TIME SPECTRAL METHOD FOR ROTORCRAFT FLOW WITH VORTICITY CONFINEMENT

A DISSERTATION
SUBMITTED TO THE DEPARTMENT OF MECHANICAL ENGINEERING
AND THE COMMITTEE ON GRADUATE STUDIES
OF STANFORD UNIVERSITY
IN PARTIAL FULFILLMENT OF THE REQUIREMENTS
FOR THE DEGREE OF
DOCTOR OF PHILOSOPHY

Nawee Butsuntorn

June 2008

© Copyright by Nawee Butsuntorn 2008
All Rights Reserved

I certify that I have read this dissertation and that, in my opinion, it is fully adequate in scope and quality as a dissertation for the degree of Doctor of Philosophy.

(G. Antony Jameson) Principal Advisor

I certify that I have read this dissertation and that, in my opinion, it is fully adequate in scope and quality as a dissertation for the degree of Doctor of Philosophy.

(Sanjiva K. Lele)

I certify that I have read this dissertation and that, in my opinion, it is fully adequate in scope and quality as a dissertation for the degree of Doctor of Philosophy.

(Robert W. MacCormack)

Approved for the University Committee on Graduate Studies.

Preface

This thesis shows that simulation of helicopter flows can adhere to engineering accuracy without the need of massive computing resources or long turnaround time by choosing an alternative framework for rotorcraft simulation. The method works in both hovering and forward flight regimes. The new method has shown to be more computationally efficient and sufficiently accurate. By utilizing the periodic nature of the rotorcraft flow field, the Fourier based Time Spectral method lends itself to the problem and significantly increases the rate of convergence compared to traditional implicit time integration schemes such as the second order backward difference formula (BDF).

A Vorticity Confinement method has been explored and has been shown to work well in subsonic and transonic simulations. Vortical structure can be maintained after long distances without resorting to the traditional mesh refinement technique.

Acknowledgments

First and foremost, I would like to say that working with Professor Jameson has been one of the best experiences that I've had during my time at Stanford. Not only is he always willing to help whenever I have questions about research, he is also a great companion and I deeply enjoy the conversations that we've had. The topics that we've talked about vary greatly including sports, life in a British/Australian boarding school (not necessarily a good life!), College life (in a British sense), etc. Of course, one of his favorite topics is mathematics (Riemann Zeta Function is one of them, Ramanujan was also a topic for a while). Professor Jameson and his wife, Charlotte, always treat me so kindly, and I've never once felt like I am just one of his many graduate students. I want to take this opportunity to say a heartfelt thank you to him.

I also would like to express my sincere gratitude to my reading committees; Professors Lele and MacCormack. Whenever I have problems with just about any subject, I always turn to Professor Lele for answers (of course it is convenient since his office is pretty much next to mine). He always has time and patience to answer my questions no matter how obscure, or how obvious and easy (for him) the questions are. Professor Lele always takes time explaining things and I've always felt that he is a fountain of knowledge, and is indeed a walking encyclopedia in the field of fluid mechanics.

One of the first CFD classes that I took at Stanford was taught by Professor MacCormack, and that class really started my interest in the field. I learned a lot from that class, and I always enjoy hearing the history of CFD as told by Professor MacCormack. It has been an incredible experience that I've had many opportunities to interact with one of the legends in CFD. On the top of that, he is also one of

the nicest professors that I've ever come across on Stanford campus. He is always kind and generous, and he is also the person who first suggested the idea of Vorticity Confinement to me.

Another person that has really made my time at Stanford such a great learning experience is Dr. Seonghyeon Hahn. We've had many meals (and coffees) together, and during these times, we discuss just about anything. Dr. Hahn has given me many valuable insights about my work during these "meetings", and many different ideas that I present in this work have come from such times.

I would also like to thank Professor Chris Allen for providing me his numerical results for comparison purposes. His help couldn't have come at a better time, and I owe a debt of gratitude to him.

Lastly, I want to thank my family and friends for their continual support. I'm sure that for my parents, my graduation couldn't have come soon enough, but I am glad that I've finally made it happen. Many, many friends have helped me along the way from the very beginning when I had great difficulties adjusting myself to a graduate student life in the U.S., then along came my Ph.D. qualifying exam, and finally my Ph.D. oral examination. I know that I couldn't have come this far without the help of all the people and friends that I've had. I really want to thank you all.

Glossary

Collective pitch	Angle of the main rotor blade pitch that changes by the same amount, thus changes the magnitude of the rotor thrust.
Cyclic pitch	Angle of attack of the blades on each revolution of the rotor, both laterally and longitudinally.
Hover	Flight regime where forward and vertical speeds are zero. Collective pitch is used to maintain altitude of the helicopter.
Zierep singularity	Phenomenon where surface pressure distribution of airfoil shows a cusp behind a normal shock. This comes from balancing the pressure behind the shock and the flow curvature demanded by the airfoil using Rankine–Hugoniot relations for gas dynamics equations.

Contents

Preface **iv**

Acknowledgments **v**

Glossary **vii**

1 Introduction **1**

1.1 Introduction to Helicopter Aerodynamics 1

1.1.1 Helicopter in Hover 2

1.1.2 Helicopter in Forward Flight 2

1.2 Motivation 3

1.2.1 Vorticity Confinement Technique 4

1.3 Thesis Outline 5

2 Background and Literature Review **6**

2.1 Helicopter Simulation 6

2.1.1 Potential Flow Simulation 8

2.1.2 Euler and RANS Simulations 9

2.1.3 Hybrid Solver 13

2.1.4 Fourier-Based Time Integration Solvers 16

2.1.5 Relevant Wind Tunnel Experiments 17

2.1.6 Summary of the Helicopter Simulation Literature Survey . . . 17

2.2 Time Dependent Simulation 18

2.2.1 Fourier Based Time Integration in Frequency Domain 20

2.2.2 Fourier-Based Time Integration in the Time Domain 21

3 Methodology **23**

3.1 Euler and Navier–Stokes Equations 23

3.1.1 RANS Equations 26

3.2 Time Spectral Method 26

3.3 Time Integration for Inner Iterations 29

3.4 Local Time Stepping 31

3.5 Residual Averaging 31

3.6 Multigrid Algorithm 32

3.6.1 Agglomeration Multigrid for the Gas Dynamics Equations . . 35

3.7 Artificial Dissipation 36

3.7.1 Jameson–Schmidt–Turkel (JST) Scheme 37

3.7.2 SLIP Scheme 38

3.7.3 CUSP Scheme 42

4 Hover Simulations **46**

4.1 Periodic Boundaries 46

4.2 Formulation for Periodically Steady State 47

4.3 Nonlifting Rotor 49

4.3.1 Boundary Conditions 50

4.3.2 Nonlifting Rotor Results 50

4.4 Lifting Rotor 50

4.4.1 Boundary Conditions 50

4.4.2 Lifting Rotor Results 52

4.5 Alternative Far-Field Boundary Condition 55

4.6 Closing Remarks 56

5 Forward Flight Simulations **61**

5.1 Complication in Forward Flight Regime 61

5.2 Mesh Topology 62

5.3 Boundary Conditions 64

5.4 Nonlifting Model Rotor in Forward Flight 66
5.4.1 Simulation Results 66
5.5 Accuracy of the Time Spectral Method 68
5.6 Time Lagged Periodic Boundary Condition 70
5.7 Lifting Rotor in Forward Flight 77
5.7.1 Simulation Results 78
5.8 Closing Remarks 79

6 Dynamic Vorticity Confinement **84**
6.1 Background of Vorticity Confinement 85
6.2 Vorticity Confinement for Incompressible Flow 86
6.3 Vorticity Confinement for Compressible Flow 87
6.3.1 Dimensional Analysis of ϵ 88
6.4 Dynamic Vorticity Confinement 90
6.5 Calculations with Vorticity Confinement 92
6.6 Vorticity Confinement in Rotorcraft Flow 95
6.7 Discussion and Analysis 96
6.7.1 Lamb–Oseen Vortex Model Problem 98
6.7.2 Numerical Diffusion vs. Vorticity Confinement 99
6.8 Closing Remarks on Vorticity Confinement 99

7 Conclusion and Future Work **105**
7.1 Recommendations for Future Work 106
7.1.1 Articulated Rotor 106
7.1.2 Aeroelasticity 106
7.1.3 Inclusion of Fuselage and Tail Rotor 107

A Numerical Method Background **108**
A.1 Non-Dimentionalization 108
A.2 Theory of Positivity 110
A.3 Local Extremum Diminishing (LED) Schemes 111

B Fourier Collocation Matrix **113**

B.1 Fourier Collocation Matrix 113

C Lifting Rotor in Forward Flight Plots **117**

List of Tables

4.1 Thrust coefficients, C_T, for different tip Mach numbers at a collective pitch of $\theta_c = 8°$ from Caradonna & Tung (1981). 52

5.1 Azimuthal angle, ψ, corresponding to blades at different frequencies. . 64

5.2 Lifting forward flight test conditions. 79

6.1 Coefficients of lift and drag from Euler calculations of NACA 0012 wing with four values of ϵ at three span stations: $M_\infty = 0.8$, $\alpha = 5°$, aspect ratio = 3. 94

List of Figures

3.1 Shock structure for single interior point 43

4.1 Single block mesh for Euler calculation with $128 \times 48 \times 32$ mesh cells 48
4.2 Coefficient of pressure distribution on a nonlifting rotor in hover using the JST scheme, $M_t = 0.52$, $\theta_c = 0°$. 51
4.3 Coefficient of pressure distribution on a lifting rotor in hover, $M_t = 0.439$, $\theta_c = 8°$. 53
4.4 Coefficient of pressure distribution on a lifting rotor in hover, $M_t = 0.877$, $\theta_c = 8°$. 54
4.5 Hover mesh with top and bottom boundaries at distance approximately five radii from the rotor. 57
4.6 Development of the flow field over time after 500 and 1,500 time steps, $M_t = 0.439$, $\theta_c = 8°$. 58
4.7 Development of the flow field over time after 2,250 and 3,000 time steps, $M_t = 0.439$, $\theta_c = 8°$. 59
4.8 Development of the flow field over time after 3,500 and 4,000 time steps, $M_t = 0.439$, $\theta_c = 8°$. 60

5.1 Schematic diagram of incident velocity normal to the leading edge of the rotor blade in forward flight. 63
5.2 Forward flight mesh for Euler calculation with $128 \times 48 \times 32$ mesh cells per blade sector. 65
5.3 Coefficient of pressure distribution on a nonlifting rotor in forward flight from Euler calculation, $M_t = 0.8$, $\theta_c = 0°$, $\mu = 0.2$, $N = 12$. . . 67

5.4 Coefficient of pressure distribution on a nonlifting rotor in forward flight including the viscous effects, $M_t = 0.8$, $\theta_c = 0°$, $\mu = 0.2$, $N = 12$. 69
5.5 Coefficient of pressure distribution on a nonlifting rotor in forward flight from Euler Calculation, $M_t = 0.8$, $\theta_c = 0°$, $\mu = 0.2$ and $N = 4$. . 70
5.6 Coefficient of pressure distribution on a nonlifting rotor in forward flight including the viscous effects, $M_t = 0.8$, $\theta_c = 0°$, $\mu = 0.2$ and $N = 4$. 71
5.7 Schematic diagram for time-lagged periodic boundary condition of a single blade sector in forward flight 72
5.8 Coefficient of pressure distribution on a nonlifting rotor in forward flight from Euler calculation using one sector of a rotor, $M_t = 0.8$, $\theta_c = 0°$, $\mu = 0.2$, $N = 12$. 73
5.9 Coefficient of pressure distribution on a nonlifting rotor in forward flight including the viscous effects using one sector of the rotor, $M_t = 0.8$, $\theta_c = 0°$, $\mu = 0.2$, $N = 12$. 74
5.10 Coefficient of pressure distribution on a nonlifting rotor in forward flight from Euler calculations using one sector of the rotor, $M_t = 0.7634$, $\theta_c = 0°$, $\mu = 0.25$, $N = 12$, aspect ratio = 7.125 with $128 \times 48 \times 32$ mesh cells. 75
5.11 Coefficient of pressure distribution on a nonlifting rotor in forward flight from Euler calculations using the entire rotor, $M_t = 0.7634$, $\theta_c = 0°$, $\mu = 0.25$, $N = 12$, aspect ratio = 7.125 with $128 \times 48 \times 32$ mesh cells. 76
5.12 Coefficient of lift per blade vs. the azimuth of a lifting rotor in forward flight using the JST dissipation scheme: $M_t = 0.7$, $\mu = 0.2857$, $\theta_c = 8°$. 80
5.13 Coefficient of lift per blade vs. the azimuth of a lifting rotor in forward flight using the CUSP dissipation scheme: $M_t = 0.7$, $\mu = 0.2857$, $\theta_c = 8°$. 81
5.14 Coefficient of pressure at $r/R = 0.90$ using the JST dissipation scheme with $192 \times 64 \times 48$ mesh cells, $M_t = 0.7$, $\mu = 0.2857$, $\theta_c = 8°$, $N = 12$. 82
5.15 Coefficient of pressure at $r/R = 0.90$ using the CUSP dissipation scheme with $192 \times 64 \times 48$ mesh cells, $M_t = 0.7$, $\mu = 0.2857$, $\theta_c = 8°$, $N = 12$. 83

6.1 Vorticity magnitude on an NACA 0012 wing with four values of ϵ: $M_\infty = 0.8$, $\alpha = 5°$, aspect ratio = 3. 93
6.2 Coefficients of lift and drag at three span stations from Euler calculation of an NACA 0012 wing with four values of ϵ, $M_\infty = 0.8$, $\alpha = 5°$, aspect ratio = 3. 94
6.3 Coefficient of pressure distribution at four span stations on NACA 0012 wing with four values of ϵ, $M_\infty = 0.8$, $\alpha = 5$, aspect ratio = 3. 95
6.4 Coefficient of lift per blade vs. the azimuth of a lifting rotor in forward flight using the JST dissipation scheme combined with Vorticity Confinement: $M_t = 0.7$, $\mu = 0.2857$, $\theta_c = 8°$, $N = 12$. 101
6.5 Vorticity magnitude of a lifting rotor in forward flight at the cut-planes $x = 2$ and $x = 5$ with $160 \times 48 \times 48$ mesh cells: $M_t = 0.7$, $\mu = 0.2857$, $\theta_c = 8°$, $N = 12$, $\psi = 90°$. 102
6.6 Mesh cross section at the tip of of the blade 102
6.7 Initial vorticity profile of a model problem with the Lamb–Oseen vortex: $r_c = 1$ and $\Gamma = 10$. 103
6.8 Vorticity distribution in the radial direction of a model problem with the Lamb–Oseen vortex: $r_c = 1$ and $\Gamma = 10$. 103
6.9 Values of the curl of the confinement term, $\vec{\nabla} \times \mathbf{s}$, for the Lamb–Oseen vortex model problem. 104

C.1 Coefficient of pressure at $r/R = 0.90$ using the JST dissipation scheme with $128 \times 48 \times 32$ mesh cells, $M_t = 0.7$, $\mu = 0.2857$, $\theta_c = 8°$, $N = 12$. 118
C.2 Coefficient of pressure at $r/R = 0.90$ using the JST dissipation scheme with $160 \times 48 \times 48$ mesh cells, $M_t = 0.7$, $\mu = 0.2857$, $\theta_c = 8°$, $N = 12$. 119
C.3 Coefficient of pressure at $r/R = 0.90$ using the CUSP dissipation scheme with $128 \times 48 \times 32$ mesh cells, $M_t = 0.7$, $\mu = 0.2857$, $\theta_c = 8°$, $N = 12$. 120
C.4 Coefficient of pressure at $r/R = 0.90$ using the CUSP dissipation scheme with $160 \times 48 \times 48$ mesh cells, $M_t = 0.7$, $\mu = 0.2857$, $\theta_c = 8°$, $N = 12$. 121

Chapter 1

Introduction

Helicopter simulation is a challenging problem due to the complexity of the flow field generated by the rotor disk, and the interaction between the vortices with the blades and fuselage. Additionally, the wide range of scales and the highly nonlinear nature of the helicopter flow make accurate prediction a very computationally expensive exercise. The thesis addresses part of the problem by introducing an alternative time integration scheme, the Time Spectral method. This recently developed approach has proved to significantly reduce the computational expense for periodic problems by solving the flow variables simultaneously at all time instances using Fourier representation. A significant further saving in computational cost is realized by the use of a Vorticity Confinement method to prevent the diffusion of the vortex wake behind each blade.

This chapter provides a brief summary of basic helicopter aerodynamics followed by the motivation behind this work, including a short introduction to Vorticity Confinement and the general outline of the thesis.

1.1 Introduction to Helicopter Aerodynamics

Uniquely, the helicopter exists to perform tasks that fixed-wing aircraft cannot perform, specifically the ability to take off and land vertically (VTOL) and to hover. There are four flight regimes in which a helicopter operates. The first is hover, where

the thrust produced by the rotor disk exactly offsets the weight of the helicopter. The helicopter remains stationary at some height off the ground. The second flight regime is vertical climb; additional thrust is produced to move the helicopter upward. Third, there is vertical descent; this flight regime is complicated because of the effects of both upward and downward flows through the rotor disk, which can significantly cause blade vibration. Lastly, there is forward flight, where the rotor disk tilts forward in the direction of the flight to create the thrust that can overcome drag.

Although vertical climb and descent represent their own unique and challenging problems, the current work focuses on two of the most important flight regimes of helicopter: hover and forward flight. There are additional issues regarding helicopter simulation that are not addressed in this work but deserve to be mentioned such as blade aeroelasticity, inclusion of the tail rotor and fuselage, and the treatment of a fully articulated rotor. These will be included in the future work and are discussed in more detail in chapter 7.

1.1.1 Helicopter in Hover

This flight regime is very unique to helicopters. There is zero forward speed as well as zero vertical speed, and collective pitch is used to maintain altitude. Therefore the flow field of helicopter in hover is axisymmetric. As a result, for an N-bladed rotor, one only needs to simulate a circular sector of the rotor with the central angle of $360^\circ/N$, instead of the entire rotor

1.1.2 Helicopter in Forward Flight

The aerodynamics of a helicopter in forward flight is much more complicated than that of a fixed-wing aircraft. One of the main causes for this difficulty is the trailing wakes from each blade. These vortices remain in the vicinity of the rotor for some revolutions, especially for a low speed forward flight. This makes it especially difficult to fully resolve using computational fluid dynamics (CFD) because of the number of grid points and computational resources required to capture and resolve

such small structures are enormous. Furthermore, it is necessary to simulate the entire rotor containing all the blades (all 360°) because each blade experiences different flow conditions at a given time, especially the relative velocity on each blade. While this is true for typical implicit time stepping schemes such the backward difference formula (BDF) by Jameson (1991), Ekici *et al.* (2008) has shown that it is possible to simulate only one sector of the rotor when combined with a Fourier based time stepping scheme through a time-lagged boundary condition. The detail of this will be discussed in section 5.6.

1.2 Motivation

In any of the four flight regimes mentioned, the flow can be characterized as periodic. This implies that flow patterns repeat after a certain interval of time (one complete revolution for helicopter rotor). Typically, periodic flows of this type are solved using fully unsteady numerical algorithms. While this approach has proved to be successful, it is very time consuming. Naturally, there are always trade-offs in unsteady flow computations between accuracy and computational cost. Highly accurate methods tend to be limited by the availability of computing power while reduced-order models fail to capture small scale physics.

During the course of the past few years, much effort has been focused at the Aerospace Computing Laboratory of Stanford University on the development of accurate and efficient methods for calculating flows which are inherently unsteady but periodic. Helicopter flows in forward flight, turbomachinery and wind turbines are constantly subjected to unsteady loads. For this class of problems, McMullen *et al.* (2001, 2002); McMullen (2003); McMullen *et al.* (2006) have shown that it is more accurate and computationally more efficient to simulate periodic flow problems using nonlinear frequency domain (NLFD) technique. The method utilizes a discrete Fourier transform for the time derivative term and can achieve better accuracy and convergence rates (9–18 times faster) than true implicit time stepping schemes such as the BDF scheme or the hybrid scheme proposed by Hsu & Jameson (2002).

Recently, Gopinath & Jameson (2005) have proposed a new method called Time

Spectral, which is simpler to implement than the typical NLFD type solver because it does not require the multiple operations of Fourier transforms and inverse Fourier transforms, while still achieving better convergence and reducing computational cost in comparison to typical implicit schemes. The foundation of this method is an application of Fourier collocation matrix to calculate the time derivative term. The memory required for this technique is comparable to the NLFD but can be 4–5 times higher than the typical second order implicit time stepping schemes (depending on the number of time instances used in a problem). The technique has been successful with problems involving pitching airfoils and wings, wind turbines (Vassberg *et al.*, 2005), and turbomachinery (Gopinath *et al.*, 2007). The motivation for this work is to extend this method further to more complicated problems, particularly the prediction of helicopter aerodynamics in forward flights.

1.2.1 Vorticity Confinement Technique

To resolve vortical structures in truly unsteady flow resolutions requires prohibitive computational resource due to the number of mesh points required. The idea of Vorticity Confinement was first proposed by Steinhoff (1994); Steinhoff & Underhill (1994) as a new method for vortex capturing by means of injecting the vortex back into the vortex core. This method has shown to be effective in treating concentrated vortical regions in coarse grids, but only for relatively simple flows. For example, flow over a cylinder (Wenren *et al.*, 2001; Dietz *et al.*, 2001), flow over an airfoil (Wang *et al.*, 1995) or flow over a wing for incompressible flows on unstructured meshes Löhner & Yang (2002); Löhner *et al.* (2002); Murayama *et al.* (2001). The method has not yet been well proven for flows over complex geometries such as rotorcraft flow or turbomachinery. The method is also somewhat controversial, and thus the literature review and discussion regarding the formulation and recent improvements as well as the validity of the results will be addressed exclusively in chapter 6.

1.3 Thesis Outline

The main purpose of this work is to demonstrate that rotorcraft simulation can achieve engineering accuracy without the need of massive computing resources or long turnaround time by use of the Time Spectral method aided by Vorticity Confinement.

Chapter 2 documents the past efforts in helicopter simulations from various approaches, ranging from potential flow calculations, Euler and Reynolds averaged Navier–Stokes (RANS) calculations, and hybrid methods. The discussion of the past work on the time integration algorithms for periodic flows using the traditional BDF formula and Fourier based methods are briefly reviewed, including ones that require the transformation to the frequency domain and others in which the flow equations remain in the physical time domain. Both these approaches are mathematically equivalent, and thus have the same level of accuracy. Chapter 3 reviews the basic governing equations, numerical algorithms, and a number of convergence acceleration techniques used in this thesis. Chapter 4 presents simulation results of hovering rotor for both nonlifting and lifting cases. Boundary conditions for lifting rotor simulation are also discussed. Chapter 5 addresses the physics of helicopters in forward flight, and subsequently presents simulation results using the Time Spectral method for both nonlifting and lifting rotors. Chapter 6 contains information regarding Vorticity Confinement including background, literature reviews, a new proposed formulation, and results from both fixed-wing and rotary-wing simulations. Lastly, chapter 7 discusses the findings from this work, conclusion, and plans for future work.

Chapter 2

Background and Literature Review

This chapter is largely divided into three parts. The first part discusses the past effort and its current status of helicopter simulation. The second part focuses on time marching methods based on discrete Fourier transform for solving periodic unsteady partial differential equations; their history and current status of such methods. Lastly, the method of Vorticity Confinement is briefly examined with respect to its potential applicability to rotorcraft flow simulations. Full detail of Vorticity Confinement can be found in chapter 6.

2.1 Helicopter Simulation

The accurate computation of helicopter rotor flows in both hover and forward flights continues to be a complex and challenging problem. Reliable prediction of helicopter performance is heavily dependent on the accurate prediction of the transonic flows on the advancing side of a helicopter rotor and proper resolution of blade–vortex and blade–wake interactions. To account for the former, a robust, fully compressible CFD solver is essential in computing the flow around rotor blades. Most compressible flow solvers, regardless of the numerical algorithms, introduce a certain amount of numerical dissipation, which can be intrinsic to the discretization or explicitly added to avoid numerical instability. In either case, the amount of dissipation is proportional to the mesh size. This is a crucial issue because it may lead to erroneous dissipation

of the wake or tip vortices and their subsequent spreading. It is clear that there is a need for a method that captures the vortical structures in order to properly resolve a helicopter wake.

Helicopter simulation remains the subject of ongoing research after many decades. An attempt to entirely simulate the main rotor system of a helicopter requires a multidisciplinary approach, involving coupling of the flow and structure models. In addition, either multi-block structured meshes or unstructured meshes are needed, and massive parallelization is a must for solving an entire helicopter including the fuselage and tail rotor. Recent comprehensive surveys of the current status of helicopter aerodynamics including both the theoretical and experimental work can be found in the article by Conlisk (1997) and the book by Leishman (2006), while an article by Friedmann (2004) extensively reviews issues regarding aeroelasticity of rotary-wing aircraft. The paper by Caradonna (2000) has an extensive review on CFD on rotorcraft with discussion of unsolved problems and prospects of solution philosophy for solving them. Books by Johnson (1994) and Stepniewski & Keys (1984) also provide excellent background on helicopter and rotary-wing aircraft aerodynamics. The remainder of this section summarizes some of the CFD work that has been done in helicopter aerodynamics and relevant experimental work.

There are many approaches that researchers use in order to simulate problems involving helicopter or rotory-wing aerodynamics. Some of the early approaches focused on the vortex dynamics using momentum theory, blade element theory and actuator vortex theory. However, as the computer power and memory increased, researchers started to work on more complicated governing equations of the fluid starting from the transonic small disturbance equation, the full potential flow equation, the Euler equations, and finally the RANS equations. To solve the true Navier–Stokes equations for helicopter simulations is still prohibitively expensive. There has been some work done using large eddy simulation (LES) to simulate parts of the geometry, mostly for the blade–vortex interaction, but it is still not computationally feasible to apply LES for the entire helicopter or even just a complete helicopter rotor.

2.1.1 Potential Flow Simulation

One of the earliest works in the field of helicopter simulation was by Caradonna & Isom (1972), who used a compressible potential flow solver to simulate nonlifting hovering helicopter blades. Analytical and numerical results of linearized subsonic three-dimensional flow in the tip region were presented. Caradonna & Isom (1976) made further progress by using the small disturbance potential flow equation with the Murman–Cole (Murman & Cole, 1970) mixed type difference technique to simulate forward flight of a nonlifting rotor blade. Later, combined experimental and simulations using the potential flow equations were carried out by Caradonna & Philippe (1978) in order to investigate transonic flow on an advancing rotor. The computational model was the two-dimensional transonic small disturbance equation for a nonlifting blade in forward flight. The test model was a modified Alouette II tail rotor with the profiles that were symmetric NACA 00XX (mostly NACA 0012) with a thickness ratio that decreased from root to tip. Three lifting cases were also considered in the paper with sinusoidal variation of the angle of attack. Chattot & Phillipe (1980) at ONERA also studied the pressure distribution on a nonlifting symmetrical helicopter blade in forward flight using the three-dimensional unsteady transonic small disturbance equation. Their numerical results were compared with experimental data, as well as computational results by RAE and NASA. The first three-dimensional, full potential flow calculation for the flow about a lifting helicopter blade was achieved by Arieli *et al.* (1985). The code was called ROT22, and was based on Jameson and Caughey's famous FLO22 (the code was an inviscid, nonconservative, three-dimensional full potential flow solver). The numerical results were compared with laser velocimeter measurements made in the tip region of a nonlifting rotor at a tip Mach number of 0.95 and zero advance ratio (i.e. no forward flight velocity component). In addition, comparisons were made with chordwise surface pressure measurements obtained in the wind tunnel for a nonlifting rotor blade at transonic tip speeds at advance ratios ranging from 0.40 to 0.50.

2.1.2 Euler and RANS Simulations

Agarwal & Deese (1987) calculated aerodynamic loads on a multi-bladed helicopter rotor in hovering flight by solving the three-dimensional Euler equations in a rotating coordinate system on body-conforming curvilinear grids around the blades. The Euler equations were recast in the absolute flow variables so that the relative flow is uniform. Equations were solved by finite volume explicit Runge–Kutta time stepping scheme based on the work of Jameson *et al.* (1981). Rotor–wake effects were modeled by computing the local induced downwash with a free wake analysis method. The far-field boundary condition was solved with one-dimensional Riemann invariant normal to the boundary. As a result, the pressure coefficient on the surface was quite accurately predicted near the tip, but was over-predicted as the distance moved closer towards the hub as compared to the experimental results by Caradonna & Tung (1981). Agarwal & Deese (1988) extended the same computation further by solving the compressible RANS equations. However, the boundary condition for the far field used in this work was still the one-dimensional Riemann invariant type, and the pressure coefficient on the surface was again under-predicted near the tip and over-predicted towards the middle of the blade.

Chen *et al.* (1990) used a finite volume upwind algorithm based on Roe flux splitting and the implicit time operator was solved by the lower upper symmetric Gauss–Seidel (LU–SGS) based on Jameson & Yoon (1987) to solve the three-dimensional Euler equations with a moving grid.

Srinivasan *et al.* (1990) performed simulations of a lifting rotor in hover based on the thin-layer Navier–Stokes equations. Their calculation used an implicit upwind finite difference method for space discretization. The monotone upstream-centered schemes for conservation laws (van Leer, 1979; Anderson *et al.*, 1984), most commonly known as the MUSCL scheme, was used to obtain the second or third order accurate fluxes with limiters in order to satisfy the total variation diminishing (TVD) property. The surface pressure calculation showed good agreement with the experimental data of Caradonna & Tung, but the wake structure diffused quickly due to the coarse grids. The authors claimed that this had minimal effects on the predicted surface pressure. Limited comparison with results calculated by the Euler equations were presented.

Srinivasan *et al.* (1991) studied the planform effects on the airloads using the three-dimensional thin-layer Navier–Stokes equations on lifting hover configurations based on UH–60 and BERP rotors. The numerical finite difference implicit numerical scheme for this work was described in the experiment of Srinivasan *et al.* (1990). The numerical algorithm used the Roe upwind-biased scheme for all three coordinates with reconstruction by higher order MUSCL schemes in order to model both shocks and propagating acoustic waves. The LU–SGS implicit operator was used to obtain the solution of both the unsteady and convective terms. The hover case was solved in the blade-fixed coordinate system.

Srinivasan & McCroskey (1993) later performed Euler calculations of unsteady interaction of advancing rotor with a line vortex. A prescribed vortex method was chosen to preserve the structure of the interacting vortex. The calculated results were compared to the two-bladed model helicopter rotor experiment by Caradonna & Tung and consisted of parallel and oblique shock interaction. Their results showed that subsonic parallel blade–vortex interaction was almost two-dimensional. However in the transonic regime, the three-dimensional effects were found to be prominent. The governing Euler equations were solved using a two-factor implicit, finite difference numerical scheme (Ying *et al.*, 1986).

A free wake Euler and Navier–Stokes calculation by Srinivasan & Baeder (1992) included the study of blade–vortex interaction (BVI) and high-speed impulsive (HSI) noise. The BVI noise is caused by the interaction of the vortical wake with the rotating blades and is more difficult to model because the three-dimensional wake effects. HSI on the other hand, is caused by the compressibility effects. The numerical schemes were identical to those used in the paper by Srinivasan *et al.* (1990).

Boniface, J. C. and Sidès, J. (1993) performed a numerical study of steady and unsteady Euler flows around multi-bladed helicopter rotors both for hover and forward flight cases. For the hover case, a source term was added and the Euler equations were solved as a steady problem. A finite volume, space-centered flux discretization that did not require artificial viscosity were used. For the time marching scheme, the authors used a modified Lax–Wendroff approximation with one predictor in each space and a corrector. However, for the forward flight simulations, an artificial viscosity

needed to be added to the equations. The hover simulations were compared with the Caradonna & Tung experiment, and also data for four-bladed rotor of IMF of Marseille. Two forward flight cases were simulated corresponding to the Caradonna *et al.* (1984) experiment and a three-bladed ONERA model rotor with cyclic pitching.

Sheffer *et al.* (1997) performed simulations of helicopter rotor flows including aeroelastic effects for both hover and forward flight using BDF for the time integration, and with the JST and CUSP artificial dissipation schemes (Jameson *et al.*, 1981; Jameson, 1995*b*). Their Euler and RANS results were in good agreements with the Caradonna & Tung model helicopter hover experiment. For the forward flight Euler calculation coupled with a structural model, 36 time steps per revolution with 50 multigrid cycles for each time step were used. After 6 revolutions, the simulation nearly reached periodic state. This simulation took 9 hours with 30 processors on IBM SP-2 machines. The total number of mesh size was 860,160 cells with 90 blocks.

Boelens *et al.* (2000) from the NLR performed computations for a helicopter rotor in hover focusing their results on vortex capturing since complete vortex wake prediction for a helicopter in hover is an important requirement for predicting the rotor performance in the hover flight regime. The compressible Euler equations expressed in an arbitrary Lagrangian Eulerian (ALE) reference frame were used in this work. The space discretization was a second order Galerkin finite element method on hexahedral mesh. The capture of vortices was achieved by local mesh refinement in regions where they were expected to form. The results were benchmarked with experimental results from Caradonna & Tung. The multi-block grid was specially generated given a grid uniform distribution to account for the tip vortex downward and inward of the blade. Even for a simple hover case with only one section of the blade, rather than the full two-bladed rotor, 55 blocks were used with the total of 726,784 elements and 823,599 mesh points. The C_p prediction of the lower surface was good but the C_p prediction of the upper surface was not that accurate as it over-predicted the pressure peak compared to the experimental data.

Pomin & Wagner (2001, 2002*b*) performed Euler/RANS hybrid computations for the hovering 7A model rotor and a low aspect ratio NACA 0012 profile in nonlifting forward flight using both periodic and overset grids. The periodic grid was a

monoblock C–H type and the computation was limited to hover cases only. The overset grid approach was used for all the helicopter flight spectrum. The C–H grids surrounding the blades were embedded into the background grid. RANS calculations were performed only in the inner regions and the Euler solver was used in the background mesh. For hover calculations, aeroelastic effects were taken into consideration via the coupling of the flow solver and a finite element model of the blade based on Timoshenko beam theory. An implicit finite volume scheme was applied for the numerical solution of the governing equation using a backward difference time discretization. The unsteady computations were second order accurate in time, and first order accurate for the hover analysis on periodic grids. The implicit system of equations was solved iteratively by a Newton method combined with LU–SGS. The hover boundary condition was based on the one-dimensional momentum theory and was applied in conjunction with a three-dimensional sink in order to determine the inflow and outflow velocities. The hover boundary condition described in these two articles is concise and better explained than others. Similar work on the hover boundary condition is also available in an article by Strawn & Ahmad (2000). Pomin & Wagner (2002*a*, 2004) included a better structural model based on Timoshenko beam with the deformable overset grids. The simulation was carried out for a fully articulated 7A model rotor for both hover and high speed forward flight. Comparative rigid blade simulations were carried out to assess the effects of blade dynamics and elasticity on the numerical results. The emphasis of these two articles was on the wake structure, aeroelasticity effects of the blades, and comparison of global thrust and torque coefficients in both hover and forward flight.

Allen (2003*a*) performed detailed simulations of steady and unsteady inviscid flow for hovering. For the unsteady simulation, the BDF time integration method used 30, 60, 120 and 360 steps per revolution (1° per step) and up to 20 revolutions. 30,000 iterations were required to obtain a converged solution for comparison with a transonic hover case from Caradonna & Tung with a tip Mach number of 0.784 and a collective pitch of 8°. Allen (2003*b*, 2004*a*, 2006) further worked on forward flight simulation on a single processor based on the the Caradonna & Tung two-bladed rotor model with a tip Mach number of 0.6 and a collective pitch of 8°. The advance ratio was

set at $\mu = 1/3$. Simulation was run with 36 steps per revolution and 20 revolutions in total for convergence. The computation for this simulation took 40,000 time steps with 1.3 million mesh points. The actual time of simulation was one week on an EV6 500 MHz processor. Allen (2007) ran simulation of an ONERA 7A four-bladed rotor with up to 192 blocks, 32 million mesh points and up to 1,024 processors.

Steijl *et al.* (2005, 2006) described and demonstrated their approach to helicopter rotor in both hover and forward flight simulation with RANS calculations. The time accurate simulation used dual time stepping with the BDF scheme. For each pseudo time solution, 25–35 steps of generalized conjugate gradient method were required to drive the residual down three orders of magnitude. The far field at the bottom of the domain for the hover case followed an empirical relation first given by Biava & Vigevano (2002), rather than the more commonly used relation of Srinivasan & McCroskey (1993). The authors suggested that periodic rotor blade motions were required to trim the rotor in forward flight. However, the blades were assumed to be rigid but the rotor was fully articulated with separate hinges for each blade. Their approach allowed for rotors with different numbers of blades and hub layouts. They used a grid deformation scheme that preserved the quality of their multi-block, structured, body-fitted mesh. Comparison of both hover and forward flight for rigid and fully articulated rotor were demonstrated using the Caradonna & Tung rotor and ONERA 7A/7AD1 rotors. For the latter, pitch changes, flapping and lead–lag deflections were included in the forward flight simulation.

2.1.3 Hybrid Solver

Recently, the idea of a hybrid solver in which wake model is integrated into a regular flow solver has proved to be popular. The model is coupled with either a full potential flow or Euler solver in the outer region far from the rotor and a RANS solver near the rotor region.

Hassan *et al.* (1992) used a finite difference scheme for the prediction of three-dimensional blade–vortex interactions via the velocity transpirational approach because of its simplicity and low implementation cost. The interaction velocity field

was obtained through a nonlinear superposition of the rotor flow field computed by the unsteady three-dimensional Euler equations. The embedded vortex wake flow field was computed using the Biot–Savart law. The three-dimensional grid was constructed by stacking two-dimensional, near orthogonal C-mesh grids generated around the blade radial. The two-dimensional grids were constructed using the method suggested by Jameson (1974). A hybrid (implicit–explicit) alternate direction implicit (ADI) scheme was used to solve the discretized equations. In the spanwise direction, the fluxes were solved explicitly while in the normal and chordwise directions, the fluxes were implicitly evaluated. Time stepping was carried out by a two-point first order backward difference scheme. The nonlifting forward flight calculation was compared to the experiment of Caradonna *et al.* (1984) with good agreement for the upstream generated vortex.

Yang *et al.* (2002) carried out helicopter rotor simulations using a hybrid solver with a potential flow solver in the outer region far from the rotor and a RANS solver near the blade region. Free and prescribed wake models were added to account for the tip vortex. The full potential solver accounts for inviscid isentropic flow in the far field. The simulation was capable of resolving the moving mesh with elastic deformations. The free and prescribed wake models were used to account for tip vortex effects once the vortex generated by the blade leaves the viscous flow region and enters the region that is in the potential flow solver. The inviscid fluxes were computed using an upwind essentially non oscillatory (ENO) scheme. The unsteady term was solved using a three-factor ADI scheme. Baldwin–Lomax (Baldwin & Lomax, 1978) turbulence model was used to calculate the eddy viscosity. Sample results were presented for the two-bladed AH–1G rotor in descent and the UH–60A rotor in high speed forward flight with reasonable accuracy.

Similarly, Zhao *et al.* (2006) coupled a full potential flow solver with a RANS solver and a free wake model for prediction of the three-dimensional viscous flow field of a helicopter rotor under both hover and forward flight. The compressible RANS solver was used for the blade and near blade area for the viscous effects. The compressible full potential flow was used to model the inviscid isentropic potential in the region far from the rotor and finally, the free wake model was used to account for

tip vortex effects in the potential flow after the vortex leaves the region of the RANS solver. The BDF scheme was used for time integration and the MUSCL scheme for spatial discretization with flux difference splitting scheme without the use of artificial viscosity. The embedded grids used in this study consisted of the cylindrical O–H background grids and the body-fitted C–H mesh around the blade. The number of grid points for the background mesh was $41 \times 71 \times 72$ with 41 points in the radial direction, 71 points in the axial direction and 72 points in the circumferential direction. $65 \times 33 \times 193$ mesh points were used for the blade with 65 points in the spanwise direction, 33 points in the normal direction and 193 points in the chordwise direction. An implicit dual-time stepping scheme with a second order BDF was adopted, using an explicit Runge–Kutta five stage scheme for integrating the pseudo time solution for each step. Five cases were simulated; two hover cases and three forward flight cases. The numerical results using the hybrid solver were in good agreement with the experimental data for the hover case, and quite good for the forward cases considering that the data came from flight tests and the grids used in this work only covered the entire rotor without the fuselage or tail rotor. It was also shown that the computational effort using the hybrid solver was reduced by approximately 43 % compared to a typical RANS solver (38 hours vs. 62 hours).

Bhagwat *et al.* (2005) recently developed a new potential flow based model for hover performance prediction with focus on the capture of the wake system (location and circulation distribution). Hover performance prediction tools traditionally consists of prescribed wake and free wake methods coupled to full potential flow, Euler or RANS solver. These methods, including Lagrangian free wake methods are susceptible to instabilities. Additionally, most methods require wake trajectories, which are not actually *free* and have to be derived from experimental data sets. The authors derived a new method called vorticity embedding, which claimed to permit free wake vortex convection. This is the second generation of such a method. The first generation vorticity embedding method can be found in the paper of Ramachandran *et al.* (1994). A hybrid RANS solver coupled with a free wake model was also tested. The numerical results were compared with UH–60A performance; wake and loads data. An approximate factorization scheme based on Jameson (1979) was used to solve the

full potential flow equation. Bhagwat *et al.* (2006) later placed more emphasis on the RANS solver by placing a small C-mesh around the blade region coupled with the vorticity embedding wake model. The solver used in the work was the TURNS code developed by Srinivasan *et al.* (1990).

Approaching the problem via commercial software, Xu *et al.* (2005) simulated a rigid two-bladed rotor of Caradonna *et al.* and a Robin four-bladed rotor in forward flight with cyclic pitching using a Chimera moving grid approach. They used the commercial code CFD–FASTRAN, in which the compressible Euler equations are spartially discretized using a finite volume method. The flux vectors were evaluated using Roe linearization with different limiters. The time marching algorithm was the Jacobi iterative implicit scheme (this is a first order accurate scheme). For the four-bladed Robin rotor, $30 \times 143 \times 63$ grid points were used for blade with 30 points in the normal direction, 143 points in the chordwise direction and 63 points in the spanwise direction. Additionally, the parent grid size was $64 \times 60 \times 87$ for one half of the cylindrical domain. Thus for the entire computational domain, there were just over 1.75 million mesh points. Each time step corresponded to 1.184×10^{-5} seconds, this represents the incremental rotational angle of only 0.15°. Results for forward flight showed quite good agreement in comparison with experimental data.

2.1.4 Fourier-Based Time Integration Solvers

Recently, there have been two other groups who have been working on Fourier-based time integration solves for rotorcraft simulation purposes. The first group of people are from Syracuse University (Kumar & Murthy, 2007, 2008), and the second is from Duke University (Ekici *et al.*, 2008). The first group's method is based on forward and backward Fourier transforms similar to the NLFD technique. However, their results show large discrepancy with experimental data. The group from Duke University has shown good results compared to the experimental data, although their code still required thousands of time steps to converge to a reasonable solution. Additionally, Ekici *et al.* also proposed a new periodic boundary condition so that it is possible to perform forward flight calculation using only one blade (as opposed to simulating

the entire rotor as has been traditionally done). The application of this boundary condition and its results compared to the traditional method are discussed in section 5.6.

2.1.5 Relevant Wind Tunnel Experiments

One of the most cited experimental works in helicopter simulation is the experiment of a model helicopter rotor in hover by Caradonna & Tung (1981) due to its simplicity. It is still widely used today as a benchmark test case for simulation of helicopter rotor in hover. Their experiment included a wide range of tip Mach numbers from subsonic to transonic flow regimes. They used a large chamber with special ducting designed to eliminate the circulation caused by the rotor. The rotor was a two-bladed model with NACA 0012 profile and were untwisted and untapered. The aspect ratio of the blades was six, with a radius of 1.143 meter.

NASA Rotorcraft Division has also conducted other experiments on model helicopter rotors in forward flight such as those described in the NASA Technical Reports of Caradonna *et al.* (1984, 1988) and Owen & Tauber (1986). The results in chapter 5 compare the computational results with the data from Caradonna *et al.* (1984). The model used in this experiment was a two-bladed teetering-rotor system equipped with full collective and cyclic control. The blades were 7 feet in diameter and 6 inches in chord with an untapered and untwisted NACA 0012 profile; this gives an aspect ratio of 7. These blades were constructed almost entirely of balsa and carbon/epoxy composites, so they were quite stiff.

2.1.6 Summary of the Helicopter Simulation Literature Survey

The aforementioned literature survey is by no means a complete representation of the body of helicopter simulation work since the work in this field has been around for more than three decades. The previous section is intended to give readers a general impression of the variety of approaches that have been employed in order to calculate the aerodynamics or helicopter rotors, both in hover and especially forward

flight. However, one thing in common found in almost all of the literature is that only two groups have tried to use Fourier-based time integration to simulate the periodic unsteadiness of helicopter. As a result, most of the simulations mentioned in the previous section required huge computational resources and were very time consuming. The work in this thesis will focus on the Fourier-based algorithm, and will demonstrate that helicopter simulation based on the Time Spectral method can vastly decrease the simulation time and computational expense compared to other methods used in the past.

2.2 Unsteady and Time Dependent Flow Simulation for Periodic Problems

From section 2.1, it can be seen that in compressible Euler and RANS calculations, by far, the most popular method for solving unsteady problems is by the dual time stepping BDF by Jameson (1991), which is an implicit time marching scheme. The other popular implicit method is the Crank–Nicolson scheme (Crank & Nicolson, 1947). The most well known advantage of the Crank–Nicolson method is that it does not have any amplitude error. The scheme is also A-stable, which means that it is unconditionally stable for any given time step on the left half of the complex plane. As an aside, it is more appropriate to view this scheme as a trapezoidal integration in time. While it is true that the Crank–Nicolson scheme in unconditionally stable, if the time step Δt is too large, the solution can oscillate between 1 and –1 because the scheme is undamped. See Moin (2001) for an example.

On the other hand, the BDF scheme is a tried and tested scheme that works very well with compressible Euler and RANS calculations. The discretization that is most commonly used is

$$\frac{3}{2\Delta t}\left\{\mathbf{w}^{n+1}\mathcal{V}^{n+1}\right\} - \frac{4}{2\Delta t}\left\{\mathbf{w}^{n}\mathcal{V}^{n}\right\} + \frac{1}{2\Delta t}\left\{\mathbf{w}^{n-1}\mathcal{V}^{n-1}\right\} + \mathbf{R}\left(\mathbf{w}^{n+1}\right) = 0. \qquad (2.1)$$

This is the second order accurate backward difference formula (BDF2), which is also

A-stable, and is a preferred practical choice for compressible Euler and RANS simulations in the CFD community. Consistent with the Dahlquist barrier theorem (Dahlquist, 1956, 1959), higher order accurate BDF are not A-stable.

For the case where the cell volumes remain the same at all time steps, the BDF2 simplifies to

$$\mathcal{V}\left\{\frac{3}{2\Delta t}\mathbf{w}^{n+1}-\frac{4}{2\Delta t}\mathbf{w}^{n}+\frac{1}{2\Delta t}\mathbf{w}^{n-1}\right\}+\mathbf{R}\left(\mathbf{w}^{n+1}\right)=0. \tag{2.2}$$

However, while the BDF method is very robust and is a second order accurate scheme, for problems involving periodic flows, the method still requires at least 5–6 cycles (complete revolutions) to reach converged periodic solutions, with as many as 360 steps in each period. Although this is acceptable for two-dimensional cases, three-dimensional external flow RANS simulations still take weeks or months to complete. Explicit time stepping schemes are rarely used for time dependent calculation because they generally take even longer to obtain converged periodic solutions. An interesting algorithm was studied by van der Ven *et al.* (2001), who introduced the multitime multigrid algorithm with the main application expected to be future forward flight simulations of helicopter rotors. The authors claimed that one order of magnitude reduction in time compared to the classic multigrid acceleration time could be achieved at the expense of one order of magnitude increase in memory usage. In essence, the authors proposed to solve the problem for all time steps simultaneously, recognizing that periodic problems can be considered as steady state problems in the space–time domain. A pseudo time method can be introduced in order to march the solution to a steady state using standard acceleration techniques such as local time stepping, grid sequencing and multigrid. One difference compared to previous techniques is that the multi-level techniques will be applied to the space–time grid, and not restricted to the space grid only. So time is treated as just another dimension. This method is also scalable beyond 1,000 processors machines as has been demonstrated by the ASCI project (Mavriplis, 1999).

2.2.1 Fourier Based Time Integration in Frequency Domain

The focus of this thesis is the simulation of helicopter rotors, which constitutes a periodic problem with strong nonlinearity. The Harmonic Balance method by Hall *et al.* (2002) was the first method that resolves the full nonlinear equations in the frequency domain for compressible flow. McMullen *et al.* (2001, 2002, 2006) subsequently studied the nonlinear frequency domain (NLFD) method in detail, and showed that it is 8–19 times faster than the BDF scheme for Euler simulations of a two-dimensional pitching airfoil. Additionally, it was shown that the accuracy of the time derivative converges to a smooth function faster than any power of the mesh width. In other words, the method displays spectral accuracy while being computationally cheaper than traditional BDF implicit time stepping schemes.

Starting with the governing equations in semi-discrete form:

$$\frac{\mathrm{d}}{\mathrm{d}t}\left(\mathcal{V}\,\mathbf{w}\right) + \mathbf{R}(\mathbf{w}) = 0,$$

and with the assumption that both $\mathbf{w}$ and $\mathbf{R}(\mathbf{w})$ are both periodic in time. These variables are then independently transformed using finite Fourier series, therefore

$$\mathbf{w} = \sum_{k=-\frac{N}{2}}^{\frac{N}{2}-1} \widehat{\mathbf{w}}_k \mathrm{e}^{\mathrm{i}kt} \qquad \text{and} \qquad \mathbf{R}(\mathbf{w}) = \sum_{k=-\frac{N}{2}}^{\frac{N}{2}-1} \widehat{\mathbf{R}_k(\mathbf{w})} \mathrm{e}^{\mathrm{i}kt}$$

where $\mathrm{i} = \sqrt{-1}$. Using the orthogonality property of the Fourier terms and the assumption that the volume $\mathcal{V}$ does not vary in time, a separate equation is obtained for each Fourier wave number k,

$$\mathrm{i}k\mathcal{V}\,\widehat{\mathbf{w}}_k + \widehat{\mathbf{R}_k(\mathbf{w})} = 0. \tag{2.3}$$

However, the coefficients of $\widehat{\mathbf{R}_k(\mathbf{w})}$ are not independent from the coefficients of $\widehat{\mathbf{w}}_k$ because $\mathbf{R}(\mathbf{w})$ is a nonlinear function of $\mathbf{w}$. Hence, (2.3) cannot be solved directly. So, first, $\mathbf{R}(\mathbf{w})$ is calculated from $\mathbf{w}$. Then $\mathbf{R}(\mathbf{w})$ is Fourier transformed to $\widehat{\mathbf{R}_k(\mathbf{w})}$. With this approach, one needs the values of $\mathbf{R}(\mathbf{w})$ at all the instances in time in order

to proceed to the Fourier transformation. This increases the storage significantly since the residual at each wave number, k, needs to be stored. Additionally, for each iteration, at least two Fourier transformations for $\mathbf{w}$ and the residual $\mathbf{R}(\mathbf{w})$ are required to get to (2.3). To summarize this approach, one needs to perform the following steps:

(1) Assume that $\widehat{\mathbf{w}}_k$ is known at all time instances (this is the initial condition).

(2) Inverse Fourier transform $\widehat{\mathbf{w}}_k$ back to the physical space to obtain $\mathbf{w}$.

(3) Calculate the residual $\mathbf{R}(\mathbf{w})$.

(4) Fourier transform $\mathbf{R}(\mathbf{w})$ back to the frequency space to obtain $\widehat{\mathbf{R}_k(\mathbf{w})}$.

Define the unsteady residual as

$$\widehat{\mathbf{R}_k(\mathbf{w})} + \mathrm{i}k\widehat{\mathbf{w}}_k = \widehat{\mathbf{I}_k(\mathbf{w})},$$

and instead of solving (2.3) directly by an iterative method, one can introduce a pseudo time τ and thus a pseudo time derivative term can be added. The resulting set of equations becomes

$$\mathcal{V}\frac{\mathrm{d}\widehat{\mathbf{w}}_k}{\mathrm{d}\tau} + \widehat{\mathbf{I}_k(\mathbf{w})} = 0. \tag{2.4}$$

Now one can easily solve this equation by numerically integrating (2.4) in the pseudo time.

2.2.2 Fourier-Based Time Integration in the Time Domain

Gopinath & Jameson (2005); Gopinath (2007) extend the idea of Fourier-based time integration further by using a Fourier collocation matrix for the temporal derivative term. While the basic fundamental is the same as the NLFD method, this method avoids the transformation of dependent variables back and forth from time and frequency domain. This is a large computational saving and the implementation is more straightforward compared to the NLFD algorithm as it is simpler to implement this

technique in existing flow solvers. As a result, The governing equations are now essentially solved in the physical domain, rather than the frequency domain.

The core of this idea is the use of a Fourier collocation matrix, which is a matrix that couples all the dependent variables at all time instances with equally spaced intervals. These dependent variables are simultaneously iterated until the periodic steady state is reached. Unlike a time marching method (either explicit or implicit), periodicity is an assumption from the beginning. So there is no need to wait for the periodic pattern of the solution to be established. Similar to the NLFD method discussed previously, the introduction of a pseudo time derivative is utilized, so that the existing flow solver can be used to drive the equations to the steady state in pseudo time. This method (along with the NLFD method) can take advantage of other well proven convergence acceleration techniques such as multigrid and local time stepping. It can also be implemented with Message Passing Interface (MPI) with some modification to the existing flow solvers. The detailed algorithm of this technique will be presented in section 3.2.

Chapter 3

Mathematical Formulation and Methodology

This chapter addresses the governing equations and the common numerical formulations used in the work of this thesis. Details of certain numerical algorithms for particular cases are discussed in later chapters.

3.1 Euler and Navier–Stokes Equations

Let p, ρ, E and H denote the pressure, density, total energy and total enthalpy of the fluid. The Cartesian coordinates and velocity components are denoted by x_1, x_2, x_3 and u_1, u_2, u_3 respectively. Einstein notation is used to simplify the presentation of the equations where summation is implied by a repeated index.

For an arbitrary volume of fluid Ω, consider the flow equations without a body force in integral form:

$$\frac{\partial}{\partial t}\int_{\Omega} \mathbf{w}\,\mathrm{d}\mathcal{V} + \oint_{\partial\Omega} \mathbf{f}_j \cdot \mathbf{n}\,\mathrm{d}\mathcal{S} = 0 \tag{3.1}$$

where $\int_{\Omega} \mathrm{d}\mathcal{V}$ is the volumetric integral, $\oint_{\partial\Omega} \mathrm{d}\mathcal{S}$ is the surface integral, $\mathbf{n}$ is the outward pointing normal unit vector normal to the surface and $\mathbf{w}$ is the state vector with the

following components:

$$\mathbf{w} = \begin{bmatrix} \rho \\ \rho u_1 \\ \rho u_2 \\ \rho u_3 \\ \rho E \end{bmatrix}.$$

The flux $\mathbf{f}_j$ contains both the convective and viscous terms and can be split into two two components:

$$\mathbf{f}_j = \mathbf{f}_{j,c} - \mathbf{f}_{j,v} \tag{3.2}$$

where $\mathbf{f}_{j,c}$ is the convective flux and $\mathbf{f}_{j,v}$ is the viscous flux. Consider the control volume boundary that moves with the velocity $\mathbf{b} = b_j = \partial x_j/\partial t$, the flux terms can now be written as

$$\mathbf{f}_{j,c} = \begin{bmatrix} \rho\,(u_j - b_j) \\ \rho u_1\,(u_j - b_j) + p\,\delta_{1j} \\ \rho u_2\,(u_j - b_j) + p\,\delta_{2j} \\ \rho u_3\,(u_j - b_j) + p\,\delta_{3j} \\ \rho E\,(u_j - b_j) + p\,u_j \end{bmatrix} \quad \text{and} \quad \mathbf{f}_{j,v} = \begin{bmatrix} 0 \\ \tau_{1j} \\ \tau_{2j} \\ \tau_{3j} \\ u_m \tau_{mj} - q_j \end{bmatrix} \tag{3.3}$$

where δ_{mj} is the Kronecker delta, q_j is the heat flux in the j direction and τ_{mj} is the stress tensor. Its components are given by

$$\tau_{mj} = \mu \left(\frac{\partial u_j}{\partial x_m} + \frac{\partial u_m}{\partial x_j} \right) + \delta_{mj} \lambda \frac{\partial u_l}{\partial x_l}$$

where μ is the dynamic viscosity of the fluid and λ is the second coefficient of viscosity, which is equal to $-2\mu/3$. The dynamic viscosity can be modeled using Sutherland's law where μ is a function of temperature:

$$\mu = \frac{(1.458 \times 10^{-6})\, T^{\frac{3}{2}}}{T + 110.4},$$

and the temperature is defined by

$$T = \frac{p}{(\gamma - 1)\rho}.$$

With the aid of Fourier's law of heat conduction, the heat flux q_j is defined as

$$q_j = -\kappa \frac{\partial T}{\partial x_j},$$

where κ is the thermal conductivity of the fluid, which is defined as

$$\kappa = \frac{\gamma \mu}{\mathrm{Pr}}.$$

The values of the ratio of specific heats, γ, and Prandtl number are held constant at 1.4 and 0.725 respectively. The equation of state provides the closure for the governing equations. For an ideal gas,

$$E = \frac{p}{(\gamma - 1)\rho} + \frac{1}{2}\left(u_j u_j\right) \qquad \text{and} \qquad H = E + \frac{p}{\rho}.$$

For Euler calculations, the term $\mathbf{f}_{j,v}$ in (3.2) is set to zero.

Following the analysis presented in Appendix A.1, the governing equations can be stated in dimensionless form as:

$$\frac{\partial}{\partial t^*} \oint_\Omega \mathbf{w}^* \, \mathrm{d}\mathcal{V}^* + \oint_{\partial\Omega} \mathbf{f}^*_{j,c} \cdot \mathbf{n}^* \, \mathrm{d}\mathcal{S}^* + \sqrt{\gamma} \frac{\mathrm{M}_0}{\mathrm{Re}_0} \oint_{\partial\Omega} \mathbf{f}^*_{j,v} \cdot \mathbf{n}^* \, \mathrm{d}\mathcal{S}^* = 0 \tag{3.4}$$

where M_0 and Re_0 are the reference Mach number and Reynolds number. For brevity, the superscript * will be dropped from the variables for the remainder of the thesis.

Using central differencing in combination with the artificial dissipation scheme outlined in section 3.7 for spatial discretization, the governing equations (3.1) can be written in semi-discrete form:

$$\mathcal{V} \frac{\mathrm{d}\mathbf{w}}{\mathrm{d}t} + \mathbf{R}(\mathbf{w}) = 0. \tag{3.5}$$

3.1.1 RANS Equations

For high Reynolds number case in which the flow becomes turbulent, the RANS equations for compressible flow are derived using Favre averaging. This results in nine additional unknowns termed the Reynolds stresses, $\partial\left(\overline{u_j u_m}\right)/\partial x_m$. However, these Reynolds stresses are symmetric, therefore there are only six unknowns. There are various types/levels of closures. There are zero-equation, one-equation and two-equation models, which are scalar models. Additionally there are Reynolds stress transport models, which are tensor models. In simple closures, the total dynamic viscosity of the fluid can be found by addition of the dynamic viscosity and the turbulent dynamic viscosity:

$$\mu_{\text{total}} = \mu + \mu_t.$$

The total thermal conductivity now becomes:

$$\begin{aligned} \kappa_{\text{total}} &= \kappa + \kappa_t \\ &= \gamma\left(\frac{\mu}{\text{Pr}} + \frac{\mu_t}{\text{Pr}_t}\right). \end{aligned}$$

where κ_t is the thermal conductivity due to the effect of turbulence, μ_t is the turbulent dynamic viscosity of the fluid and Pr_t is the turbulent Prandtl number, which is held constant at 0.9 in throughout this work.

The value of turbulent dynamic viscosity μ_t (or more commonly referred to as eddy viscosity, $\nu_t = \mu_t/\rho$) can be calculated by many different turbulence models. A recent review on different types of closure models can be found in (Ji, 2006, Chapter 1). In this work, the Baldwin–Lomax zero-equation turbulence model is used for the closure (Baldwin & Lomax, 1978).

3.2 Time Spectral Method

Taking advantage of the periodic nature of periodic unsteady problems, a Fourier representation in time can achieve high level of accuracy using a small number of modes. However, typical nonlinear frequency domain solvers require multiple forward

and backward Fourier transforms between the time and frequency domain for every time step. The Time Spectral method addresses this complexity by utilizing the Fourier collocation matrix (Canuto *et al.*, 2007). As a result, the governing equations are now solved in the time domain only. The total number of equations that needs to be solved concurrently correspond directly to the number of time instances required for the period.

Recall that for a periodic function, $f(x)$, defined on N equally spaced grid points, $x_j = j\Delta$ where $j = 0, 1, 2, \ldots, N-1$, the discrete Fourier transform of f is

$$\hat{f}_k = \frac{1}{N} \sum_{j=0}^{N-1} f_j \mathrm{e}^{-\mathrm{i}kx_j}, \tag{3.6}$$

and its inverse transform is

$$f_j = \sum_{k=-N/2}^{N/2-1} \hat{f}_k \mathrm{e}^{\mathrm{i}kx_j}. \tag{3.7}$$

Then, the Fourier transform of the derivative approximation is computed by multiplying the Fourier transform of f by $\mathrm{i}k$

$$\widehat{Df_k} = \mathrm{i}k\hat{f}_k$$

where D is the spectral derivative operator. Therefore the spectral derivative of f at point j is

$$\left.\frac{\partial f}{\partial x}\right|_j = \sum_{k=-N/2+1}^{N/2-1} \widehat{Df_k} \mathrm{e}^{\mathrm{i}kx_j}.$$

Note that in the above representation, the period in space, x, is assumed to be 2π and the wave number $k = -n/2$ is omitted. This is done because if f is a real function, the derivative of f cannot be complex.

If one wishes to have a compact representation of the spectral derivative operator in the physical space and not in the wave space, a physical (time) space operator for numerical differentiation can be derived for the governing equations as follows.

Using the definition from (3.6) and (3.7), the discrete Fourier transform of the

state vector $\mathbf{w}$ for a time period T is

$$\widehat{\mathbf{w}}_k = \frac{1}{N}\sum_{n=0}^{N-1} \mathbf{w}^n \mathrm{e}^{-\mathrm{i}k\frac{2\pi}{T}n\Delta t},$$

and its inverse transform:

$$\mathbf{w}^n = \sum_{k=-\frac{N}{2}}^{\frac{N}{2}-1} \widehat{\mathbf{w}}_k \mathrm{e}^{\mathrm{i}k\frac{2\pi}{T}n\Delta t}. \tag{3.8}$$

The spectral derivative of (3.8) with respect to time at the n-th time instance is given by

$$D\mathbf{w}^n = \frac{2\pi}{T}\sum_{k=-\frac{N}{2}}^{\frac{N}{2}-1} \mathrm{i}k\,\widehat{\mathbf{w}}_k \mathrm{e}^{\mathrm{i}k\frac{2\pi}{T}n\Delta t}.$$

This summation involves the Fourier modes $\widehat{\mathbf{w}}_k$ that can be written in the conservative variables $\mathbf{w}$ in the time domain as

$$D\mathbf{w}^n = \sum_{j=0}^{N-1} d_n^j \mathbf{w}^j$$

where

$$d_n^j = \begin{cases} \frac{2\pi}{T}\frac{1}{2}(-1)^{n-j}\cot\left\{\frac{\pi(n-j)}{N}\right\} & : \quad n \neq j \\ 0 & : \quad n = j \end{cases}.$$

This representation of the time derivative expresses the multiplication of a matrix with elements d_n^j and the vector $\mathbf{w}^j$. The detailed derivation of the Fourier collocation matrix for the spectral derivative can be found in Appendix B.1.

Let $n - j = -m$, one can rewrite the time derivative term as

$$D\mathbf{w}^n = \sum_{m=-\frac{N}{2}+1}^{\frac{N}{2}-1} d_m \mathbf{w}^{(n+m)}, \tag{3.9}$$

where d_m is given by

$$d_m = \begin{cases} \frac{2\pi}{T}\frac{1}{2}(-j)^{m+1}\cot\left\{\frac{\pi m}{N}\right\} & : \quad m \neq 0 \\ 0 & : \quad m = 0 \end{cases}.$$

Using (3.9) in (3.5), the governing equations in semi-discrete form is

$$\mathcal{V}D\mathbf{w}^n + \mathbf{R}(\mathbf{w}^n) = 0. \tag{3.10}$$

Introducing pseudo time, τ, to (3.10) in the same manner as the implicit dual time stepping scheme,

$$\mathcal{V}\frac{\mathrm{d}\mathbf{w}^n}{\mathrm{d}\tau} + \mathcal{V}D\mathbf{w}^n + \mathbf{R}(\mathbf{w}^n) = 0. \tag{3.11}$$

Equation (3.11) can now be solved as a steady state problem in pseudo time for the four dimensional space–time solution using well known convergence acceleration techniques.

3.3 Time Integration for Inner Iterations

In combination with the Fourier collocation matrix, the objective is to march the equations at each time level to pseudo steady state as quickly as possible. Runge–Kutta time stepping scheme with modified coefficients that maximizes the stability region can be readily applied. Hence one can split the residual $\mathbf{R}(\mathbf{w})$ in (3.11) into two parts

$$\mathbf{R}(\mathbf{w}) = \mathbf{Q}(\mathbf{w}) - \mathbf{D}(\mathbf{w}) \tag{3.12}$$

where $\mathbf{Q}(\mathbf{w})$ is the convective part and $\mathbf{D}(\mathbf{w})$ is the dissipative part. Denote the time level $n\Delta t$ by a superscript n, then the multi-stage time stepping scheme is formulated

as follows

$$\begin{aligned}
\mathbf{w}^{(n+1,0)} &= \mathbf{w}^{n} \\
&\cdots \\
\mathbf{w}^{(n+1,k)} &= \alpha_k \Delta t \left\{ \mathbf{Q}\left(\mathbf{w}^{(k-1)}\right) + \mathbf{D}\left(\mathbf{w}^{(k-1)}\right) \right\} , \\
&\cdots \\
\mathbf{w}^{n+1} &= \mathbf{w}^{(n+1,m)}
\end{aligned}$$

where k denotes the k-th stage and $\alpha_m = 1$. Note that this superscript n is not the n-th time instance as used in section 3.2, but the actual time level as is conventionally known. Additionally,

$$\begin{aligned}
\mathbf{Q}^{(0)} &= \mathbf{Q}\left(\mathbf{w}^{n}\right) \\
&\cdots \\
\mathbf{Q}^{(k)} &= \mathbf{Q}\left(\mathbf{w}^{(n+1,k)}\right)
\end{aligned}$$

and

$$\begin{aligned}
\mathbf{D}^{(0)} &= \mathbf{D}\left(\mathbf{w}^{n}\right) \\
&\cdots \\
\mathbf{D}^{(k)} &= \beta_k \mathbf{D}\left(\mathbf{w}^{(n+1,k)}\right) + \left(1-\beta_k\right)\mathbf{D}^{(k-1)}
\end{aligned}$$

Jameson's modified Runge–Kutta five-stage time stepping scheme is used to advance the solution forward at all time instances. Different coefficients are used for the convective and dissipative terms at each stage of the multi-stage scheme in order to maximize the stability region. The coefficients α_k are chosen to maximize the stability interval along the imaginary axis, and the efficients β_k are chosen to increase the stability interval along the negative real axis. These schemes do not fall within the classic Runge–Kutta schemes and they have much larger stability regions (Jameson, 1985*b*). The coefficients of the five-stage scheme with three evaluations of dissipation

are as follows:

$$\begin{array}{lllllll} \alpha_1 & = & \frac{1}{4} & & \beta_1 & = & 1. \\ \alpha_2 & = & \frac{1}{6} & & \beta_2 & = & 0. \\ \alpha_3 & = & \frac{3}{8} & & \beta_3 & = & 0.56 \\ \alpha_4 & = & \frac{1}{2} & & \beta_4 & = & 0. \\ \alpha_5 & = & 1 & & \beta_5 & = & 0.44 \end{array} . \tag{3.13}$$

3.4 Local Time Stepping

Unlike an explicit time accurate scheme where the global time step is determined by the minimum time step of all the cells in the domain, the local time stepping scheme uses the local optimal time step for each individual cell based on the local CFL number (Jameson, 1982). Therefore, if the objective is to reach steady state as quickly as possible, using local time stepping scheme will march the solution in each cell independently towards the global steady state without loss of accuracy in the solution. Since there are n sets of equations in (3.11) that can be thought of as n steady flow problems, local time stepping is utilized at every stage of the multi-stage time integration.

3.5 Residual Averaging

The properties of multi-stage schemes can be further enhanced by residual averaging. The residual at each mesh point, $\mathbf{R}(\mathbf{w})$ is replaced by an implicitly weighted average of neighboring residuals (Jameson & Baker, 1983). In one dimension, $\mathbf{R}_j(\mathbf{w})$ is replaced by $\overline{\mathbf{R}}_j(\mathbf{w})$, where at the j-th mesh point

$$-\epsilon\overline{\mathbf{R}}_{j-1} + (1+2\epsilon)\overline{\mathbf{R}}_j - \epsilon\overline{\mathbf{R}}_{j+1} = \mathbf{R}_j.$$

It can easily be shown that the scheme can be stabilized for arbitrarily large time step by choosing a sufficiently large value for ϵ. In a non-dissipative one-dimensional

case, the value of ϵ is

$$\epsilon > \frac{1}{4}\left\{\left(\frac{\Delta t}{\Delta t^*}\right)^2 - 1\right\}$$

where Δt^* is the maximum stable time step of the basic scheme, and Δt is the actual time step. The method can be extended to three dimensions by using smoothing in product form

$$\left(1-\epsilon_x\delta_x^2\right)\left(1-\epsilon_y\delta_y^2\right)\left(1-\epsilon_z\delta_z^2\right)\overline{\mathbf{R}} = \mathbf{R} \tag{3.14}$$

3.6 Multigrid Algorithm

The concept of convergence acceleration by multiple grids was first proposed by Federenko (1964) for Laplace's equation and it was later popularized by Brandt (1977). Jameson (1983, 1986) showed that multigrid method can be applied to a set of hyperbolic equations with great success in practice. To date, there has been no mathematical proof that this idea must work for hyperbolic partial differential equations. In fact, it is possible to show counter examples in the case that the inflow boundary data is not sufficiently smooth (Jameson, 2003). On the other hand, there exists a comprehensive theory of multigrid convergence acceleration for elliptic partial differential equations, for example, in the paper by Nicolaides (1978).

Just to illustrate the idea, for a simple time stepping scheme, an update at a point affects its neighbors in the next time step. If one takes a simple two-dimensional Laplace's equation on a uniform mesh:

$$u_{i,j}^{n+1} = u_{i,j}^n + \frac{\sigma\Delta t}{\Delta x^2}\left(u_{i+1,j}^n - 2u_{i,j}^n + u_{i-1,j}^n\right) + \frac{\sigma\Delta t}{\Delta y^2}\left(u_{i,j+1}^n - 2u_{i,j}^n + u_{i,j-1}^n\right),$$

it is clear that the information at the left boundary can only reach the right boundary in a number of steps equal to the number of mesh intervals. For example, on 100×100 mesh, the information on the left hand side can only cross the mesh in 100 steps. Hence to reach the equilibrium solution, this would require thousands of iterations. Additionally, since the optimal time step increases with the increase in mesh size, one can anticipate that the rate of convergence would also increase on a coarser mesh.

To illustrate the basic of multigrid, consider a linear problem

$$Lu = f. \tag{3.15}$$

Discretize (3.15) on a grid with interval h as

$$L_h u_h = f_h. \tag{3.16}$$

Suppose one can obtain an estimate v_h of the solution, which would need a correction δv_h. Equation (3.16) can be re-written as

$$L_h \left(v_h + \delta v_h\right) = f_h,$$

or in terms of a residual R_h

$$L_h \delta v_h + R_h = 0$$

where

$$R_h = L_h v_h - f_h. \tag{3.17}$$

Substitute (3.17) to a coarser grid with interval $2h$ as

$$L_{2h} \delta v_{2h} + I_{2h}^h R_h = 0 \tag{3.18}$$

and interpolate the correction back to the fine mesh as

$$v_h^{n+1} = v_h^n + I_h^{2h} \delta v_{2h}. \tag{3.19}$$

The transfer operators from fine to coarse and coarse to fine meshes are I_{2h}^h and I_h^{2h} respectively.

The idea can be extended to a sequence of grids by obtaining a correction to the estimate δv_{2h} by transferring (3.18) to a grid with interval $4h$ and so on. One may

use grids with

$$\left.\begin{array}{c} 128 \times 128 \\ 64 \times 64 \\ 32 \times 32 \\ 16 \times 16 \\ 8 \times 8 \\ 4 \times 4 \\ 2 \times 2 \end{array}\right\} \equiv \text{number of mesh cells in the } k\text{-th level.}$$

With Dirichlet boundary condition, the 2×2 grid has only 1 unknown. If the fine grid residual, R_h, is zero, the residuals on coarse meshes are not necessarily zero. Without care, these coarse meshes residuals will drive the fine mesh solution, which is incorrect. Typical cycle for multigrid is a V-cycle, which is the simplest. Updates are performed on the way down. But one might use iterations at each level on the way down and not on the way up.

It follows that the cells on a fine mesh can typically be amalgamated into larger cells. On a coarse mesh, conservation laws are applied as in the fine mesh but with the addition of the residual of the fine mesh acts as a forcing term. The correction from the coarse mesh is then interpolated back to the fine mesh. If one uses an explicit scheme and the time step is doubled each time the process passes to a coarser mesh, a five-level multigrid V-cycle consisting of one time step on each mesh represents a total advance in time of

$$\Delta t + 2\Delta + 4\Delta t + 8\Delta t + 16\Delta t = 31\Delta t$$

where Δt is the time step on the finest mesh. On a two-dimensional grid, the work for one multigrid cycle is

$$1 + \frac{1}{4} + \frac{1}{16} + \frac{1}{64} + \frac{1}{256} \leq \frac{4}{3}.$$

Similarly, on a three-dimensional grid, the work is

$$1 + \frac{1}{8} + \frac{1}{64} + \frac{1}{512} + \frac{1}{4096} \leq \frac{8}{7}.$$

3.6.1 Agglomeration Multigrid for the Gas Dynamics Equations

It is possible to devise a multigrid scheme using a sequence of coarser meshes by eliminating every other point in each direction, so that each coarse grid cell is an agglomeration of the fine grid cells it contains. First, perform a time advancement in a fine grid by standard multi-stage scheme as in section 3.3.

$$\begin{aligned} \mathbf{w}_h^{(1)} &= \mathbf{w}_h^{(0)} - \alpha_1 \Delta t_h \mathbf{R}_h^{(0)} \\ &\cdots \\ \mathbf{w}_h^{(q+1)} &= \mathbf{w}_h^{(0)} - \alpha_{q+1} \Delta t_h \mathbf{R}_h^{(q)} \end{aligned} \quad . \tag{3.20}$$

Then, initialize the solution vector $\mathbf{w}$ on grid $2h$ as

$$\mathbf{w}_{2h}^{(0)} = T_{2h,h} \mathbf{w}_h$$

where $\mathbf{w}_h$ is the current value on grid h and $T_{2h,h}$ is the transfer operator. The transferred solution to the next coarser grid is performed by area (two-dimensional) or volume (three-dimensional) weighting (conservative transfer).

$$\mathbf{w}_{2h}^{(0)} = \frac{\sum_{ijk} \mathcal{V}_h \mathbf{w}_h}{\sum_{ijk} \mathcal{V}_h} = Q_{2h}^h \mathbf{w}_h.$$

The residual summation is then transferred

$$\mathbf{R}_{2h}^{(0)} = \sum_{ijk} \mathbf{R}_h = I_{2h}^h \mathbf{R}_h.$$

It is important to transfer the residual forcing function such that the solution on grid $2h$ is driven by the residual calculated on grid h. Setting

$$\mathbf{P}_{2h} = Q_{2h,h}\mathbf{R}_h\left(\mathbf{w}_h\right) - \mathbf{R}_{2h}\left[\mathbf{w}_{2h}^{(0)}\right]$$

where $Q_{k,k-1}$ is another transfer operator. For the update of the solution, replace $\mathbf{R}_{2h}\left(\mathbf{w}_{2h}\right)$ by $\mathbf{R}_{2h}(\mathbf{w}_{2h}) + \mathbf{P}_{2h}$ in the time stepping scheme. Thus the multi-stage scheme for the coarser meshes is reformulated as

$$\begin{aligned} \mathbf{w}_{2h}^{(1)} &= \mathbf{w}_{2h}^{(0)} - \alpha_1 \Delta t_{2h}\left[\mathbf{R}_{2h}^{(0)} + \mathbf{P}_{2h}\right] \\ &\ldots \\ \mathbf{w}_{2h}^{(q+1)} &= \mathbf{w}_{2h}^{(0)} - \alpha_{q+1} \Delta t_{2h}\left[\mathbf{R}_{2h}^{(q)} + \mathbf{P}_{2h}\right] \end{aligned} \quad . \tag{3.21}$$

The result $\mathbf{w}_{2h}^{(m)}$ then provides the initial data for grid $4h$ and so on. Finally, the accumulated correction has to transferred to the finer meshes via an interpolation operator, e.g.

$$\mathbf{w}_h^+ = \mathbf{w}_h + I_h^{2h}\left(\mathbf{w}_{2h} - \mathbf{w}_{2h}^{(0)}\right)$$

using bilinear or trilinear interpolation.

3.7 Artificial Dissipation

To suppress odd–even coupling and to prevent oscillations near discontinuities, it is necessary to add artificial dissipative terms. While the first order upwind scheme is the least diffusive first order scheme that satisfies the local extremum diminishing (LED) criterion, it is desirable to have higher order LED scheme. For detailed description of an LED scheme, refer to Appendix A.3.

The use of flux splitting allows precise matching of the dissipative terms to control the minimum amount of dissipation needed to prevent oscillations. As a result, the numerical shock thickness is reduced to the minimum attainable, typically one or two cells for a normal shock. In practice, using adaptive coefficients have proven that shock waves can be captured cleanly without flux splitting. The formulation of three

methods based on such concepts that are used in this work is presented as follows.

3.7.1 Jameson–Schmidt–Turkel (JST) Scheme

This follows the seminal paper by Jameson *et al.* (1981) where an effective form of $\mathbf{D}(\mathbf{w})$ is suggested consisting a blend of second and fourth order differences with the coefficients depending on local pressure gradients. The construction of the dissipative terms is similar for all the five dependent equations. For the purpose of illustration, the continuity equation will be used to demonstrate the construction of the dissipative term. Define the numerical diffusive terms to be

$$\mathbf{D}\rho = \mathbf{D}_x\rho + \mathbf{D}_y\rho + \mathbf{D}_x\rho.$$

where $\mathbf{D}_x$, $\mathbf{D}_y$ and $\mathbf{D}_z$ are the corresponding diffusive contributions of the three Cartesian coordinate directions. Writing these terms in conservation form

$$\begin{aligned}
\mathbf{D}_x\rho &= \mathbf{d}_{i+\frac{1}{2},j,k} - \mathbf{d}_{i-\frac{1}{2},j,k} \\
\mathbf{D}_y\rho &= \mathbf{d}_{i,j+\frac{1}{2},k} - \mathbf{d}_{i,j-\frac{1}{2},k} \\
\mathbf{D}_z\rho &= \mathbf{d}_{i,j,k+\frac{1}{2}} - \mathbf{d}_{i,j,k-\frac{1}{2}},
\end{aligned}$$

any of the terms on the right hand side follows the following form:

$$\begin{aligned}
\mathbf{d}_{i+\frac{1}{2},j,k} = \Big\{ & \epsilon^{(2)}_{i+\frac{1}{2},j,k} \left(\rho_{i+1,j,k} - \rho_{i,j,k}\right) \\
& - \epsilon^{(4)}_{i+\frac{1}{2},j,k} \left(\rho_{i+2,j,k} - 3\rho_{i+1,j,k} + 3\rho_{i,j,k} - \rho_{i-1,j,k}\right) \Big\}. \quad (3.22)
\end{aligned}$$

The idea is to use variable coefficients $\epsilon^{(2)}_{i+\frac{1}{2},j}$ and $\epsilon^{(4)}_{i+\frac{1}{2},j}$ that produce a low level of diffusion in the regions where the flow is smooth, but add enough dissipation to prevent oscillations near discontinuities.

Now define

$$\nu_{i,j,k} = \frac{|p_{i+1,j,k} - 2p_{i,j,k} + p_{i-1,j,k}|}{|p_{i+1,j,k}| + 2\,|p_{i,j,k}| + |p_{i-1,j,k}|}.$$

Also define

$$\epsilon^{(2)}_{i+\frac{1}{2},j,k} = \kappa^{(2)} \max\left(\nu_{i+1,j,k}, \nu_{i,j,k}\right)$$

and

$$\epsilon^{(4)}_{i+\frac{1}{2},j,k} = \max\left\{0, \left(\kappa^{(4)} - \epsilon^{(2)}_{i+\frac{1}{2},j,k}\right)\right\}.$$

Typically values of $\kappa^{(2)}$ and $\kappa^{(4)}$ are

$$\kappa^{(2)} = \frac{1}{4} \qquad \text{and} \qquad \kappa^{(4)} = \frac{1}{256}.$$

The dissipative terms for the remaining equations are obtained in a similar fashion by substituting ρu, ρv, ρw and ρH in (3.22).

3.7.2 SLIP Scheme

Jameson (1995a) introduced the symmetric limited positive (SLIP) scheme as a high resolution scheme without oscillation. This is achieved by introducing flux limiters to ensure the positivity condition. The original idea of this improved scheme dates back to the paper by Jameson (1985a).

Consider a one-dimensional scalar conservation law

$$\frac{\partial v}{\partial t} + \frac{\partial}{\partial x} f(v) = 0 \tag{3.23}$$

where it can be represented by a three point scheme as

$$\frac{\mathrm{d}v_j}{\mathrm{d}t} = c^+_{j+\frac{1}{2}}\left(v_{j+1} - v_j\right) + c^-_{j-\frac{1}{2}}\left(v_j - v_{j-1}\right).$$

The scheme is LED if

$$c^+_{j+\frac{1}{2}} > 0 \qquad \text{and} \qquad c^-_{j-\frac{1}{2}} < 0.$$

Written in semi-discrete form, the evolution of the value v_j in the j-th cell is governed by the equation

$$\Delta x \frac{\mathrm{d}v_j}{\mathrm{d}t} + h_{j+\frac{1}{2}} - h_{j-\frac{1}{2}} = 0$$

where $h_{j+\frac{1}{2}}$ is an estimate of the flux between cells j and $j+1$. Using an arithmetic

average for the flux evaluation does not satisfy the positivity condition and an artificial dissipative term needs to be added. Thus one can set

$$h_{j+\frac{1}{2}} = \frac{1}{2}\left(f_{j+1} + f_j\right) - \alpha_{j+\frac{1}{2}}\left(v_{j+1} - v_j\right)$$

where $\alpha_{j+\frac{1}{2}}$ is a coefficient that needs to be determined. Also define the numerical wave speed $a_{j+\frac{1}{2}}$, which is analogous to $\partial f/\partial u$ as

$$a_{j+\frac{1}{2}} = \begin{cases} \frac{f_{j+1}-f_j}{v_{j+1}-v_j} & \text{if} \quad v_{j+1} \neq v_j \\ \frac{\partial f}{\partial v}|_{v=v_j} & \text{if} \quad v_{j+1} = v_j \end{cases} .$$

So now

$$\begin{aligned} h_{j+\frac{1}{2}} &= f_j + \frac{1}{2}\left(f_{j+1} - f_j\right) - \alpha_{j+\frac{1}{2}}\left(v_{j+1} - v_j\right) \\ &= f_j - \left(\alpha_{j+\frac{1}{2}} - \frac{1}{2}a_{j+\frac{1}{2}}\right)\left(v_{j+1} - v_j\right) \end{aligned}$$

and

$$h_{j-\frac{1}{2}} = f_j - \left(\alpha_{j-\frac{1}{2}} + \frac{1}{2}a_{j-\frac{1}{2}}\right)\left(v_j - v_{j-1}\right).$$

Then

$$h_{j+\frac{1}{2}} - h_{j-\frac{1}{2}} = \left(\frac{1}{2}a_{j+\frac{1}{2}} - \alpha_{j+\frac{1}{2}}\right)\Delta v_{j+\frac{1}{2}} + \left(\frac{1}{2}a_{j-\frac{1}{2}} + \alpha_{j-\frac{1}{2}}\right)\Delta v_{j-\frac{1}{2}}$$

where

$$\Delta v_{j+\frac{1}{2}} = v_{j+1} - v_j \qquad \text{and} \qquad \Delta v_{j-\frac{1}{2}} = v_j - v_{j-1}.$$

The LED condition is satisfied if

$$\alpha_{j+\frac{1}{2}} \geq \frac{1}{2}\left|a_{j+\frac{1}{2}}\right|.$$

The construction of the flux limiters can now be done as follows. First introduce

$L(u, v)$ as a limited average of u and v with the following properties:

$$\begin{aligned} L(u,v) &= L(v,u) && (3.24a)\\ L(\alpha u, \alpha v) &= \alpha L(v,u) && (3.24b)\\ L(u,u) &= u && (3.24c)\\ L(u,v) &= 0 \qquad \text{if } u \text{ and } v \text{ have opposite sign.} && (3.24d) \end{aligned}$$

Property (3.24d) is required for the construction of an LED scheme.

Also introduce a notation

$$\phi(r) = L(1, r) = L(r, 1). \tag{3.25}$$

Upon setting $\alpha = 1/u$ or $1/v$ and using the notation from (3.25) and property (3.24b), it follows that

$$L(u, v) = \phi\left(\frac{v}{u}\right) u = \phi\left(\frac{u}{v}\right) v.$$

If one sets $v = 1$ and $u = r$, then

$$\phi(r) = r\phi\left(\frac{1}{r}\right).$$

The diffusive flux for a one-dimensional scalar conservation law is now defined to be

$$d_{j+\frac{1}{2}} = \alpha_{j+\frac{1}{2}} \left\{ \Delta v_{j+\frac{1}{2}} - L\left(\Delta v_{j+\frac{3}{2}}, \Delta v_{j-\frac{1}{2}}\right) \right\}.$$

Additionally, define

$$r^+ = \frac{\Delta v_{j+\frac{3}{2}}}{\Delta v_{j-\frac{1}{2}}} \qquad \text{and} \qquad r^- = \frac{\Delta v_{j-\frac{3}{2}}}{\Delta v_{j+\frac{1}{2}}}.$$

Then the semi-discrete one-dimensional scalar conservation law becomes

$$\begin{aligned}\Delta x\frac{\mathrm{d}v_j}{\mathrm{d}t} =& -\frac{1}{2}a_{j+\frac{1}{2}}\Delta v_{j+\frac{1}{2}} - \frac{1}{2}a_{j-\frac{1}{2}}\Delta v_{j-\frac{1}{2}} \\ &+ \alpha_{j+\frac{1}{2}}\left(\Delta v_{j+\frac{1}{2}} - \phi\left(r^+\right)\Delta v_{j-\frac{1}{2}}\right) \\ &- \alpha_{j-\frac{1}{2}}\left(\Delta v_{j-\frac{1}{2}} - \phi\left(r^-\right)\Delta v_{j+\frac{1}{2}}\right) \\ =& \left\{\alpha_{j+\frac{1}{2}} - \frac{1}{2}a_{j+\frac{1}{2}} + \alpha_{j-\frac{1}{2}}\phi\left(r^-\right)\right\}\Delta v_{j+\frac{1}{2}} \\ &- \left\{\alpha_{j-\frac{1}{2}} + \frac{1}{2}a_{j-\frac{1}{2}} + \alpha_{j+\frac{1}{2}}\phi\left(r^+\right)\right\}\Delta v_{j-\frac{1}{2}}.\end{aligned}$$

The scheme satisfies the LED condition if $\alpha_{j+\frac{1}{2}} \geq \frac{1}{2}\left|a_{j+\frac{1}{2}}\right|$ for all j and $\phi(r) \geq 0$. The first order diffusive flux is canceled when Δv is smooth and of a constant sign. Another variation is to include the coefficient $\alpha_{j+\frac{1}{2}}$ in the limited average by setting

$$d_{j+\frac{1}{2}} = \alpha_{j+\frac{1}{2}}\Delta v_{j+\frac{1}{2}} - L\left(\alpha_{j+\frac{3}{2}}\Delta v_{j+\frac{3}{2}}, \alpha_{j-\frac{1}{2}}\Delta v_{j-\frac{1}{2}}\right)$$

A number of limiters can be defined that meet the requirements of properties (3.24a) to (3.24d). First define

$$S(u,v) = \frac{1}{2}\left\{\mathrm{sign}(u) + \mathrm{sign}(v)\right\}$$

so that

$$S(u,v) = \begin{cases} 1 & \text{if } u > 0 \text{ and } v > 0 \\ 0 & \text{if } u \text{ and } v \text{ have opposite sign} \\ -1 & \text{if } u < 0 \text{ and } v < 0 \end{cases}.$$

The following limiters are the well known limiters that have the required properties.

(1) Minmod:

$$L(u,v) = S(u,v)\min(|u|,|v|)$$

(2) van Leer:

$$L(u,v) = S(u,v)\frac{2|u||v|}{|u|+|v|}$$

(3) Superbee:

$$L(u,v) = S(u,v)\max\{\min(2|u|,|v|),\min(|u|,2|v|)\}.$$

3.7.3 CUSP Scheme

Jameson (1995*b*) introduced the convective upwind and split pressure (CUSP) scheme based on characteristic decomposition. This scheme leads to conditions on the diffusive flux such that the stationary discrete shock can contain only one single interior point. This type of scheme satisfies the following criteria:

(1) It produces an upwind flux if the flow is supersonic through the interface.

(2) It satisfies a generalized eigenvalue problem for the exit from the shock of the form

$$(A_{AR} + \alpha_{AR}\, B_{AR})\,(\mathbf{w}_R - \mathbf{w}_A) = 0,$$

where A_{AR} is the linearized Jacobian matrix and B_{AR} is the matrix defining the diffusion for the interface AR. Scalar diffusion such as the JST or SLIP schemes do not satisfy the first condition.

Let $\mathbf{w}_L$ and $\mathbf{w}_R$ be the left and right states that satisfy the shock jump conditions for a stationary shock with the corresponding fluxes, $\mathbf{f}_L = \mathbf{f}(\mathbf{w}_L)$ and $\mathbf{f}_R = \mathbf{f}(\mathbf{w}_R)$. If the shock is stationary, $\mathbf{f}_L = \mathbf{f}_R$ and the discrete shock also has constant states $\mathbf{w}_L$ to the left and $\mathbf{w}_R$ to the right. Additionally, $\mathbf{w}_A$ is an intermediate value in the middle. Figure 3.1 shows the schematic diagram of the model of a discrete shock structure.

For one-dimensional case gas dynamics equations, define the diffusive flux as

$$\mathbf{d}_{j+\frac{1}{2}} = \frac{1}{2}\alpha^* c\,(\mathbf{w}_{j+1} - \mathbf{w}_j) + \frac{1}{2}\beta\,(\mathbf{f}_{j+1} - \mathbf{f}_j)$$

where c is the speed of sound and is included to make α^* dimensionless. Let M be the Mach number u/c. If the flow is supersonic, an upwind scheme is achieved by setting

$$\alpha^* = 0, \qquad \beta = \text{sign}\,(\text{M})\,.$$

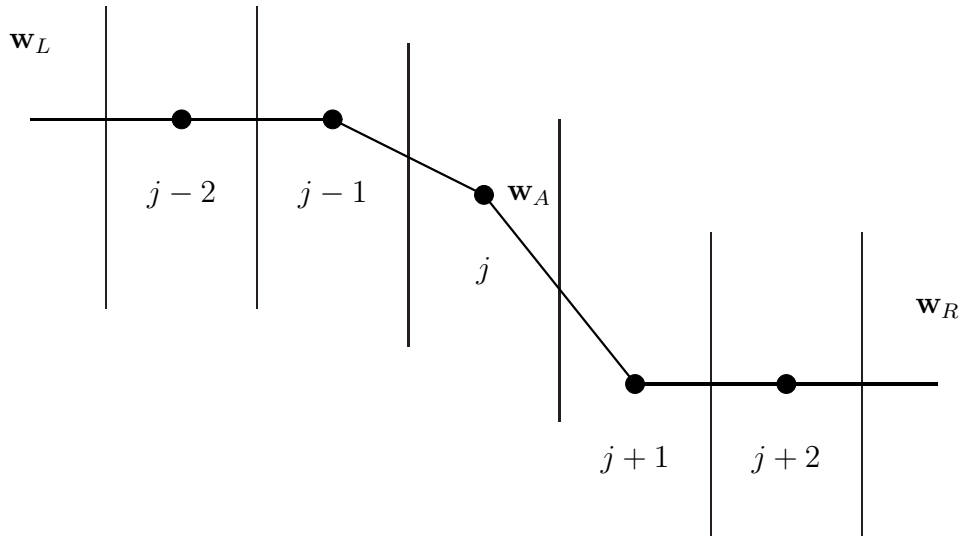

Figure 3.1: Shock structure for single interior point

If one chooses the Roe linearization, the Mach number is calculated from u and c. At the entrance to the shock transition to an intermediate value $\mathbf{w}_A$ is admitted with $u > c$. Therefore,

$$\mathbf{h}_{LA} = \frac{1}{2}(\mathbf{f}_A + \mathbf{f}_L) - \frac{1}{2}(\mathbf{f}_A - \mathbf{f}_L) = \mathbf{f}_L.$$

The fluxes leaving and entering the cell immediately to the right of the shock are now

$$\mathbf{h}_{RR} = \mathbf{f}_R$$

since $\Delta\mathbf{w}$ and $\Delta\mathbf{f}$ are zero, while

$$\mathbf{h}_{AR} = \frac{1}{2}(\mathbf{f}_R + \mathbf{f}_A) - \frac{1}{2}\alpha^* c\,(\mathbf{w}_R - \mathbf{w}_A) - \frac{1}{2}\beta\,(\mathbf{f}_R - \mathbf{f}_A)$$

since $\mathbf{h}_{j+\frac{1}{2}} = \mathbf{h}_{j+\frac{3}{2}} = \mathbf{f}_R$.

Hence

$$(1-\beta)(\mathbf{f}_R - \mathbf{f}_A) + \alpha^* c\,(\mathbf{w}_R - \mathbf{w}_A) = 0.$$

They are in equilibrium if

$$\mathbf{f}_R - \mathbf{f}_A + \frac{\alpha^* c}{1+\beta}\left(\mathbf{w}_R - \mathbf{w}_A\right) = 0.$$

Since

$$\mathbf{f}_R - \mathbf{f}_A = A_{RA}\left(\mathbf{w}_R - \mathbf{w}_A\right),$$

we have an eigenvalue problem

$$A_{RA}\left(\mathbf{w}_R - \mathbf{w}_A\right) = -\frac{\alpha^* c}{1+\beta}\left(\mathbf{w}_R - \mathbf{w}_A\right).$$

Assuming that $u > 0$, the only negative eigenvalue is $u - c$. Therefore α^* and β must satisfy

$$\frac{\alpha^* c}{1+\beta} = c - u.$$

This gives a one parameter family of schemes where if you have α^*, β is determined, or vice versa.

The choice $\beta = \mathrm{M}$ when $\mathrm{M} < 1$ leads to $\alpha^* =$ constant. This is very diffusive and corresponds to the Harten–Lax–van Leer (HLL) scheme.

To get a less diffusive scheme, note that

$$\mathbf{f} = u\mathbf{w} + \begin{pmatrix} 0 \\ p \\ up \end{pmatrix} \qquad \text{and} \qquad \Delta\mathbf{f} = \overline{u}\Delta\mathbf{w} + \overline{\mathbf{w}}\Delta u + \Delta\begin{pmatrix} 0 \\ p \\ up \end{pmatrix}$$

The recommended choice for the effective coefficient of diffusion is

$$\alpha c = \alpha^* c + \beta\overline{u}.$$

To get low diffusion, set $\alpha = |\mathrm{M}|$. Then

$$\begin{aligned} \alpha c &= \alpha^* c - \beta \\ &= (1+\beta)(c-u) \\ &= c - u + \beta c - \beta u, \end{aligned}$$

and therefore

$$\alpha = 1 - \mathrm{M} + \beta,$$

where $\alpha = \mathrm{M}$. Therefore

$$\beta = \begin{cases} \max(0, 2\mathrm{M}-1) & \text{if} \quad 0 \leq \mathrm{M} \leq 1 \\ \min(0, 2\mathrm{M}+1) & \text{if} \quad -1 \leq \mathrm{M} \leq 0 \end{cases}.$$

Chapter 4

Hover Simulations

Hovering is one of the most important features of a helicopter; it is where all the velocities in the lateral and vertical direction and zero and only the rotor generates just enough thrust to offset the weight of the helicopter. It is this unique feature that makes helicopters different from other aircraft with the consequence that hovering is one of the two most important flight regimes for helicopters. Thus it is important to be able to predict these flows accurately in order to improve the performance of the rotor design.

4.1 Periodic Boundaries

The coordinate system employed in this thesis is as follows: y is the vertical direction with $y = 0$ at the rotor plane, z is the spanwise direction starting from the rotor hub to tip and beyond, and x in the chordwise direction that completes an orthogonal system. Hence the rotation vector is always

$$\mathbf{\Omega} = \begin{bmatrix} 0 \\ \Omega_2 \\ 0 \end{bmatrix}.$$

Therefore, for brevity, the subscript 2 will be dropped from Ω for the remainder of this thesis.

For an N-bladed calculation of a hovering rotor, only one blade or $1/N$ of the cylindrical domain needs to be considered. The upstream and downstream boundary planes can be treated as periodic boundaries. Figure 4.1 show the isometric and top views of a representative mesh topology used in the computations. The root of the blade is located at $K = 9$ and the tip is located at $K = 25$ with 33 grid points in this direction. The distance from the tip to the far-field boundary in the z direction is approximately 1.5 times the rotor radius. The top and bottom boundaries are located at approximately 1.5 radii from the rotor plane.

At the periodic planes, the state variables required for the halo cells in the downstream boundary are evaluated using the following matrix transformation:

$$\begin{bmatrix} \rho \\ \rho u_1 \\ \rho u_2 \\ \rho u_3 \\ \rho E \end{bmatrix}_{\text{downstream, } JE} = \begin{bmatrix} 1 & 0 & 0 & 0 & 0 \\ 1 & \cos\left(\frac{2\pi}{N}\right) & 0 & \sin\left(\frac{2\pi}{N}\right) & 0 \\ 0 & 0 & 1 & 0 & 0 \\ 1 & -\sin\left(\frac{2\pi}{N}\right) & 0 & \cos\left(\frac{2\pi}{N}\right) & 0 \\ 0 & 0 & 0 & 1 & 0 \end{bmatrix} \cdot \begin{bmatrix} \rho \\ \rho u_1 \\ \rho u_2 \\ \rho u_3 \\ \rho E \end{bmatrix}_{\text{upstream, } JL}$$

where JE denotes the first halo cells and JL denotes the inner cells at the outermost boundary in the $\mathbf{j}$ direction. Similarly, the transformation matrix for the upstream boundary is

$$\begin{bmatrix} \rho \\ \rho u_1 \\ \rho u_2 \\ \rho u_3 \\ \rho E \end{bmatrix}_{\text{upstream, } JE} = \begin{bmatrix} 1 & 0 & 0 & 0 & 0 \\ 1 & \cos\left(\frac{2\pi}{N}\right) & 0 & -\sin\left(\frac{2\pi}{N}\right) & 0 \\ 0 & 0 & 1 & 0 & 0 \\ 1 & \sin\left(\frac{2\pi}{N}\right) & 0 & \cos\left(\frac{2\pi}{N}\right) & 0 \\ 0 & 0 & 0 & 1 & 0 \end{bmatrix} \cdot \begin{bmatrix} \rho \\ \rho u_1 \\ \rho u_2 \\ \rho u_3 \\ \rho E \end{bmatrix}_{\text{downstream, } JL}$$

4.2 Formulation for Periodically Steady State

For the hover case, it is possible to solve for the absolute velocities without physically rotating the computational grid, Holmes & Tong (1984) suggested adding a source term to the governing equations (3.1), so that the problem can now be solved as a

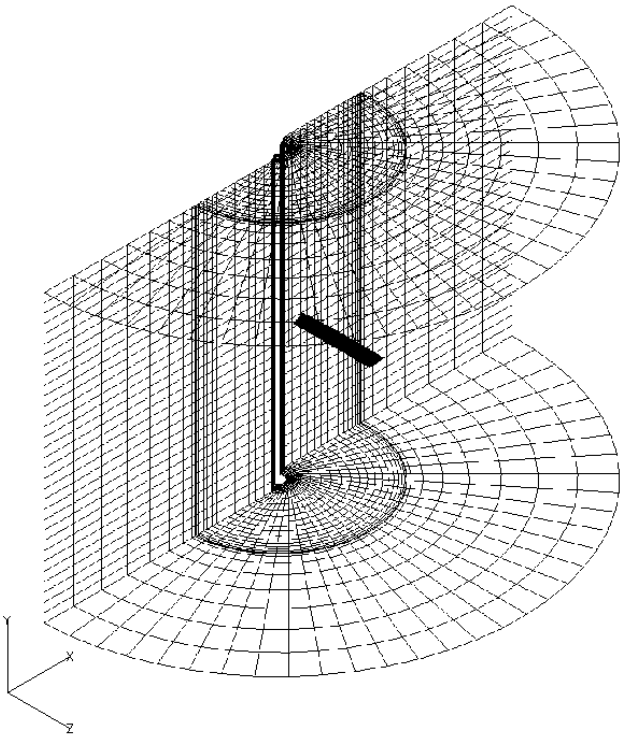

(a) Isometric view

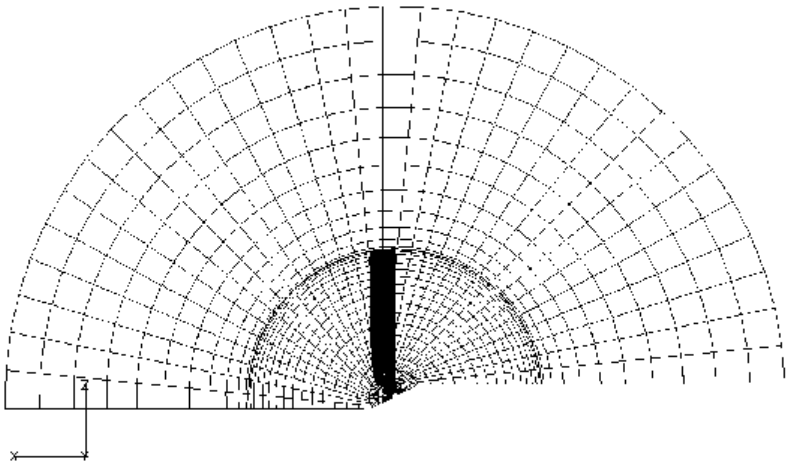

(b) Top view

Figure 4.1: $128 \times 48 \times 32$ computational mesh cells for Euler calculations modeling an untwisted, untapered, two-bladed NACA 0012 rotor with an aspect ratio of 6 for hover case

steady case. This leads to the new set of governing equations:

$$\int_{\Omega} \frac{\partial \mathbf{w}}{\partial t} \, \mathrm{d}\mathcal{V} + \oint_{\partial\Omega} \mathbf{f} \cdot \mathbf{n} \, \mathrm{d}\mathcal{S} = \int_{\Omega} \mathbf{T} \, \mathrm{d}\mathcal{V}$$

where $\mathbf{T}$ is defined as

$$\mathbf{T} = \begin{bmatrix} 0 \\ \rho\Omega u_3 \\ 0 \\ -\rho\Omega u_1 \\ 0 \end{bmatrix}$$

for a rotor that lies in the (x, z) plane with the angular velocity Ω. The results of Euler calculations shown in this chapter are solved with this forcing term unless otherwise stated.

4.3 Nonlifting Rotor

To verify the general algorithm of the flow solver, a nonlifting case was tested corresponding to the experimental work of Caradonna & Tung (1981). This is a good case for testing the flow solver in the absence of downwash effects and also the blade–vortex interaction. The experimental setup consisted of a two-bladed model helicopter rotor in hover. The blades were untapered and untwisted with the aspect ratio of six and NACA 0012 profile.

For this nonlifting case, the tip Mach number is 0.52, the collective pitch is set to zero degree with the angular velocity, Ω, equal to 1500 revolutions per minute (RPM). The tip Mach number is defined as

$$\mathrm{M}_t = \frac{\Omega R}{a_0}$$

where R is the radius of the the blade and a_0 is the reference speed of sound.

4.3.1 Boundary Conditions

A Riemann Invariant boundary condition for one-dimensional flow normal to the boundary is used for the three far-field boundaries; top, bottom and the far field in the spanwise direction. A solid body boundary condition is used at the rotor hub and on the blade (flow tangency for Euler calculation). The periodic boundary conditions described in section 4.1 are used at the remaining two boundaries.

4.3.2 Nonlifting Rotor Results

An Euler calculation was performed on $128 \times 48 \times 32$ cells with 128 cells in the chordwise direction, 48 cells in the direction normal to the blade and 32 cells in the spanwise direction. The coefficient of pressure distribution at four different span stations are shown in figure 4.2. In this case, the agreement with the experimental data is excellent.

4.4 Lifting Rotor

Typically, when one uses Riemann Invariant boundary conditions for the far fields, the velocities tend to vanish outside the computational domain. While this assumption is acceptable for a nonlifting rotor, it does not make physical sense for lifting rotors. The above assumption implies that the flow circulates inside the computational domain while in reality, the rotor disk continuously draws the fluid from outside the computational box. To remedy this inconsistency, Srinivasan *et al.* (1991) modeled this process as a sink in the downwash boundary. Using one-dimensional momentum theory, the mass flow requirements can be satisfied, leading to better agreement with experimental results.

4.4.1 Boundary Conditions

In this method, the wake velocity obtained from momentum theory induces a mass flux that has to be balanced by an opposite mass flux through the inflow boundaries.

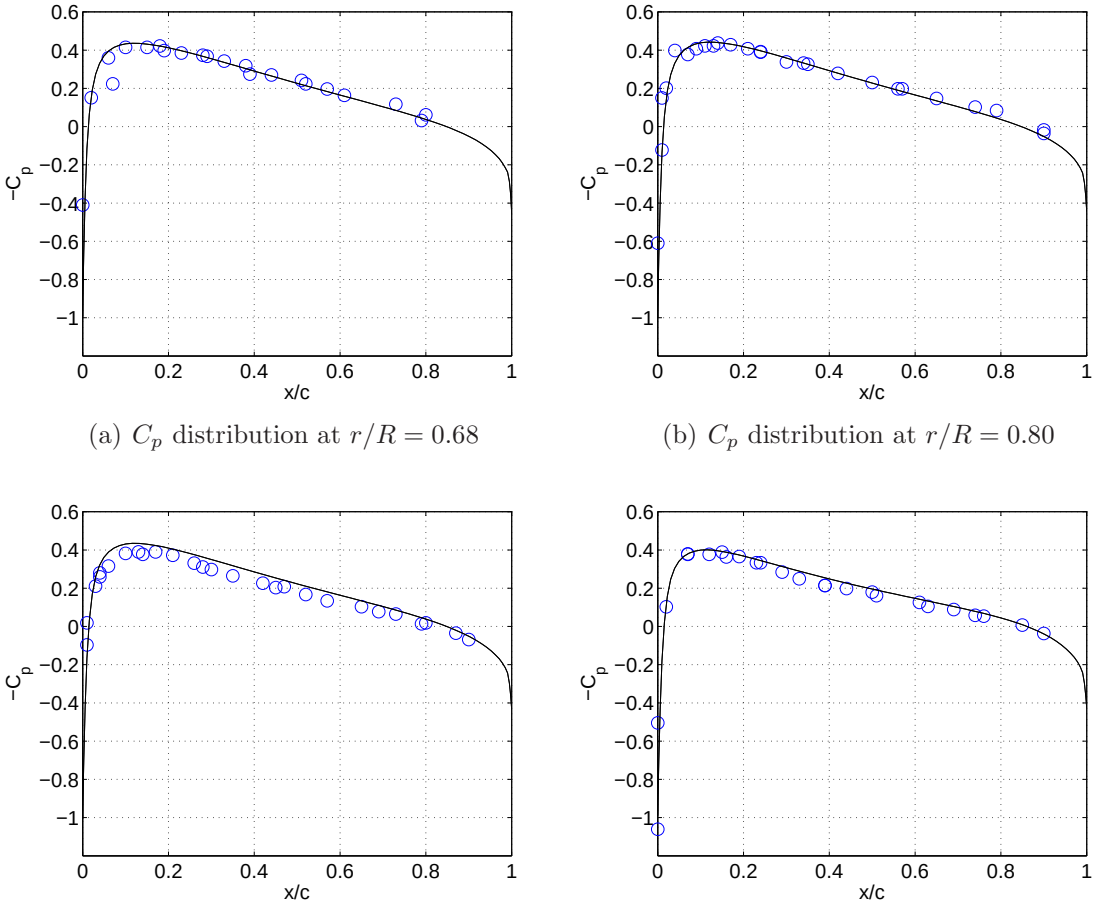

(a) C_p distribution at $r/R = 0.68$

(b) C_p distribution at $r/R = 0.80$

(c) C_p distribution at $r/R = 0.89$

(d) C_p distribution at $r/R = 0.96$

Figure 4.2: Coefficient of pressure distribution on a nonlifting rotor in hover using the JST dissipation scheme, $M_t = 0.52$, $\theta_c = 0°$: ○ denotes the experimental values of C_p and — represents the computed result.

The rotor is idealized as an infinitesimally thin actuator disk over which, there exists a pressure difference. In other words, consider an infinite number of blades of zero thickness with the mass flux assumed to be uniformly distributed over the area of radius R located at the center of the rotor disk. The actuator disk supports the thrust force that is generated by the rotation of the rotor blades. Power is required to generate this thrust, which is supplied by the shaft work on the rotor. The work done on the rotor leads to a gain in kinetic energy of the rotor slipstream and this energy

Case	M_{tip}	Ω (RPM)	C_T	Dissipation Scheme
1	0.439	1250	0.459	JST
2	0.439	1250	0.459	SLIP
3	0.877	2500	0.473	JST
4	0.877	2500	0.473	SLIP

Table 4.1: Thrust coefficients, C_T, for different tip Mach numbers at a collective pitch of $\theta_c = 8°$ from Caradonna & Tung (1981).

loss is called the induced power. One-dimensional momentum theory assumes that the flow field is incompressible and the loading on the actuator disk is constant. The use of this boundary condition requires as input the rotor radius, rotor disk center, the center of rotor wake at the outflow boundary and a known coefficient of thrust. In the present work, the center of the rotor disk is located at the coordinate $(0, 0, 0)$. The coefficient of thrust is taken from Caradonna & Tung (1981, page 45).

4.4.2 Lifting Rotor Results

Euler calculation of two lifting cases were performed for two different flow conditions. Each case was run with two different artificial dissipation schemes using the same overall geometry as described in section 4.3. The conditions of all these cases are presented in table 4.1.

In the first case, the tip Mach number is 0.439 with a collective pitch of 8 degrees. The angular velocity is 1250 RPM: this is a subsonic flow simulation. Figure 4.3 shows the computed coefficient of pressure distributions at four different spanwise locations using the JST and SLIP dissipation schemes respectively. The numerical results are in excellent agreement with the experimental data. Since this is a subsonic case, the flow solver does not have to capture discontinuities and the results from the two schemes are almost identical.

The second case has a tip Mach number of 0.877, also with a collective pitch of 8 degrees. The angular velocity for this case is 2500 RPM. This requires the flow solver to capture discontinuities near the blade tip. The results from both the JST and CUSP dissipation schemes are shown in figure 4.4.

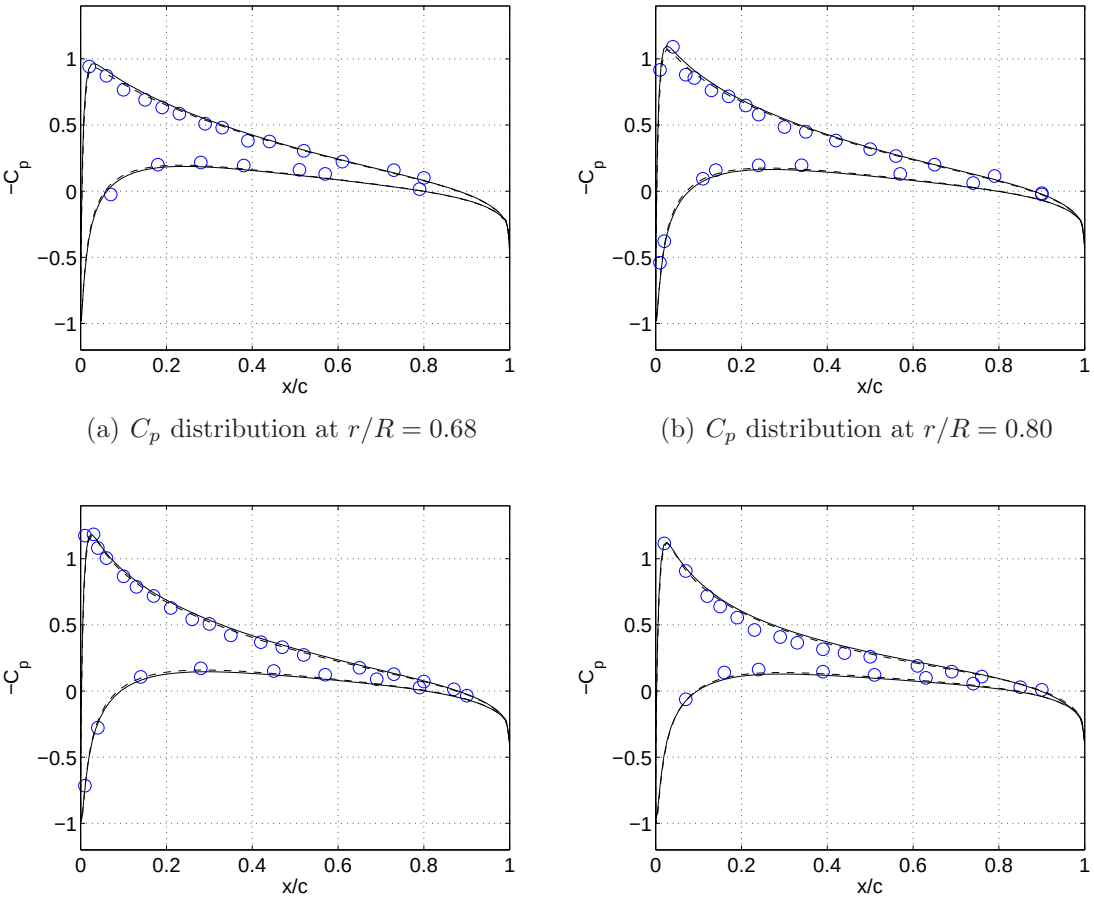

(a) C_p distribution at $r/R = 0.68$

(b) C_p distribution at $r/R = 0.80$

(c) C_p distribution at $r/R = 0.89$

(d) C_p distribution at $r/R = 0.96$

Figure 4.3: Coefficient of pressure distribution on a lifting rotor in hover, $M_t = 0.439$, $\theta_c = 8°$: ○ experimental values of C_p, — computed result using the JST dissipation scheme, – – computed result using the SLIP dissipation scheme.

Some differences can be found in this case. In the transonic regime, the shock captured by the SLIP scheme is sharper. This is to be expected since there is more numerical dissipation built into the JST scheme. The shock location computed by both schemes occur further downstream than the actual location recorded in the experiment. This can partly be explained by the fact that these results are from Euler calculations and the boundary layer thickness is not accounted for. Thus the effective thickness of the rotor blade is not as thick as it should be in viscous calculations. In viscous calculations and in real life, the boundary layer forces the flow to accelerate

quicker over the curvature past the leading edge. Note that the "Zierep singularity" (Zierep, 1966) is present in the result computed by the SLIP dissipation scheme. For this case, the results from Sheffer *et al.* (1997) also showed the same discrepancy in the shock location.

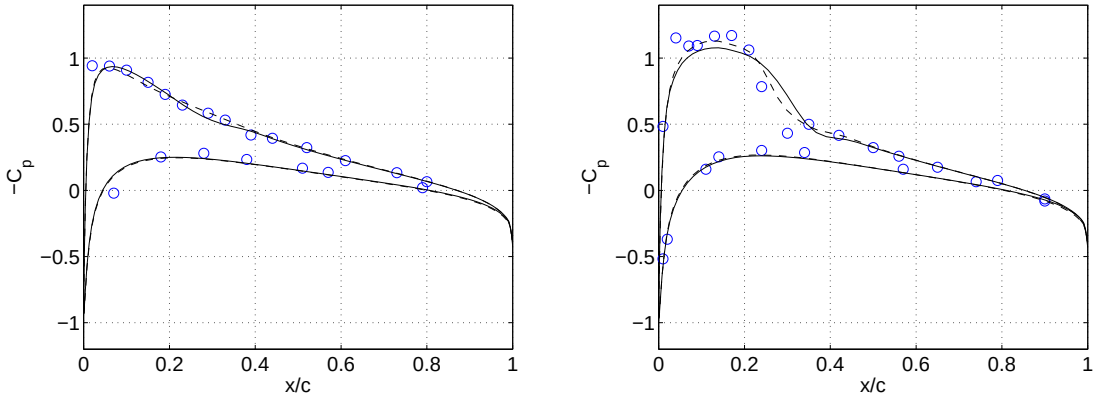

(a) C_p distribution at $r/R = 0.68$

(b) C_p distribution at $r/R = 0.80$

(c) C_p distribution at $r/R = 0.89$

(d) C_p distribution at $r/R = 0.96$

Figure 4.4: Coefficient of pressure distribution on a lifting rotor in hover, $M_t = 0.877$, $\theta_c = 8°$: ○ experimental values of C_p, — computed result using the JST dissipation scheme, – – computed result using the SLIP dissipation scheme.

4.5 Alternative Far-Field Boundary Condition

As mentioned in section 4.4.1, one-dimensional momentum theory has been applied for the lifting rotor calculations thus far. The argument is that the typical Riemann invariant far-field boundary condition forces the velocity to circulate and vanish near the bottom boundary (for a lifting rotor) and hence the downwash cannot develop as it should in an actual hovering rotor. Nevertheless, it is in fact possible to use the Riemann invariant boundary condition for the bottom boundary if the distance from the rotor to the bottom is far enough, typically many radii away from the rotor (at least five radii away), such that the top and bottom boundaries are indeed far fields, not the end of a computation box in the near field. The advantage of this approach is obvious since the thrust coefficient is not required beforehand. This is always true if one were to simulate the flow during the design stage of a helicopter. The simulation time is, however, much longer as the downwash requires a lot of time to become fully developed. This is true even when the residual plot shows that the solution has converged. Authors who have used this real far-field boundary condition have reported that many thousands, or in some case tens of thousands, iterations are required for the flow to be fully considered as converged (Allen, 2004*b*).

Figure 4.5 shows a mesh with the top and bottom boundaries at a distance approximately five spans away from the rotor. The subsonic lifting rotor case mentioned previously was calculated using this mesh. Figures 4.6, 4.7 and 4.8 show the development of the flow field after six different time intervals from 500 up to 4,000 multigrid cycles. It can be observed that there is still slight change in the flow field after 3,500 multigrid cycles, and this confirms the findings that other researchers have also experienced. It is natural to compare this approach to the one-dimensional momentum boundary condition approach. With the one-dimensional momentum approach, solution converges far quicker but the thrust coefficient needs to be known in advance. This is usually not the case during the design stage, therefore using the true far-field boundary is a safer and preferred approach for hover case.

4.6 Closing Remarks

This chapter has shown that the flow solver is capable of predicting aerodynamic quantities of a rotor in hover. Different far-field boundary conditions have been tested. The conclusion regarding this matter is that one should use top and bottom far fields that properly extend at least up to the distance of at least five radii away from the rotor. Hover simulation is not as straightforward as it first appears because of the time required to resolve the downwash velocity. Monitoring the the residual is not a true indicator of the state of convergence for hover case.

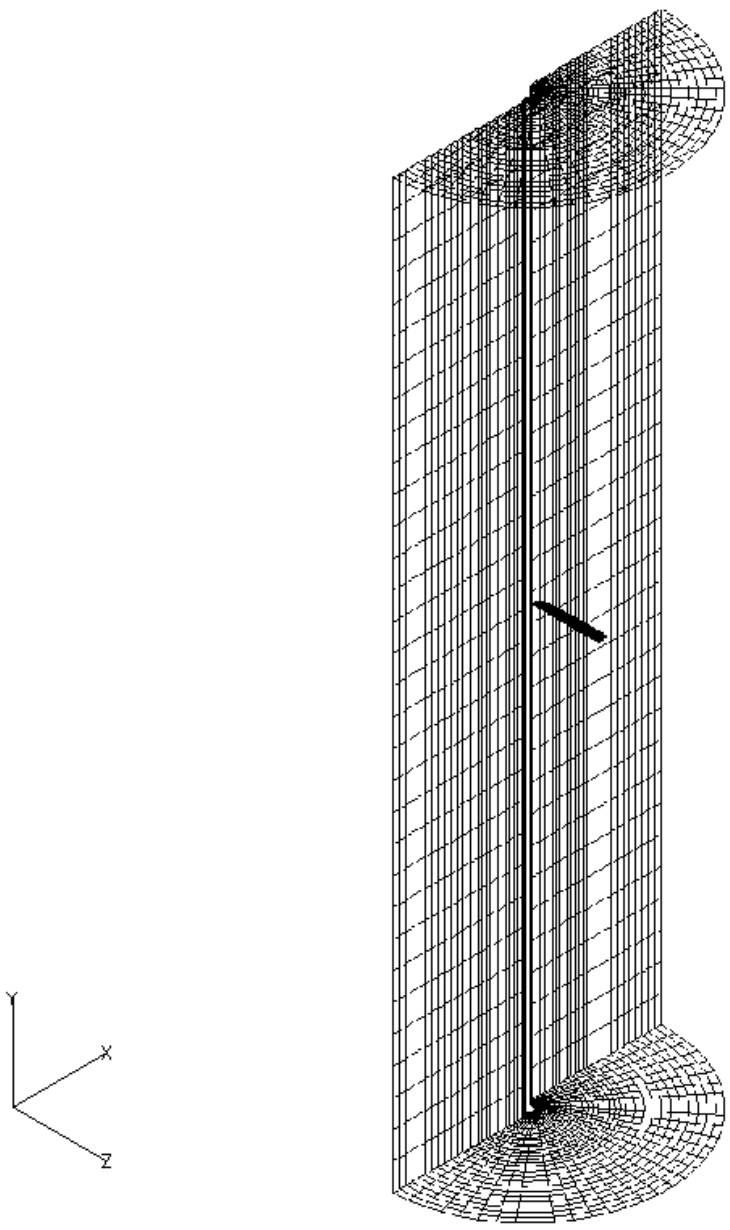

Figure 4.5: Hover mesh with top and bottom boundaries at distance approximately five radii from the rotor.

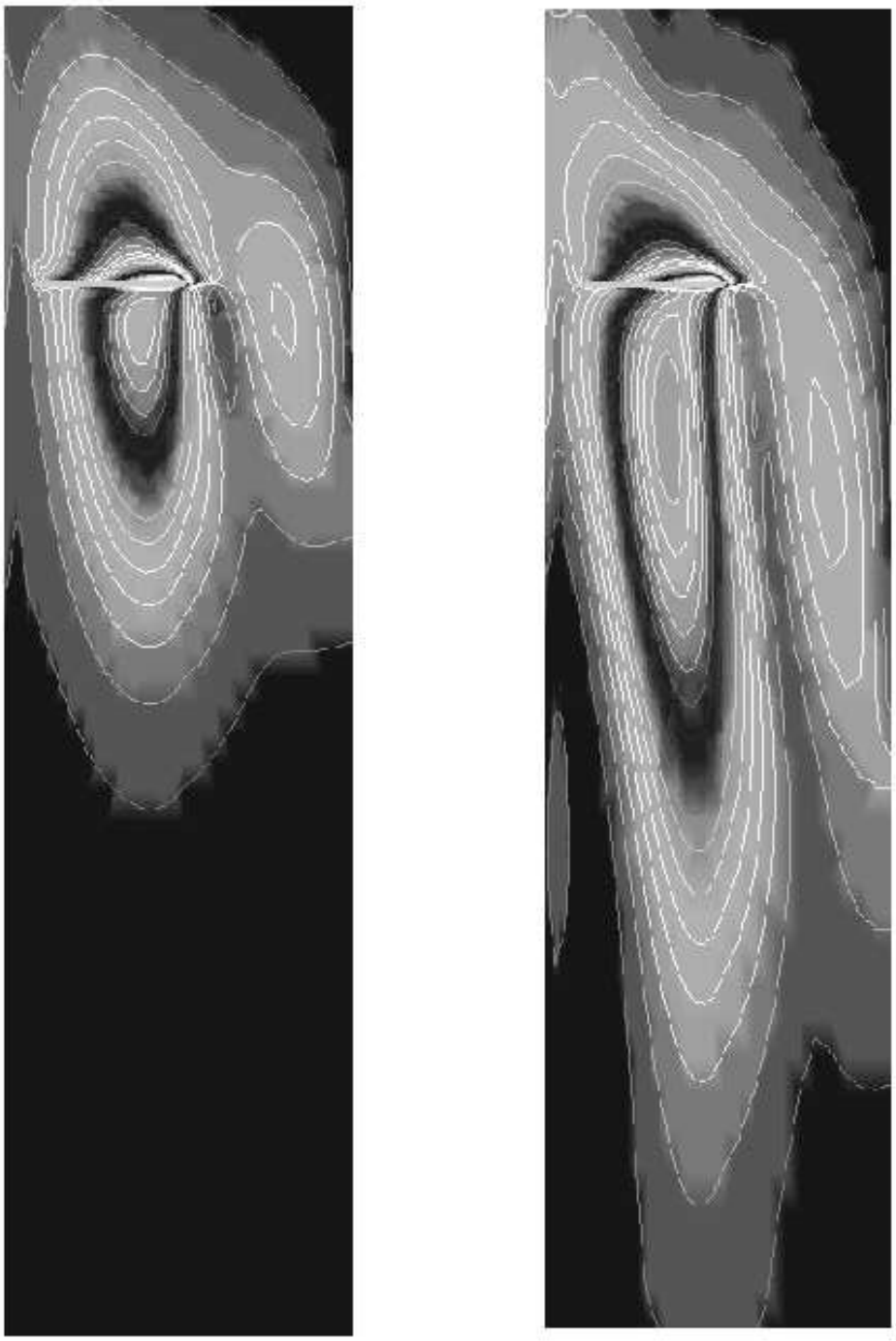

(a) 500 steps (b) 1,500 steps

Figure 4.6: Development of the flow field over time after 500 and 1,500 time steps, $M_t = 0.439$, $\theta_c = 8°$.

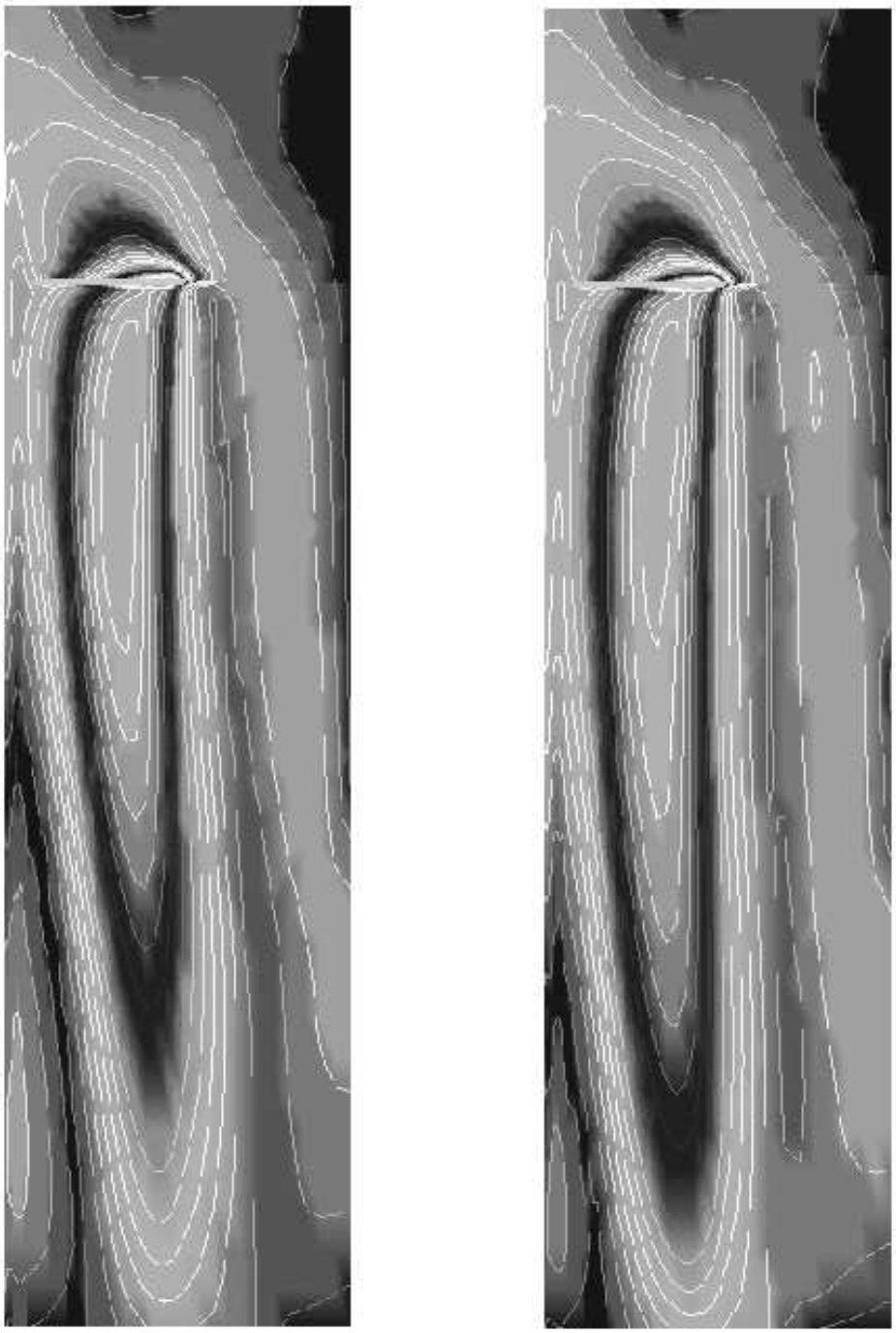

(a) 2,250 steps (b) 3,000 steps

Figure 4.7: Development of the flow field over time after 2,250 and 3,000 time steps, $M_t = 0.439$, $\theta_c = 8°$.

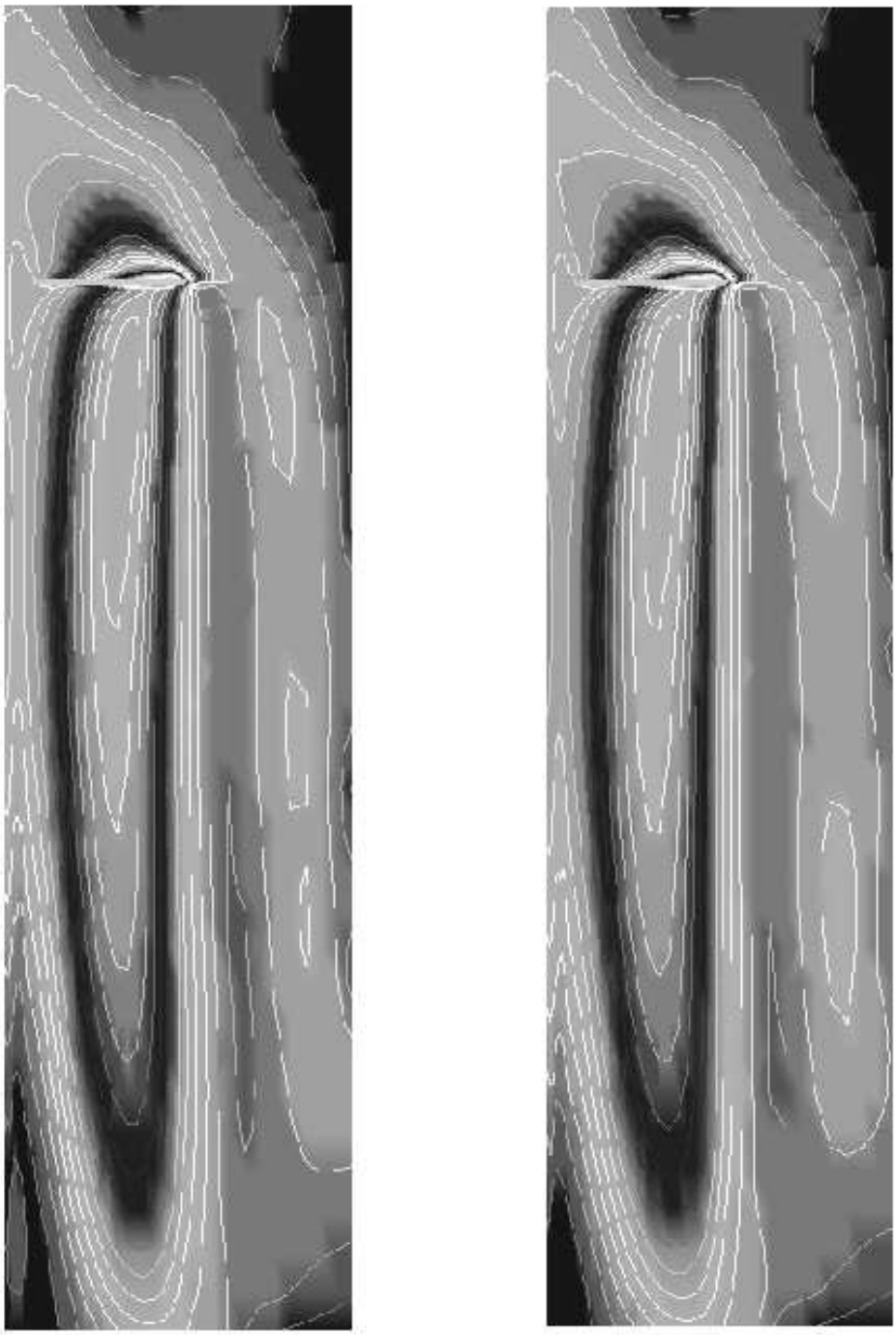

(a) 3,500 steps (b) 4,000 steps

Figure 4.8: Development of the flow field over time after 3,500 and 4,000 time steps, $M_t = 0.439$, $\theta_c = 8°$.

Chapter 5

Forward Flight Simulations

This chapter is the core of this thesis: simulation of helicopter in forward flight. One of the most difficult aspects of helicopter simulation is in the forward flight regime, especially low speed flight. If one can significantly save computational expense by applying the Time Spectral method, computational power can be assigned for other aspects of helicopter flow simulations such as grid adaptation near the vortical regions or strong coupling of the blades. This chapter shows that it is possible to accurately predict the unsteady aerodynamics of a rotor in forward flight using the Time Spectral method with the algorithm derived in section 3.2.

5.1 Complication in Forward Flight Regime

Forward flight is normally characterized by the advance ratio,

$$\mu = \frac{U_\infty}{\Omega R},$$

where U_∞ is the forward flight speed, Ω is the angular velocity of the rotor, and R is the rotor radius. Typical values of the advance ratio are $\mu \leq 0.4$.

In forward flight, a component of free-stream velocity U_∞ (this is the same as the forward velocity of the helicopter) adds or subtracts from the rotational velocity at

every part of the blade. The blade tip velocity U_t now becomes

$$U_t = \Omega R + U_\infty \sin\psi.$$

where ψ is the azimuthal angle of the blade. ψ is defined as zero in the downstream direction of the rotor. This angle is measured from downstream to the blade span axis. Hence for constant rotational speed,

$$\psi = \Omega t.$$

It is commonly assumed that the direction of the rotor rotation is in the counter-clockwise direction when viewed from above. However, for the work presented in this thesis, the rotor rotation direction is in the clockwise direction i.e., the left side of the rotor disk (when viewed from above) is the advancing side and right side is the retreating side as illustrated in figure 5.1.

5.2 Mesh Topology

The mesh used for calculations in this chapter is an O–H type mesh as mentioned in the chapter 4 but simulations of helicopter in forward flight requires the mesh of the entire rotor, rather than a section of the rotor as in the hover case. Effectively, this is still a single block mesh for each blade. For all the blades other than the first one (the first blade corresponds to the azimuth $\psi = 90°$), the coordinates are rotated in the clockwise direction in the x–z plane. For instance, the coordinates of the j-th blade in an N-bladed rotor for $1 < j \leq N$ in relation to the first blade are as follows:

$$\begin{bmatrix} x_1 \\ x_2 \\ x_3 \end{bmatrix}_{j\text{-th blade}} = \begin{bmatrix} \cos\left[\frac{2\pi(j-1)}{N}\right] & 0 & -\sin\left[\frac{2\pi(j-1)}{N}\right] \\ 0 & 0 & 0 \\ \sin\left[\frac{2\pi(j-1)}{N}\right] & 0 & \cos\left[\frac{2\pi(j-1)}{N}\right] \end{bmatrix} \cdot \begin{bmatrix} x_1 \\ x_2 \\ x_3 \end{bmatrix}_{\text{Blade 1}}$$

The first time instance corresponds to the first blade. As an example, for the simulation of a two-bladed rotor with 12 time instances, the corresponding positions of

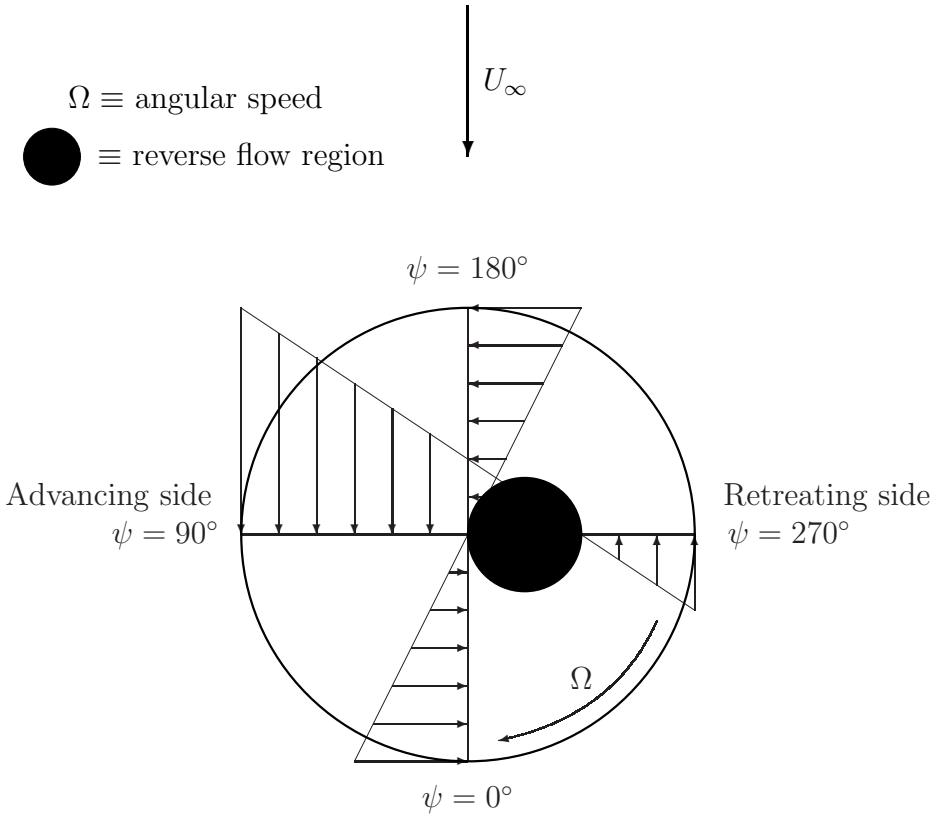

Figure 5.1: Schematic diagram of incident velocity normal to the leading edge of the rotor blade in forward flight.

each blade are shown in table 5.1

Figure 5.2 shows the mesh of a two-bladed rotor at the first time instance. There is a singularity point at the center of the mesh. As a result, a hole needs to be cut through the middle of the cylinder along the y axis.

Furthermore, the blades of a real helicopter are normally twisted along their length (linear twist) but the blades simulated in this chapter are rigid and the calculations do not account for aeroelastic effects. The current simulations also do not include an articulated rotor, nor the fuselage and tail rotor. Therefore the flight test data will not be compared with the simulation results. Instead, the forward flight simulation results presented in the following sections are compared to the wind tunnel experiment

Azimuthal angle, ψ		
Mode	Blade 1	Blade 2
1	90°	270°
2	120°	300°
3	150°	330°
4	180°	0°
5	210°	30°
6	240°	60°
7	270°	90°
8	300°	120°
9	330°	150°
10	0°	180°
11	30°	210°
12	60°	240°

Table 5.1: Azimuthal angle, ψ, corresponding to blades at different frequencies.

of a model helicopter rotor in forward flight by Caradonna *et al.* (1984).

5.3 Boundary Conditions

At the rotor hub ($z \rightarrow 0$), a solid body boundary condition is used: flow tangency for Euler calculation and no-slip for RANS calculation. Riemann invariant boundary condition and direct extrapolation of the variables have also been tested, but these approaches do not make noticeable differences to the overall results. On the blade surface, a solid body boundary condition is also applied.

There are three far-field boundaries in this case, the outer boundary, and the top and bottom boundaries. At these far-field boundaries, the one-dimensional Riemann invariant type boundary condition is imposed. The first case presented is a nonlifting rotor and therefore there is no special treatment required for the lower boundary as it is needed in the lifting hover cases. In the halo cells at the side boundaries the values of the flow variables, mesh geometry and mesh velocities are exchanged between the blade sectors at every time step.

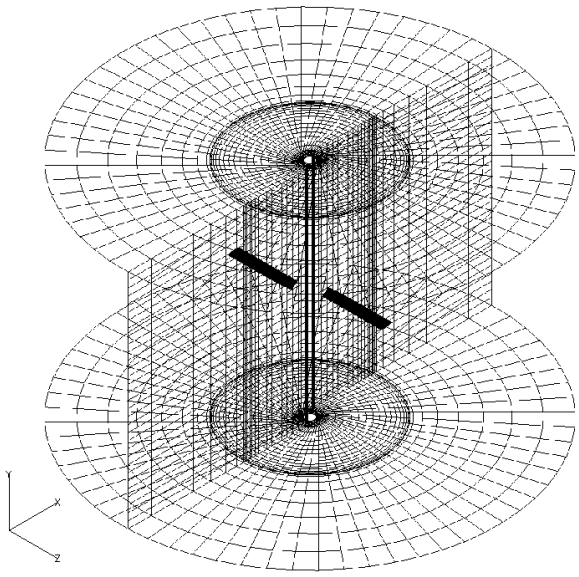

(a) Isometric view

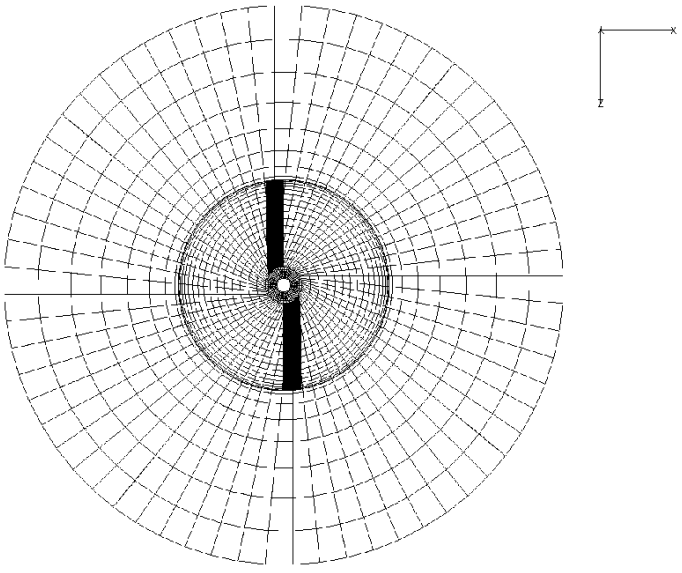

(b) Top view

Figure 5.2: $128 \times 48 \times 32$ computational mesh cells per blade sector modeling untwisted, untapered, two-bladed NACA 0012 rotor with an aspect ratio of seven for Euler simulation of forward flight case.

5.4 Nonlifting Model Rotor in Forward Flight

The first forward flight case is the simulation of the flow around isolated model helicopter rotor in forward flight without pitching and flapping motion. The experimental data is taken from the experiment by Caradonna *et al.* (1984). The blades had an NACA 0012 section with zero angle of attack. The rotor was seven feet in diameter and 6 inches in chord constructed almost entirely of balsa and carbon/epoxy composites. The aspect ratio of the blades was seven.

The tip Mach number for the first case is 0.8 with the advance ratio set at $\mu = 0.2$. This advance ratio of 0.2 corresponds to a Mach number in the unperturbed flow of $\mathrm{M}_0 = 0.16$.

For the Euler calculations, the number of cells per blade sector is $128 \times 48 \times 32$ with 24 cells distributed along the blade, 128 cells in the chordwise direction, 48 cells in the normal direction and 32 cells in the spanwise direction. Similarly, $192 \times 64 \times 48$ cells are used for RANS calculations with 32 cells distributed along each blade.

5.4.1 Simulation Results

Figure 5.3 shows the variation of the local pressure coefficient around a blade section located near the tip on the advancing side at $r/R = 0.893$ at different values of azimuthal angles ($0° \leq \psi \leq 180°$) from the Euler calculation with the JST and CUSP dissipation schemes. These two calculations used 12 time instances ($N = 12$), which corresponds to five frequencies. A very good agreement of the calculated pressure coefficient with the experimental result can be observed. The calculations were performed on an SGI™Origin™300 machine using 8 processors and also on an HPC BoxCluster ML machine with four Intel® Core™2 Duo processors. The SGI™machine has 64-bit 600 MHz processors with 32 GB of shared memory. Each simulation took less than 6 hours to complete 300 multigrid cycles on the SGI™machine and approximately 55 minutes on the HPC machine.

Figure 5.4 shows the results from the RANS calculations using the JST and CUSP dissipation schemes with the Baldwin–Lomax turbulence model. The reference Reynolds number for this case is $\mathrm{Re} = 2.89 \times 10^6$ based on the chord length at

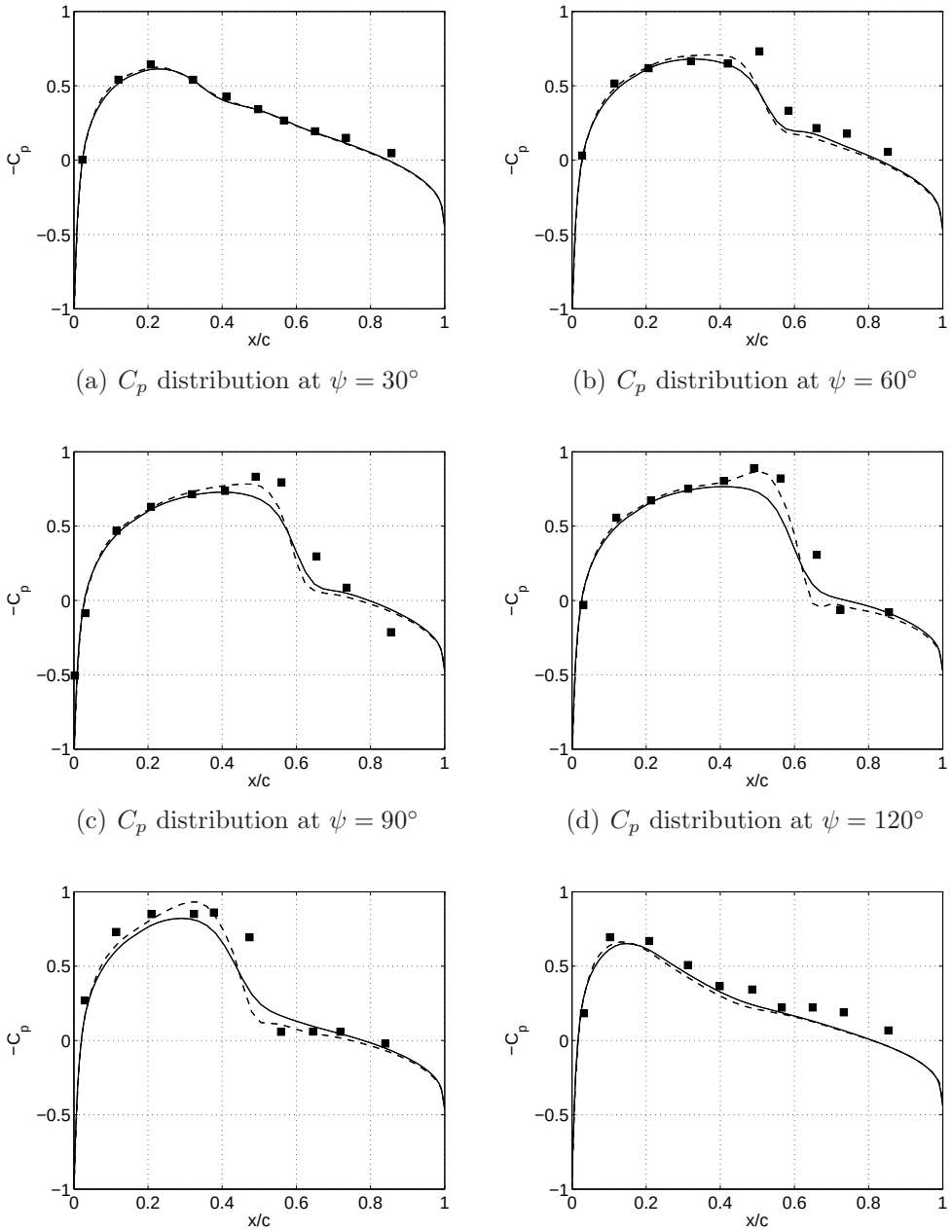

(a) C_p distribution at $\psi = 30°$

(b) C_p distribution at $\psi = 60°$

(c) C_p distribution at $\psi = 90°$

(d) C_p distribution at $\psi = 120°$

(e) C_p distribution at $\psi = 150°$

(f) C_p distribution at $\psi = 180°$

Figure 5.3: Coefficient of pressure distribution on a blade section at $r/R = 0.893$ on a nonlifting rotor in forward flight from Euler calculation, $M_t = 0.8$, $\theta_c = 0°$, $\mu = 0.2$, $N = 12$: ■ experimental values of C_p, — computed result using the JST dissipation scheme, – – computed result using the CUSP dissipation scheme.

the blade tip. Again, the results display very good agreement with the experimental data. The RANS calculations were run on the SGI^{TM}Origin^{TM}300 machine using 8 processors. A single viscous calculation took approximately 40 hours to complete with 12 times instances to complete 500 multigrid cycles. Comparing these numbers to simulations mentioned in section 2.1, one can observe the huge computational saving of the Time Spectral method in comparison with other traditional implicit time marching schemes.

For this nonlifting case, the shock location at the azimuthal angles $\psi = 60°$, $90°$, $120°$ and $150°$ occurs earlier than the actual locations measured from the experiment. This is true for both Euler and RANS calculations. The viscous effects do not appear to alter the shock location in comparison with the results from Euler calculations. The solution obtained with the CUSP dissipation scheme produces sharper shock structure than the one with the JST scheme. This is expected since the JST scheme is a scalar dissipation scheme while the CUSP scheme uses a characteristic decomposition. Thus the JST dissipation scheme cannot perform as well as the CUSP scheme as mentioned in section 3.7.3. In comparison to the calculations performed on the SGI^{TM}machine, the calculations performed on the HPC^{TM}machine with the JST and CUSP dissipation schemes took four hours and 45 minutes, and five hours respectively.

5.5 Accuracy of the Time Spectral Method

To test the accuracy of the Time Spectral method, the same forward flight calculations were performed with only four time instances ($N = 4$). Results from Euler and RANS calculations at the azimuthal angles of $90°$ and $180°$ are shown in figures 5.5 and 5.6 respectively. One can observe that even with a small number of modes (only one in this case), i.e. as low as only four time instances, the results still show excellent agreement compared to the experimental data. This implies that there is only one dominant frequency in this particular test case. Nevertheless, this demonstrates that the Time Spectral is indeed a highly accurate scheme if there are enough number of modes to resolve the dominant frequencies of the flow field.

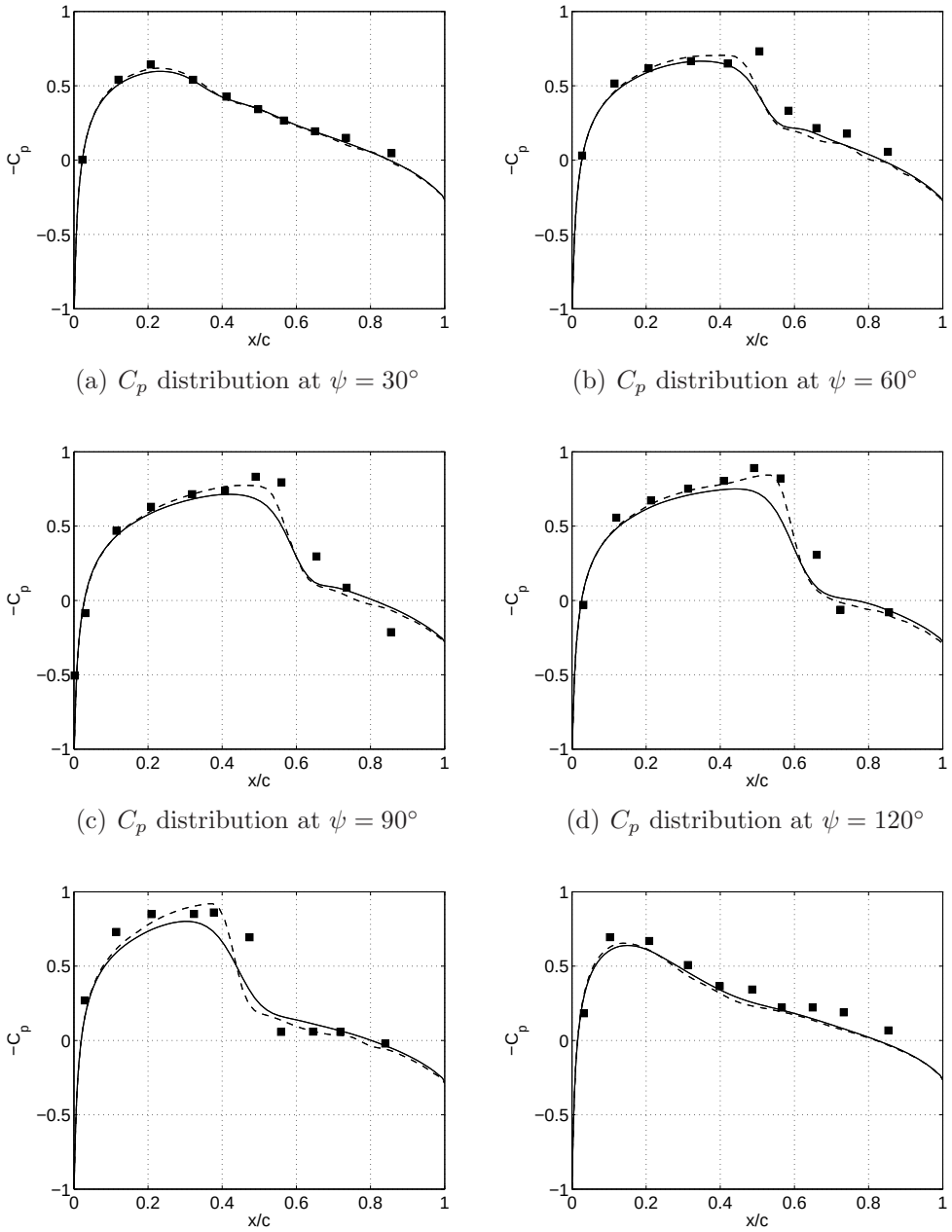

(a) C_p distribution at $\psi = 30°$

(b) C_p distribution at $\psi = 60°$

(c) C_p distribution at $\psi = 90°$

(d) C_p distribution at $\psi = 120°$

(e) C_p distribution at $\psi = 150°$

(f) C_p distribution at $\psi = 180°$

Figure 5.4: Coefficient of pressure distribution on a blade section at $r/R = 0.893$ on a nonlifting rotor in forward flight including the viscous effects, $\mathrm{M}_t = 0.8$, $\theta_c = 0°$, $\mu = 0.2$, $N = 12$: ■ experimental values of C_p, — computed result using the JST dissipation scheme, – – computed result using the CUSP dissipation scheme.

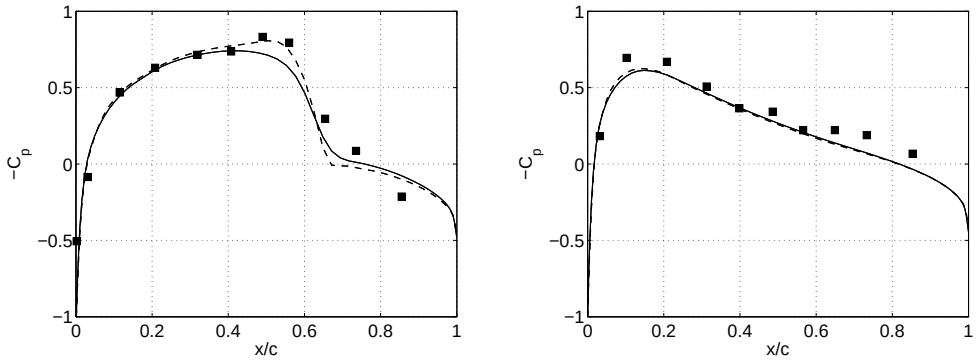

(a) C_p distribution at $\psi = 90°$ (b) C_p distribution at $\psi = 180°$

Figure 5.5: Coefficient of pressure distribution on a blade section at $r/R = 0.893$ on a nonlifting rotor in forward flight from Euler calculations, $N = 4$, $\mathrm{M}_t = 0.8$, $\theta_c = 0°$, $\mu = 0.2$: ■ experimental values of C_p, — computed result using the JST dissipation scheme, – – computed result using the CUSP dissipation scheme.

5.6 Time Lagged Periodic Boundary Condition

When Fourier based time integration is used for rotorcraft simulation, it is possible to use only one sector of a rotor for forward flight calculation by applying the boundary condition first proposed by Ekici *et al.* (2008) at the upstream and downstream boundaries:

$$\mathbf{w}(t) = \mathbf{w}(t - \Delta t) \tag{5.1}$$

where the current solution at point a is the same at point b at an earlier time (see figure 5.7). Although the work in this thesis uses a Cartesian coordinate system, it is simpler to use a cylindrical coordinate system to demonstrate the idea behind (5.1). Depending on the number of blades in a given rotor, the formulation can be generalized for an N-bladed rotor as follows:

$$\mathbf{w}(r, \psi, z, t) = \mathbf{w}\left(r, \psi - \frac{2\pi}{N}, z, t - \frac{T}{N}\right) \tag{5.2}$$

where N is the number of blades of a rotor, T is the period, and $\Delta t = T/N$.

Figure 5.7 shows the schematic diagram of a four-bladed rotor. The solid lines represent the boundaries where the flow variables at point a at the time instance

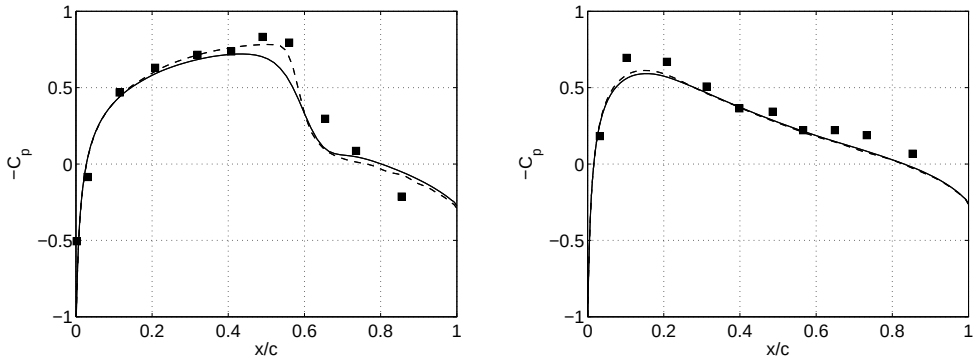

(a) C_p distribution at $\psi = 90°$ (b) C_p distribution at $\psi = 180°$

Figure 5.6: Coefficient of pressure distribution on a blade section at $r/R = 0.893$ on a nonlifting rotor in forward flight from Euler calculations, $N = 4$, $M_t = .8$, $\theta_c = 0°$, $\mu = 0.2$: ■ experimental values of C_p, — computed result using the JST dissipation scheme, – – computed result using the CUSP dissipation scheme.

shown here are the same as the flow variables at point b at the earlier time instance as described in (5.2).

Figures 5.8 and 5.9 show the Euler and RANS calculation results of the nonlifting rotor in forward flight as in section 5.4. From the plots, the results obtained from calculating one sector of the rotor in comparison to the results computed from the entire rotor are identical. For the calculations with the JST dissipation scheme, the number of multigrid steps required for convergence is 300 multigrid steps for the Euler calculation and 500 multigrid steps for the RANS calculation. With the CUSP dissipation scheme, the Euler calculation still requires 300 multigrid steps to obtain convergence, however, the RANS calculation requires 800 multigrid steps to obtain convergence. When 500–700 multigrid steps are used for the RANS calculation with the CUSP scheme, the solution still contain oscillations and the periodic steady state is still not yet established.

Figures 5.10 and 5.11 show the Euler calculation results obtained using one blade and the entire rotor respectively. This is a nonlifting case and the experimental data is also found in Caradonna *et al.* (1984), but with a different blade aspect ratio, advance ratio and tip Mach number compared to the previous case. For this case, the aspect ratio is 7.125, the advance ratio is 0.25 and the tip Mach number

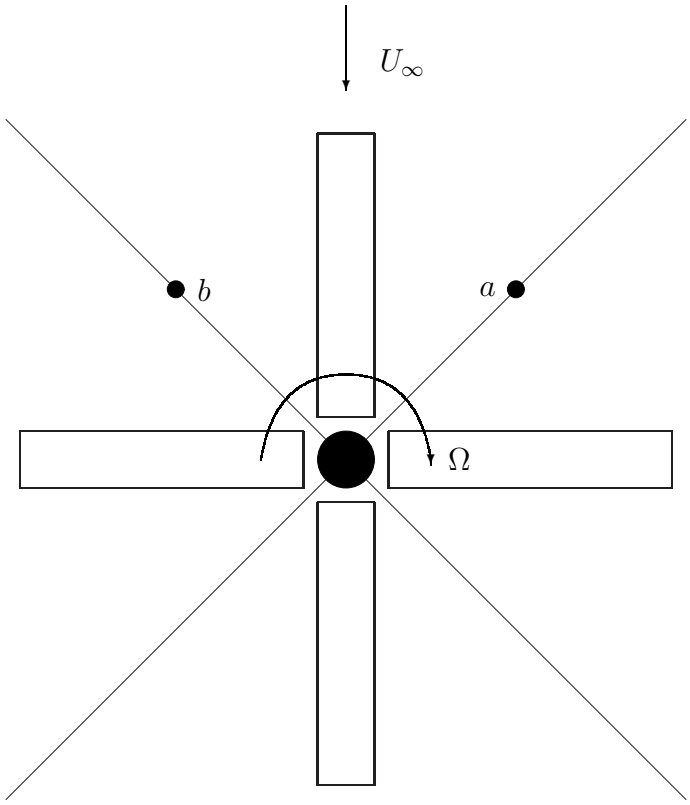

Figure 5.7: Schematic diagram for time-lagged periodic boundary condition of a single blade sector in forward flight

is 0.7634. This is a higher speed forward flight, so the shock strength observed is slightly stronger. The mesh size for this calculation is the same as in the previous case with $128 \times 48 \times 32$ mesh cells. Both the JST and CUSP dissipation schemes were used. The simulations required 400 multigrid cycles using 12 time instances before convergence was observed. Similar to the previous results, the shock location occurs earlier than the location measured in the experiment.

The subsequent calculations from this point onwards use the time-lagged boundary condition with only one blade sector.

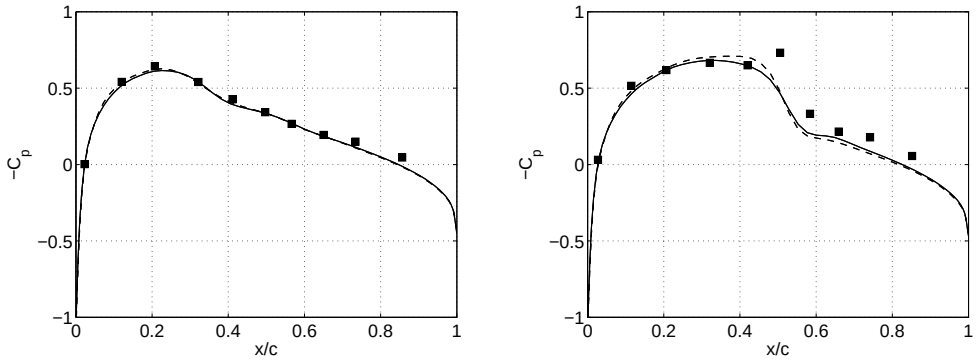

(a) C_p distribution at $\psi = 30°$

(b) C_p distribution at $\psi = 60°$

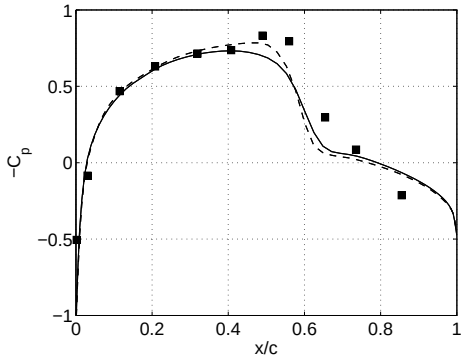

(c) C_p distribution at $\psi = 90°$

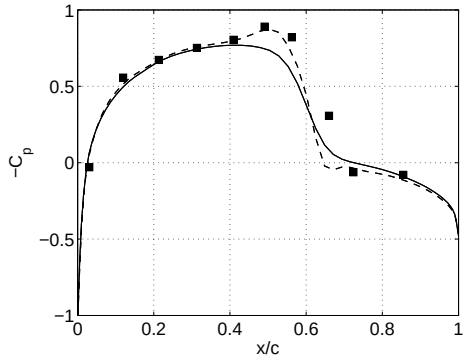

(d) C_p distribution at $\psi = 120°$

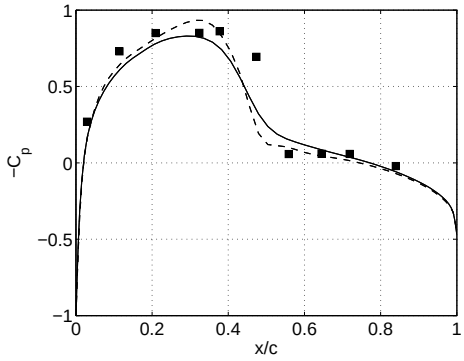

(e) C_p distribution at $\psi = 150°$

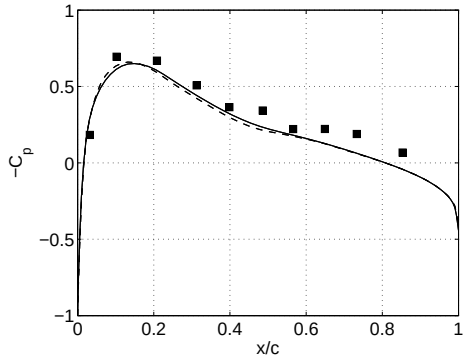

(f) C_p distribution at $\psi = 180°$

Figure 5.8: Coefficient of pressure distribution on a blade section at $r/R = 0.893$ on a nonlifting rotor in forward flight from the Euler calculation using one sector of a rotor, $M_t = 0.8$, $\theta_c = 0°$, $\mu = 0.2$, $N = 12$: ■ experimental values of C_p, — computed result using the JST dissipation scheme, – – computed result using the CUSP dissipation scheme.

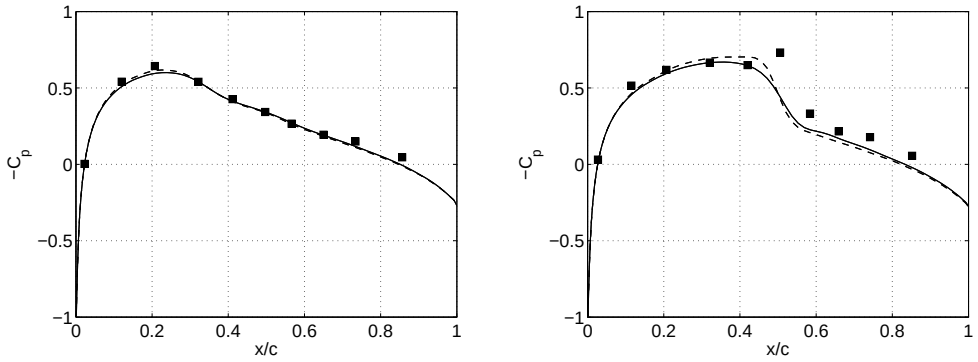

(a) C_p distribution at $\psi = 30°$

(b) C_p distribution at $\psi = 60°$

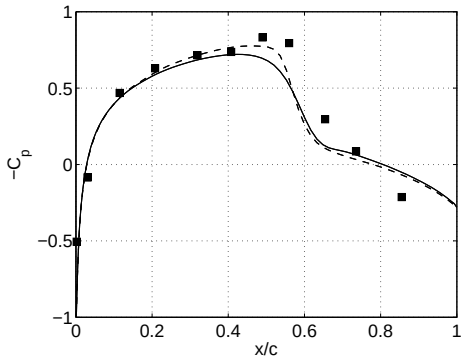

(c) C_p distribution at $\psi = 90°$

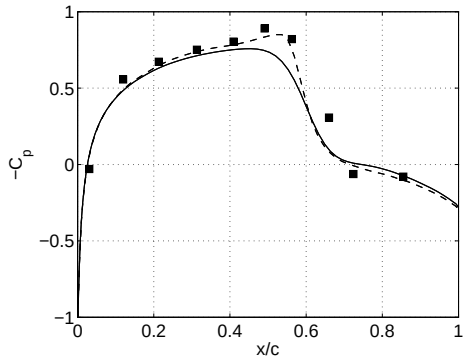

(d) C_p distribution at $\psi = 120°$

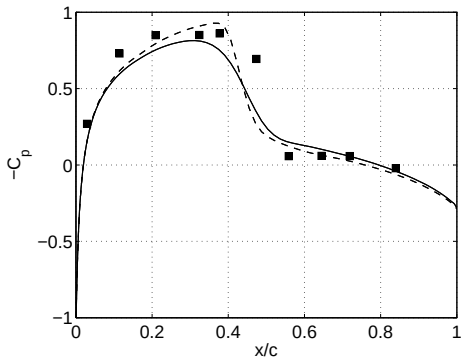

(e) C_p distribution at $\psi = 150°$

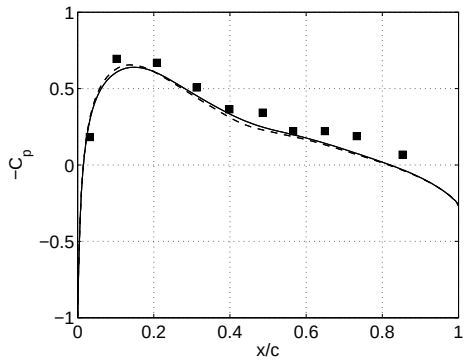

(f) C_p distribution at $\psi = 180°$

Figure 5.9: Coefficient of pressure distribution on a blade section at $r/R = 0.893$ on a nonlifting rotor in forward flight including the viscous effects using one sector of the rotor, $\mathrm{M}_t = 0.8$, $\theta_c = 0°$, $\mu = 0.2$, $N = 12$: ■ experimental values of C_p, — computed result using the JST dissipation scheme, – – computed result using the CUSP dissipation scheme.

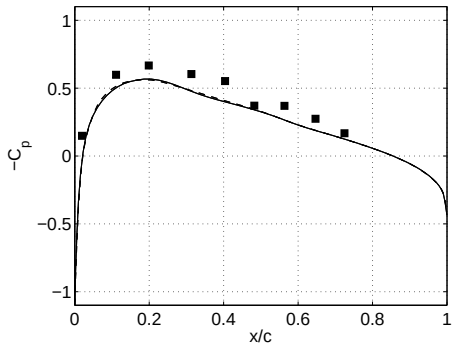

(a) C_p distribution at $\psi = 30°$

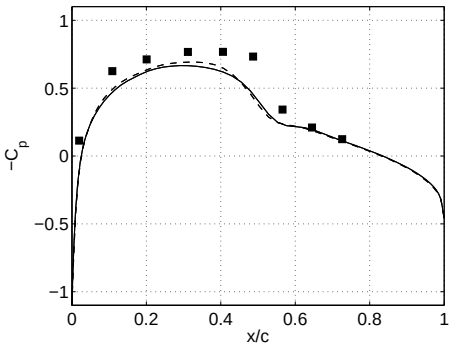

(b) C_p distribution at $\psi = 60°$

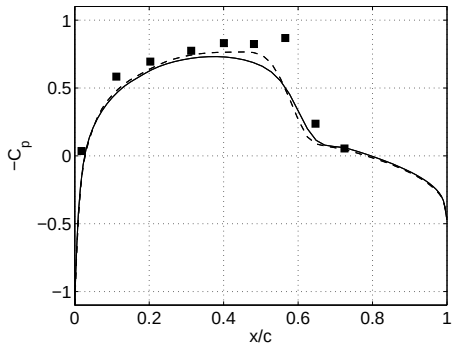

(c) C_p distribution at $\psi = 90°$

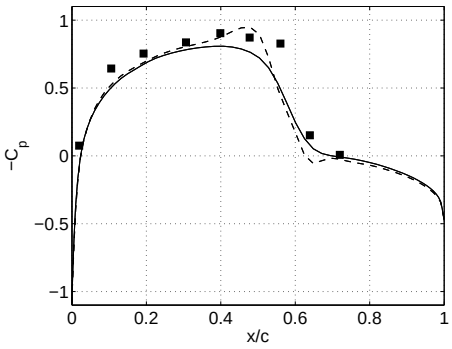

(d) C_p distribution at $\psi = 120°$

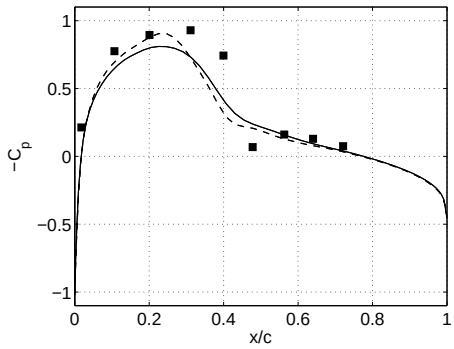

(e) C_p distribution at $\psi = 150°$

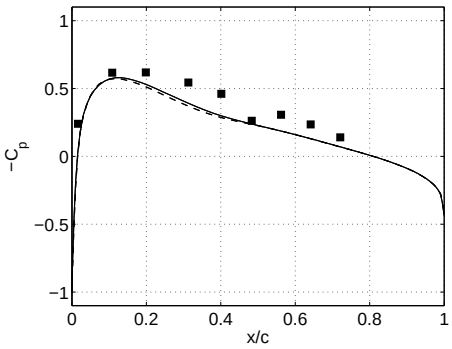

(f) C_p distribution at $\psi = 180°$

Figure 5.10: Coefficient of pressure distribution on a blade section at $r/R = 0.88$ on a nonlifting rotor in forward flight from Euler calculations using one sector of the rotor, $M_t = 0.7634$, $\theta_c = 0°$, $\mu = 0.25$, $N = 12$, aspect ratio = 7.125 with $128 \times 48 \times 32$ mesh cells: ■ experimental values of C_p, — computed result using the JST dissipation scheme, – – computed result using the CUSP dissipation scheme.

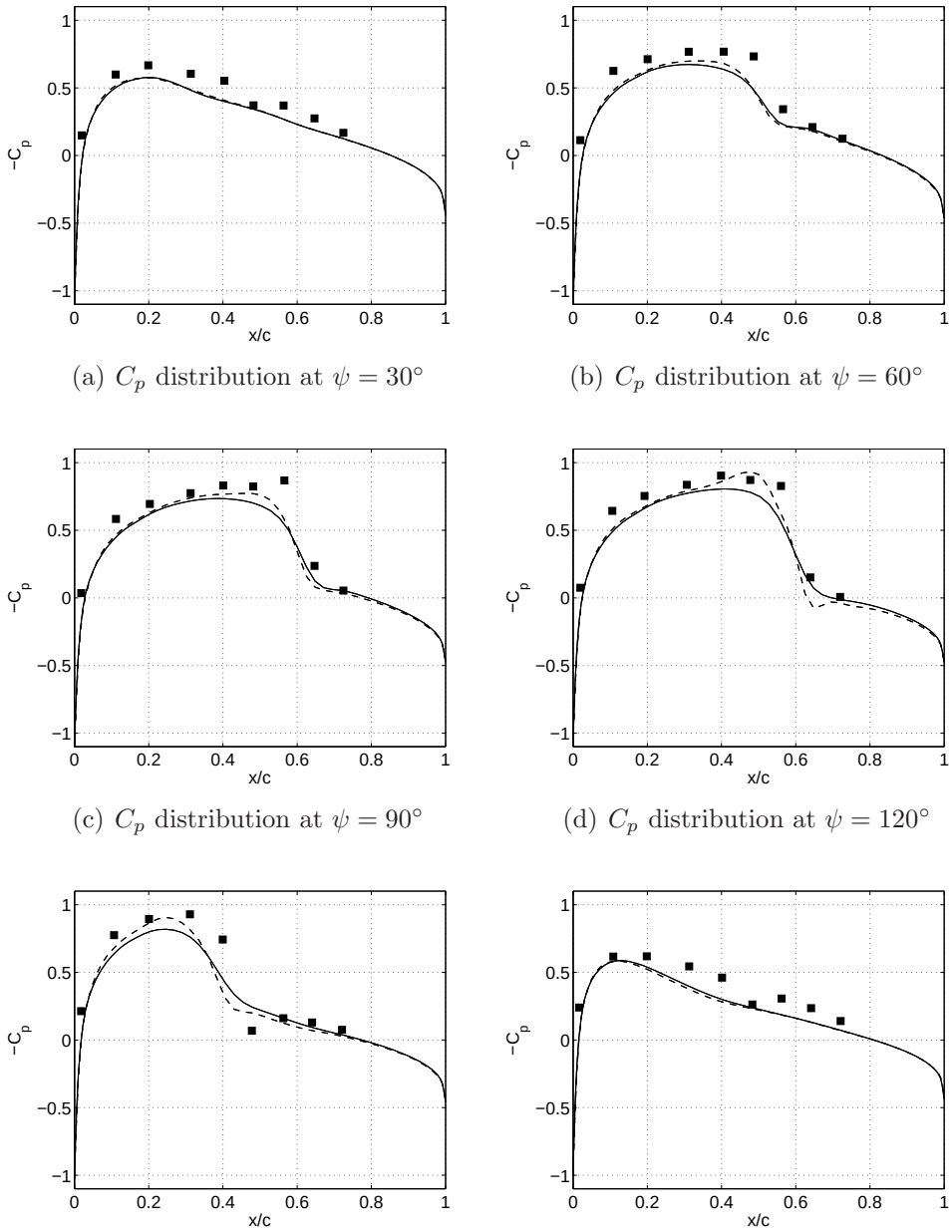

(a) C_p distribution at $\psi = 30°$

(b) C_p distribution at $\psi = 60°$

(c) C_p distribution at $\psi = 90°$

(d) C_p distribution at $\psi = 120°$

(e) C_p distribution at $\psi = 150°$

(f) C_p distribution at $\psi = 180°$

Figure 5.11: Coefficient of pressure distribution on a blade section at $r/R = 0.88$ on a nonlifting rotor in forward flight from Euler calculations using an entire rotor, $M_t = 0.7634$, $\theta_c = 0°$, $\mu = 0.25$, $N = 12$, aspect ratio = 7.125 with $128 \times 48 \times 32$ mesh cells: ■ experimental values of C_p, — computed result using the JST dissipation scheme, – – computed result using the CUSP dissipation scheme.

5.7 Lifting Rotor in Forward Flight

In this section, calculation results for a lifting rotor in forward flight is compared to the numerical simulation of Professor Chris Allen of the University of Bristol. The geometry for this test case is the same as the lifting hover case (Caradonna & Tung, 1981). The aspect ratio is six with an NACA 0012 blade section, and the collective pitch is 8 degrees. The tip Mach number is set at 0.7 and the advance ratio, μ, is 0.2857. This corresponds to a forward flight Mach number of 0.2.

This test case has been chosen for a number of reasons. The primary reason is that there is no blade motion, i.e. the blades are completely rigid with no allowance for aeroelasticity effects and the rotor hub is not articulated. Additionally, simulations by Allen used 4 million mesh points with 60 time steps per revolution, and 70 four-level V-cycle multigrid inner iterations for each time step. The time integration for this work was the widely used BDF (Jameson, 1991). Thus Allen's results seem accurate enough for comparison purposes. His past work has been thorough and he has consistently obtained good agreement between his numerical results and the experimental data. Lastly, the number of mesh cells used in the current work is approximately 200,000 per blade sector for the smallest case. While this relatively small number of mesh cells may not be able to fully resolve all details of the correct flow field, the results indicate that the prediction of aerodynamic quantities such as the coefficient of pressure, is remarkably accurate for the mesh size.

The quantity compared here is the load variation on each blade around the azimuth. Allen defined the force coefficient for each blade as

$$C_L = \frac{F_y}{\frac{1}{2}\rho \left(\Omega R\right)^2 cR} \tag{5.3}$$

where c is the chord at the tip (the chord is constant along the radius in this case), F_y is the force in the y direction, Ω is the angular velocity and the term cR represents the surface area of the blade. The subscript L indicates the lifting load. It is different from the coefficient of thrust in that this quantity is only for one blade, not for the complete rotor as one would associate with the thrust.

5.7.1 Simulation Results

Figures 5.12 and 5.13 show the comparison of the load variation computed by the Time Spectral method with the JST and CUSP dissipation schemes, and the data that has been supplied by Professor Allen.

Only one sector of a rotor is used in this calculation using the time-lagged periodic boundary condition from (5.2). Four cases for each scheme are compared with different combinations of the number of mesh cells and time instances. The cases are summarized in table 5.2. The number of time instances used in the calculations are 12 for cases 1–3 and 18 for case 4 as indicated in the table. This corresponds to azimuthal angles of 0, 30, 60, ... , 330, 360 degrees for the first case, and 0, 20, 40, ..., 340 and 360 degrees for the second case. Periodicity was not established in Allen's result until the second revolution. The computed result is thus shifted by 360°. Additionally, 90° is added because of the difference in the rotor orientation. Therefore the comparison starts at $\psi = 450°$ onwards.

The comparison of the first three cases can be thought of as a mesh refinement study, although this should be done by doubling the number of mesh points in all directions, rather than increasing the number of points by small numbers as it is shown here. All three cases over-predict the lift coefficient except around the azimuthal angle greater than 90° and less than 225° approximately. This is not unexpected since the blade geometry from the Caradonna & Tung experiment was not fully specified such as where the root of the blade actually starts (only the diameter of the rotor and the aspect ratio are given). Different researchers presumably use slightly different geometries in this regard. The calculation with 18 time instances shows better agreement of the lift coefficient on the retreating side for both dissipation schemes, but the over-prediction of the lift coefficient between azimuthal angles of 0° and 30° is greater than the calculations with 12 time instances.

Allen explained that there was a dip in the coefficient of lift, C_L, around an azimuth angle approximately between 0° and 30° because the blade was running into the vortex generated from the previous blade. In the present work, it is not very visible that there is a dip in the lift coefficient in this area with the result from the JST scheme. This phenomenon is more visible with the CUSP dissipation scheme.

Case	Number of Cells			Number of Time Instances
	x	y	z	N
1	128	48	32	12
2	160	48	48	12
3	192	64	48	12
4	160	48	48	18

Table 5.2: Lifting forward flight test conditions.

It can be observed that as the number of mesh size increases, this feature starts to look more prominent. A calculation with the JST dissipation scheme combined with Vorticity Confinement will be discussed in chapter 6. Figures 5.14 and 5.15 show the distribution of the coefficient of pressure at $r/R = 0.90$ at 12 azimuthal angles from calculations with the JST and CUSP dissipation schemes. This corresponds to case 3 in the table. The calculations used $192 \times 64 \times 48$ mesh cells. The span $r/R = 0.90$ is chosen for comparison because discontinuity is certain to appear in the advancing side near the tip. A good agreement with the data provided by Allen is observed except at three azimuthal angles, 150°, 180° and 330°. Personal consultation with Professor Allen suggested that the number of mesh points is not enough to capture shock at the first two locations. The coefficient of pressure distribution at 330° over-predicts the result of Allen's by some margin. However, this location is on the retreating side and there is no physical reason why the coefficient of pressure should significantly drop only to rise up again at 360°. Plots of cases 1 and 2 for both the JST and CUSP dissipation schemes can be found in Appendix C.

5.8 Closing Remarks

The accuracy of the Time Spectral method has been verified for a number of forward flight cases, both lifting and nonlifting. The calculations for nonlifting rotors in forward flight show good agreement in all the cases. For the case of lifting rotors in forward flight, the coefficient of lift per blade at different locations for a complete revolution is in fairly good agreement with the data provided by Professor Allen although there is some discrepancy in the overall magnitude. The trend of the results

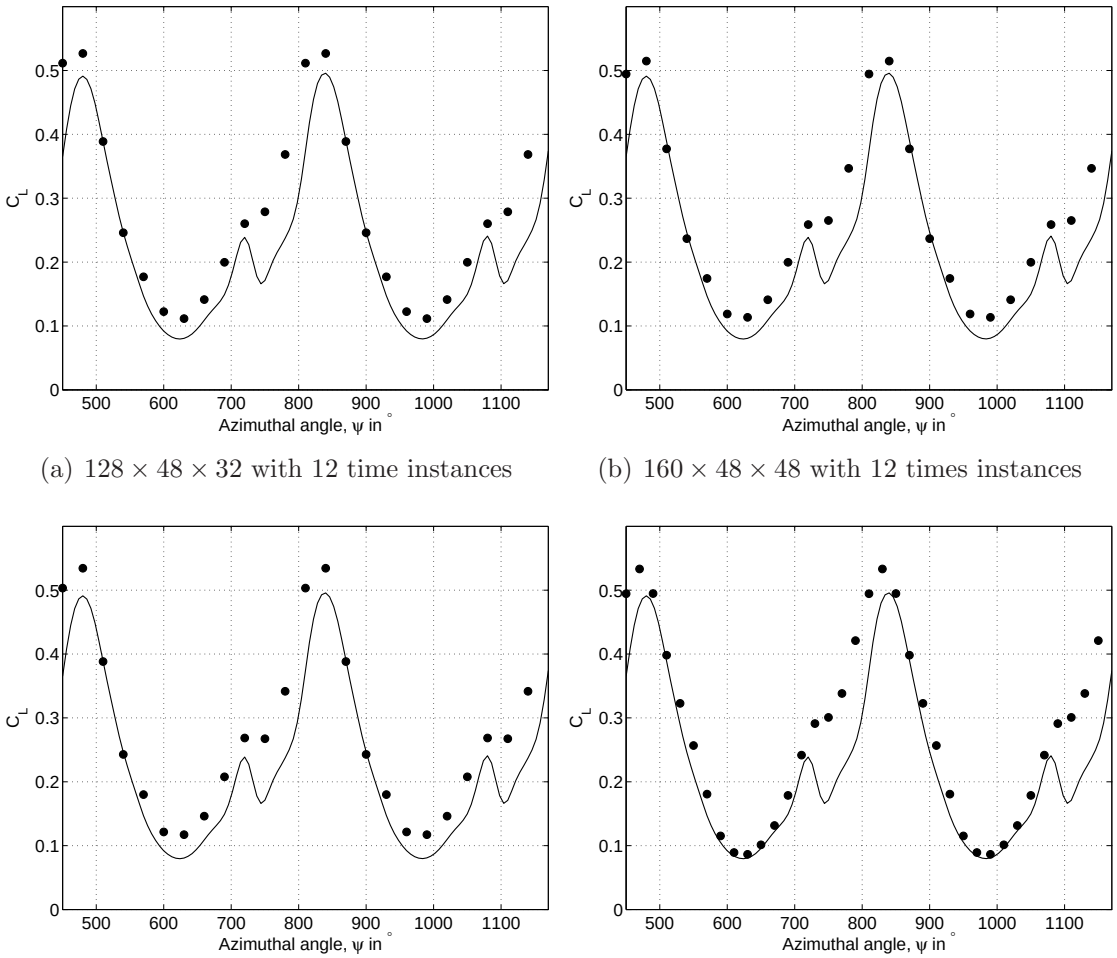

(a) $128 \times 48 \times 32$ with 12 time instances

(b) $160 \times 48 \times 48$ with 12 times instances

(c) $192 \times 64 \times 48$ with 12 time instances

(d) $160 \times 48 \times 48$ with 18 time instances

Figure 5.12: Comparison of the coefficient of lift per blade vs. the azimuth of a lifting rotor in forward flight from Euler calculation with the CUSP dissipation scheme, $M_t = 0.7$, $\mu = 0.2857$, $\theta_c = 8°$: • computed result from the current work using the JST dissipation scheme, — simulation result provided by Allen.

are the same but the blade–vortex interaction at the beginning of the advancing side is not present in the calculations with the JST scheme. The results with the CUSP scheme show better agreement. Lastly, the coefficient of pressure computed with the JST scheme using $192 \times 64 \times 48$ mesh cells are compared. The overall agreement is good except at three locations where there are some discrepancies. Most likely, these can be resolved with the increase in the number of mesh cells in the y direction.

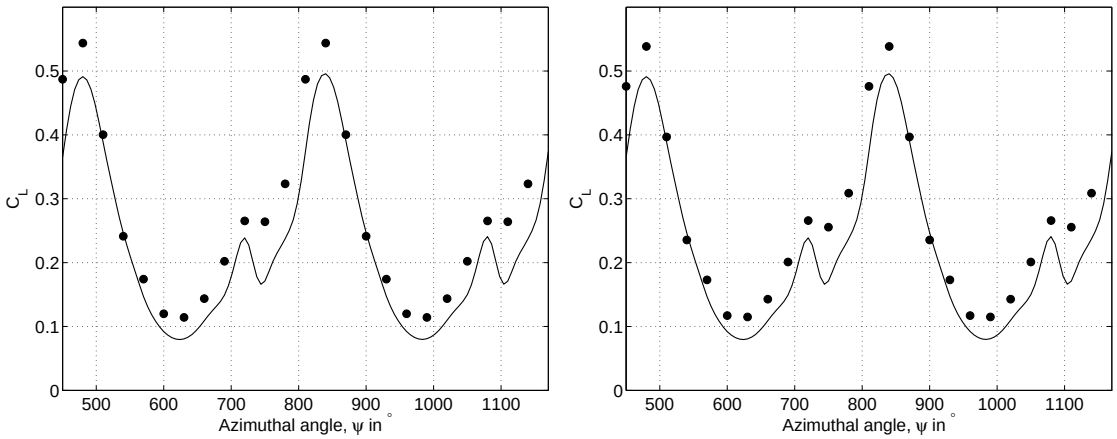

(a) $128 \times 48 \times 32$ with 12 time instances

(b) $160 \times 48 \times 48$ with 12 times instances

(c) $192 \times 64 \times 48$ with 12 times instances

(d) $160 \times 48 \times 48$ with 18 time instances

Figure 5.13: Comparison of the coefficient of lift per blade vs. the azimuth of a lifting rotor in forward flight from Euler calculation with the CUSP dissipation scheme, $M_t = 0.7$, $\mu = 0.2857$, $\theta_c = 8°$: • computed result from the current work using the CUSP dissipation scheme, — simulation result provided by Allen.

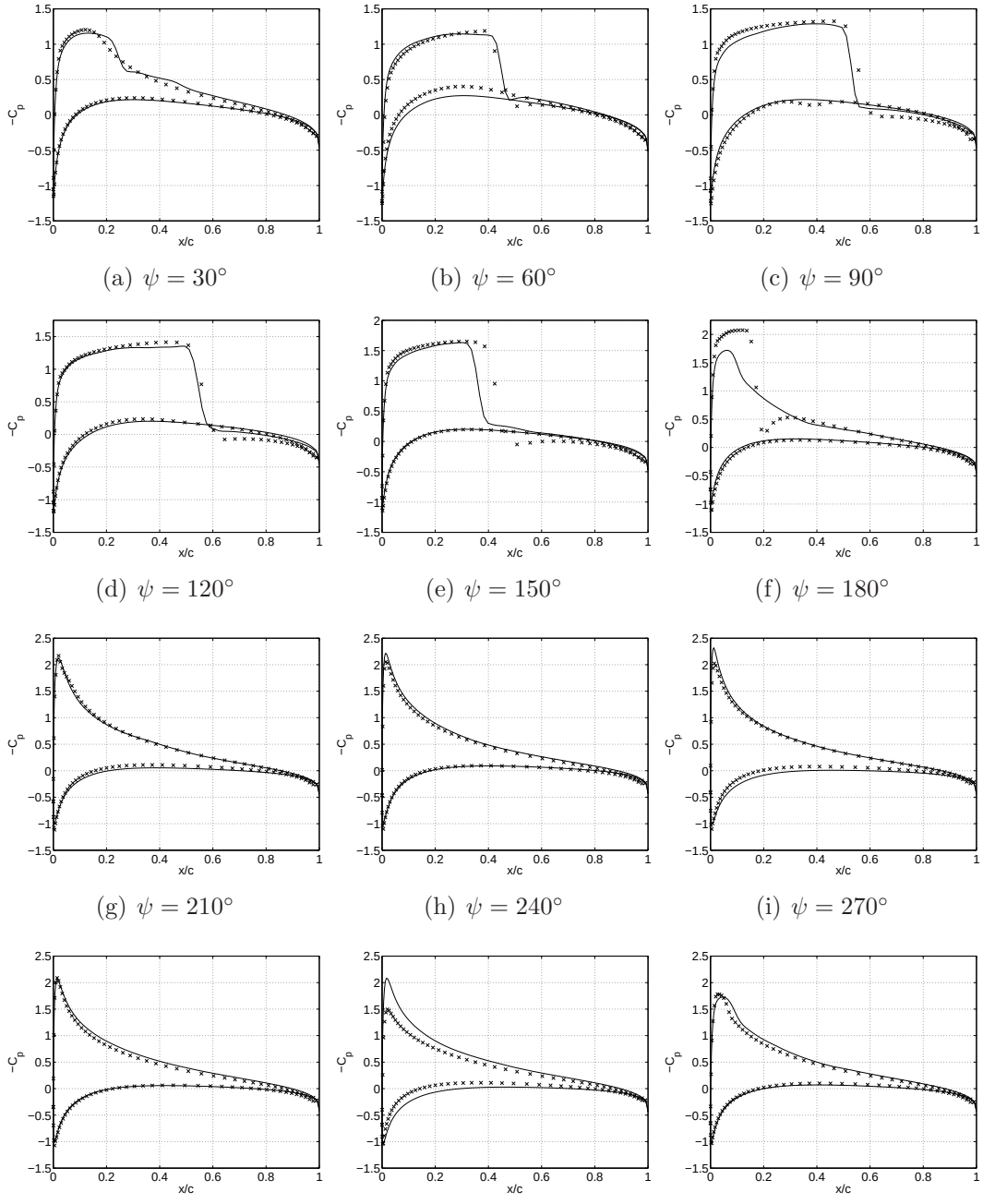

(a) $\psi = 30°$ (b) $\psi = 60°$ (c) $\psi = 90°$

(d) $\psi = 120°$ (e) $\psi = 150°$ (f) $\psi = 180°$

(g) $\psi = 210°$ (h) $\psi = 240°$ (i) $\psi = 270°$

(j) $\psi = 300°$ (k) $\psi = 330°$ (l) $\psi = 360°$

Figure 5.14: Coefficient of pressure at $r/R = 0.90$ using the JST dissipation scheme with $192 \times 64 \times 48$ mesh cells, $M_t = 0.7$, $\mu = 0.2857$, $\theta_c = 8°$, $N = 12$: — computed result, $\times$ result provided by Allen.

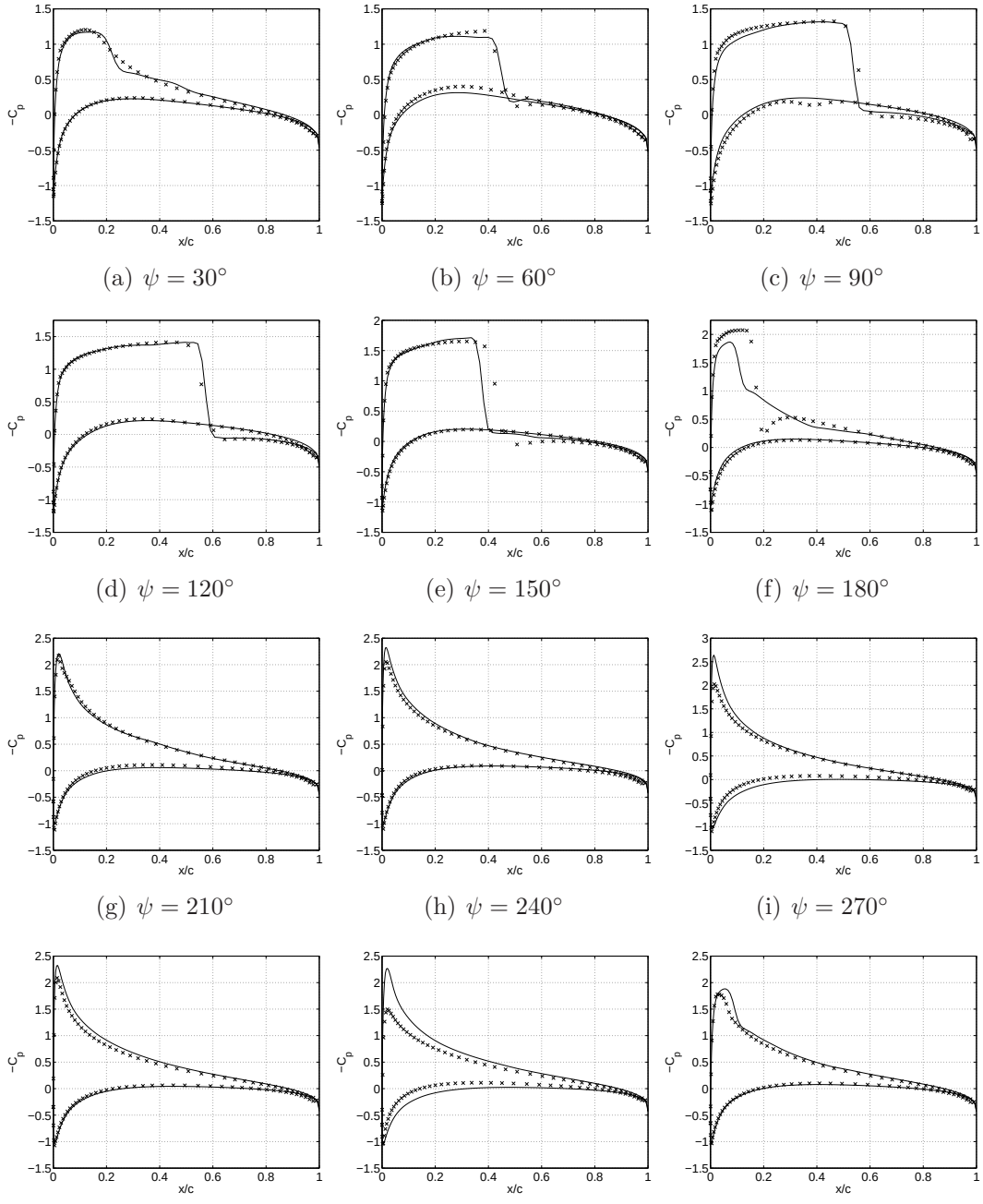

(a) $\psi = 30°$ (b) $\psi = 60°$ (c) $\psi = 90°$

(d) $\psi = 120°$ (e) $\psi = 150°$ (f) $\psi = 180°$

(g) $\psi = 210°$ (h) $\psi = 240°$ (i) $\psi = 270°$

(j) $\psi = 300°$ (k) $\psi = 330°$ (l) $\psi = 360°$

Figure 5.15: Coefficient of pressure at $r/R = 0.90$ using the CUSP dissipation scheme with $192 \times 64 \times 48$ mesh cells, $M_t = 0.7$, $\mu = 0.2857$, $\theta_c = 8°$, $N = 12$: — computed result, $\times$ result provided by Allen.

Chapter 6

Dynamic Vorticity Confinement for Compressible Flow

To understand why vorticity is such an important feature in three dimensions (Roe, 2001), it is useful to examine the vorticity transport equation:

$$\frac{\partial \boldsymbol{\omega}}{\partial t} + \mathbf{u} \cdot \nabla \boldsymbol{\omega} = \boldsymbol{\omega} \cdot \nabla \mathbf{u} + \frac{1}{\rho^2} \nabla \rho \times \nabla p + \nu \nabla^2 \boldsymbol{\omega}$$

where $\boldsymbol{\omega} = \vec{\nabla} \times \mathbf{u}$.

The first term on the right hand side is responsible for the stretching effect; it is driven by the changes in velocity in the direction of the vortex lines. The is the term that is responsible for the evolution of the small scale structures.

The second term on the right hand side of the equation is the barotropic term, which arises from the misalignment of the pressure and density gradients. Where there is a density gradient and a pressure gradient is applied, the force that the pressure gradient creates may not pass through the center of gravity and thus cause the fluid element to spin.

The last term on the right hand side shows that vorticity is diffused by the viscosity. In turn, viscosity also creates vorticity at the surfaces. Numerical viscosity introduced by the discretization scheme has a similar effect. This issue is usually addressed by placing a large number of grid points close to the surfaces. However,

once the vorticity leaves the neighborhood near the surface, the vorticity cannot be accurately predicted unless one is willing to enlarge the area of refined mesh. This is not a practical approach, especially at Reynolds numbers of aeronautical interest, as it will be too computationally expensive.

Vorticity Confinement is an interesting technique that potentially can be very useful to rotorcraft flow simulations. It has the ability to control vortex diffusion that occurs too quickly from numerical dissipation that is inherently built-in to the numerical schemes when the mesh spacing is not fine enough. The method remains somewhat controversial and has not gained universal acceptance in the CFD community. Therefore Vorticity Confinement is only presented in this chapter as an optional modification of the simulation method.

6.1 Background of Vorticity Confinement

As mentioned in section 1.2.1, Steinhoff & Underhill (1994); Steinhoff (1994) first introduced the concept of Vorticity Confinement stemming from the concept of artificial compression for shocks and contact discontinuities of Harten (1978). The method has been continually refined and tested during the past decade for configurations such as vortex–solid body interaction (Wang *et al.*, 1995), flow over a cylinder and flow over a block in a channel (Wenren *et al.*, 2001), flow over an automobile (Dietz *et al.*, 2001), three-dimensional cylinder, circle and half-circle (Fan & Steinhoff, 2004). Recently, Wenren *et al.* (2006) implemented Vorticity Confinement into a flow solver to compute rotorcraft brownout using a uniform Cartesian grid. However, the main purpose of their work seemed to be to achieve good visualization of the ground effects, rather than to accurately compute the aerodynamics of rotorcraft. Particulates were also tracked during the time evolution.

The method has been shown to work on unstructured meshes solving incompressible flows. Murayama *et al.* (2001) computed RANS calculations with adaptive grid refinement for a double delta wing and a low aspect ratio NACA 0012 wing. Results for the NACA 0012 wing with a relative large confinement parameter showed extra vortices that were nonphysical embedded in the solution. Löhner & Yang (2002);

Löhner *et al.* (2002) performed Euler calculations on a low aspect ratio NACA 0012 wing, and also laminar Navier–Stokes calculations on a two-dimensional cylinder and a three-dimensional delta wing. It was shown that Vorticity Confinement was capable of tracking vortices over large distances. More importantly however, Löhner & Yang; Löhner *et al.* introduced a new form for the constant ϵ that is present in the confinement term. This constant is now a true constant, rather than having the dimension of a velocity as first conceived by Steinhoff & Underhill (1994); Steinhoff (1994). This will be discussed in detail in section 6.3.1.

For compressible flow, Dadone A. & Grossman (2001); Hu & Grossman (2002); Hu *et al.* (2002) introduced a new formulation by including a body force term in the energy equation. Morvant *et al.* (2005) obtained good results for airfoil–vortex interaction computations. A new formulation of compressible Vorticity Confinement will be presented later in section 6.3.

6.2 Vorticity Confinement for Incompressible Flow

For general unsteady incompressible flows, the governing equations with the Vorticity Confinement term are:

$$\nabla \cdot \mathbf{u} = 0 \tag{6.1}$$

$$\frac{\partial \mathbf{u}}{\partial t} + (\mathbf{u} \cdot \nabla)\,\mathbf{u} = -\frac{1}{\rho}\nabla p + \mu \nabla^2 \mathbf{u} - \epsilon \mathbf{s}. \tag{6.2}$$

where $\mathbf{s}$ is the confinement term and its simplest form is

$$\mathbf{s} = \hat{\mathbf{n}} \times \boldsymbol{\omega}.$$

and

$$\hat{\mathbf{n}} = \frac{\boldsymbol{\eta}}{|\boldsymbol{\eta}|}. \tag{6.3}$$

The vorticity vector $\boldsymbol{\omega}$ is given by

$$\boldsymbol{\omega} = \vec{\nabla} \times \mathbf{u}.$$

The variable $\boldsymbol{\eta}$ is defined as:

$$\boldsymbol{\eta} = \nabla |\boldsymbol{\omega}| . \tag{6.4}$$

The idea behind this formulation is that vorticity is convected in the direction determined by the gradient of the vorticity. The unit vector $\hat{\mathbf{n}}$ points in the direction of the gradient of the vorticity magnitude and the confinement term, $\mathbf{s}$, convects the vorticity back towards the centroid.

A very important feature of the Vorticity Confinement method is that the effect of the confinement term is limited to the vortical regions of the flow field, as the term vanishes outside these regions. Additionally, it is shown in the papers by Steinhoff & Underhill (1994); Steinhoff (1994) that the mass and vorticity are conserved and the momentum is almost exactly conserved.

6.3 Vorticity Confinement for Compressible Flow

The big disadvantage of the Vorticity Confinement method proposed by Steinhoff & Underhill; Steinhoff is that it is formulated for incompressible flow, both the original formulation and the new one (not discussed here). Since the flow of the helicopter rotor in hover and forward flight almost always involves transonic flow near the blade tip in the hover case and on the advancing side of the forward flight case, one needs a formulation of Vorticity Confinement suitable for compressible flow simulations. Dadone A. & Grossman (2001); Hu & Grossman (2002); Hu *et al.* (2002) proposed a new formulation of Vorticity Confinement for compressible flow by introducing the body force per unit mass term to the governing equations. For the momentum equations, the formulation of the confinement terms are based on that of the original one. Using the same notation as in (3.1), the governing equations now take the form:

$$\int_{\Omega} \frac{\partial \boldsymbol{w}}{\partial t} \, \mathrm{d}\mathcal{V} + \oint_{\partial\Omega} \mathbf{f}_j \cdot \mathbf{n} \, \mathrm{d}\mathcal{S} = - \int_{\Omega} \epsilon \mathbf{s} \, \mathrm{d}\mathcal{V}.$$

The components of $\mathbf{s}$ are

$$\mathbf{s} = \begin{bmatrix} 0 \\ \rho\left(\hat{\mathbf{n}} \times \boldsymbol{\omega}\right) \cdot \mathbf{i} \\ \rho\left(\hat{\mathbf{n}} \times \boldsymbol{\omega}\right) \cdot \mathbf{j} \\ \rho\left(\hat{\mathbf{n}} \times \boldsymbol{\omega}\right) \cdot \mathbf{k} \\ \rho\left(\hat{\mathbf{n}} \times \boldsymbol{\omega}\right) \cdot \mathbf{u} \end{bmatrix}, \tag{6.5}$$

and in three dimensions:

$$\mathbf{s} = \begin{bmatrix} 0 \\ \rho\left(n_2\omega_3 - n_3\omega_2\right) \\ \rho\left(n_3\omega_1 - n_1\omega_3\right) \\ \rho\left(n_1\omega_2 - n_2\omega_1\right) \\ \rho\left\{\left(n_2\omega_3 - n_3\omega_2\right)u_1 + \left(n_3\omega_1 - n_1\omega_3\right)u_2 + \left(n_1\omega_2 - n_2\omega_1\right)u_3\right\} \end{bmatrix}. \tag{6.6}$$

Dietz (2004) applied this method to simulate an unpowered missile and obtained good results for the pitching moment and normal force on the missile compared to the experimental data. The wake flow calculations also showed that the combined method was capable to capture the wake structures without resorting to fine meshes.

6.3.1 Dimensional Analysis of ϵ

One of the problems in applying Vorticity Confinement is the inconsistency of the parameter ϵ. As mentioned in section 6.1, ϵ has the dimension of a velocity. Fedkiw *et al.* (2001) included a linearly dependent parameter ϵ according to the mesh size h, so now the confining term becomes:

$$\epsilon = \epsilon_h \cdot h.$$

In this case, ϵ is still not dimensionless but at least it now scales with the mesh size.

Löhner & Yang (2002); Löhner *et al.* (2002) performed dimensional analysis and further refined the definition of the parameter ϵ to include the length scale h as the

characteristic length in the direction of $\nabla |\omega|$, i.e.

$$h = \mathbf{h} \cdot \frac{\nabla |\boldsymbol{\omega}|}{|\nabla |\boldsymbol{\omega}||}. \tag{6.7}$$

Furthermore, Löhner & Yang (2002); Löhner *et al.* (2002) suggested that the application of Vorticity Confinement in the boundary layer region where there are sufficient mesh points could lead to numerical instabilities. Therefore an explicit switch was devised based on the local Reynolds number, Re_h. The final formula for the confinement term with a switch is:

$$\mathbf{s} = g\left(\mathrm{Re}_{\boldsymbol{\omega},h}\right) \rho h^2 \nabla |\boldsymbol{\omega}| \times \boldsymbol{\omega} \tag{6.8}$$

where

$$g = \max\left\{0, \min\left[1, \frac{\mathrm{Re}_{\boldsymbol{\omega},h} - \mathrm{Re}^0_{\boldsymbol{\omega},h}}{\mathrm{Re}^1_{\boldsymbol{\omega},h} - \mathrm{Re}^0_{\boldsymbol{\omega},h}}\right]\right\} \tag{6.9}$$

and

$$\mathrm{Re}_{\boldsymbol{\omega},h} = \frac{\rho |\nabla |\boldsymbol{\omega}||}{\mu}. \tag{6.10}$$

The works by Fedkiw *et al.*; Löhner & Yang; Löhner *et al.* are for incompressible Navier–Stokes equations. Additionally, in the work of Löhner & Yang; Löhner *et al.*, the method is implemented on unstructured meshes (note that the variable ρ is present in (6.8) because ρ is not divided through the momentum equations as in (6.2)).

Robinson (2004) carried out further dimensional analysis of ϵ for compressible flow. However his formulation differs to the work of Dadone A. & Grossman; Hu *et al.*; Hu & Grossman in that it does not include the body force term in the energy equation. If one examines (6.5) for the momentum terms in full form using (6.3) and (6.4), then factoring out $|\boldsymbol{\omega}|$,

$$\mathbf{s} = \rho |\boldsymbol{\omega}| \left\{ \frac{\nabla |\boldsymbol{\omega}|}{|\nabla |\boldsymbol{\omega}||} \times \frac{\boldsymbol{\omega}}{|\boldsymbol{\omega}|} \right\}. \tag{6.11}$$

The term outside the parentheses is the magnitude term, and the term inside the parentheses is the directional term. Substituting

$$\epsilon_c = \epsilon \left| \mathbf{u} \right|,$$

where $\mathbf{u}$ is the velocity vector, into (6.11) produces

$$\epsilon_c \mathbf{s} = \epsilon \rho \left| \mathbf{u} \right| \left| \boldsymbol{\omega} \right| \left\{ \frac{\nabla \left| \boldsymbol{\omega} \right|}{\left| \nabla \left| \boldsymbol{\omega} \right| \right|} \times \frac{\boldsymbol{\omega}}{\left| \boldsymbol{\omega} \right|} \right\}. \tag{6.12}$$

The unit of $\left| \mathbf{u} \right| \left| \boldsymbol{\omega} \right|$ has the dimension of a helicity. Therefore, Robinson rearranges the terms to make the confinement term directly proportional to the helicity:

$$\epsilon_f \mathbf{s} = \epsilon \rho \left| \mathbf{u} \cdot \boldsymbol{\omega} \right| \left\{ \frac{\nabla \left| \boldsymbol{\omega} \right|}{\left| \nabla \left| \boldsymbol{\omega} \right| \right|} \times \frac{\boldsymbol{\omega}}{\left| \boldsymbol{\omega} \right|} \right\} \tag{6.13}$$

where ϵ_f is a true dimensionless parameter. Robinson performed test cases on various types of missiles. The missile force and moment were shown to improve using the formulation (6.13).

6.4 Dynamic Vorticity Confinement

Although the formulation provided by Robinson is an improvement over the previous works in some ways, it still fails to take into account the length scale in the flow field as Löhner & Yang; Löhner *et al.* have. Ultimately, one needs to construct a dynamic Vorticity Confinement term for fully compressible flow.

One could begin with the governing equations, the Navier–Stokes equations, and start looking at a way in which this vortex compression mechanism can be added as an anti-diffusion term. The properties needed to make this mechanism work are

(1) The anti-diffusion term should vanish as the mesh size gets smaller, i.e. $\epsilon \propto \Delta$.

(2) It should vary its strength according to the gradient of the vortex, $\nabla \left| \omega \right|$, i.e. $\epsilon \propto \nabla \left| \omega \right|$.

For finite volume, structured meshes, one of the simplest approaches is to scale the constant ϵ according to the cube root of the ratio of the local cell volume to the average cell volume in the computational domain:

$$\epsilon_v \propto \epsilon \left(\frac{\mathcal{V}}{\mathcal{V}_{\text{average}}} \right)^{1/3}.$$

Then ϵ_v varies with the length scale of the mesh cells. This simple algebraic relation satisfies the first criterion but not the second. However, if one simply uses ϵ_v in (6.12), both criteria are satisfied. The resulting components in the confinement term for compressible flow with the body force term in the energy equation are now:

$$\mathbf{s} = |\mathbf{u}| \left(\frac{\mathcal{V}}{\mathcal{V}_{\text{averaged}}} \right)^{1/3} . \begin{bmatrix} 0 \\ \rho \left(\hat{\mathbf{n}} \times \boldsymbol{\omega} \right) \cdot \mathbf{i} \\ \rho \left(\hat{\mathbf{n}} \times \boldsymbol{\omega} \right) \cdot \mathbf{j} \\ \rho \left(\hat{\mathbf{n}} \times \boldsymbol{\omega} \right) \cdot \mathbf{k} \\ \rho \left(\hat{\mathbf{n}} \times \boldsymbol{\omega} \right) \cdot \mathbf{u} \end{bmatrix} \tag{6.14}$$

where $\mathbf{u}$ is the local velocity vector and the confinement parameter is now dimensionless.

Alternatively, using the helicity directly as in (6.13), the confinement term is

$$\mathbf{s} = |\mathbf{u} \cdot \boldsymbol{\omega}| \left(\frac{\mathcal{V}}{\mathcal{V}_{\text{averaged}}} \right)^{1/3} . \begin{bmatrix} 0 \\ \rho \left(\hat{\mathbf{n}} \times \frac{\boldsymbol{\omega}}{|\boldsymbol{\omega}|} \right) \cdot \mathbf{i} \\ \rho \left(\hat{\mathbf{n}} \times \frac{\boldsymbol{\omega}}{|\boldsymbol{\omega}|} \right) \cdot \mathbf{j} \\ \rho \left(\hat{\mathbf{n}} \times \frac{\boldsymbol{\omega}}{|\boldsymbol{\omega}|} \right) \cdot \mathbf{k} \\ \rho \left(\hat{\mathbf{n}} \times \frac{\boldsymbol{\omega}}{|\boldsymbol{\omega}|} \right) \cdot \mathbf{u} \end{bmatrix} . \tag{6.15}$$

The application of this last formulation depends on the type of flow. If the helical structure is normal to the free-stream velocity (e.g. the vortical structure of a tornado is normal to the direction of its velocity), then the confinement term will become

ineffective because $|\mathbf{u}\cdot\boldsymbol{\omega}|$ will reduce to zero.

In finite volume calculations, especially in RANS calculations, the difference between the smallest and largest cell volumes is very large, and thus the ratio between $\mathcal{V}$ and $\mathcal{V}_{\text{average}}$ in most regions in the domain essentially becomes zero. In the case of this NACA wing presented in the next section, the smallest cell volume in the domain is in the order of $\mathcal{O}(10^{-6})$ while the largest cell volume in the domain is in the order of $\mathcal{O}(10^{2})$. In order to apply the length scale more appropriately, one can use the log scale for the scaling parameter. Equations (6.14) and (6.15) can be now be scaled as follows

$$\mathbf{s} = |\mathbf{u}| \left[1 + \log_{10}\left(1 + \frac{\mathcal{V}}{\mathcal{V}_{\text{averaged}}}\right)^{1/3}\right] \begin{bmatrix} 0 \\ \rho\left(\hat{\mathbf{n}}\times\boldsymbol{\omega}\right)\cdot\mathbf{i} \\ \rho\left(\hat{\mathbf{n}}\times\boldsymbol{\omega}\right)\cdot\mathbf{j} \\ \rho\left(\hat{\mathbf{n}}\times\boldsymbol{\omega}\right)\cdot\mathbf{k} \\ \rho\left(\hat{\mathbf{n}}\times\boldsymbol{\omega}\right)\cdot\mathbf{u} \end{bmatrix} \tag{6.16}$$

and

$$\mathbf{s} = |\mathbf{u}\cdot\boldsymbol{\omega}| \left[1 + \log_{10}\left(1 + \frac{\mathcal{V}}{\mathcal{V}_{\text{averaged}}}\right)^{1/3}\right] \begin{bmatrix} 0 \\ \rho\left(\hat{\mathbf{n}}\times\frac{\boldsymbol{\omega}}{|\boldsymbol{\omega}|}\right)\cdot\mathbf{i} \\ \rho\left(\hat{\mathbf{n}}\times\frac{\boldsymbol{\omega}}{|\boldsymbol{\omega}|}\right)\cdot\mathbf{j} \\ \rho\left(\hat{\mathbf{n}}\times\frac{\boldsymbol{\omega}}{|\boldsymbol{\omega}|}\right)\cdot\mathbf{k} \\ \rho\left(\hat{\mathbf{n}}\times\frac{\boldsymbol{\omega}}{|\boldsymbol{\omega}|}\right)\cdot\mathbf{u} \end{bmatrix}. \tag{6.17}$$

Equation (6.17) is the formulation adopted in the present work.

6.5 Calculations with Vorticity Confinement

The first case is a computation of wing tip vortex of an NACA 0012 wing with an aspect ratio of 3. The free-stream Mach number is 0.8 and the angle of attack is 5 degrees. The fully compressible Euler calculations were solved with Vorticity Confinement using the formulation from (6.17) for four values of the confinement parameter ϵ.

The mesh was generated internally and is a typical C-mesh with $160 \times 32 \times 48$ mesh cells. There are 3 cut-planes normal to the x direction at $x = 2, 4, 6$ and 8 (the reference chord length of unity and the trailing edge is located at $x = 1$). The coefficient ϵ is fixed at 0, 0.025, 0.05 and 0.075. The results are shown in figure 6.1. One can observe that the vortex structure is still quite well maintained after 8 chord lengths away with the Vorticity Confinement term. The effectiveness depends on the strength of the confinement term. For the case of no confinement, $\epsilon = 0$, the vorticity magnitude dissipates much quicker.

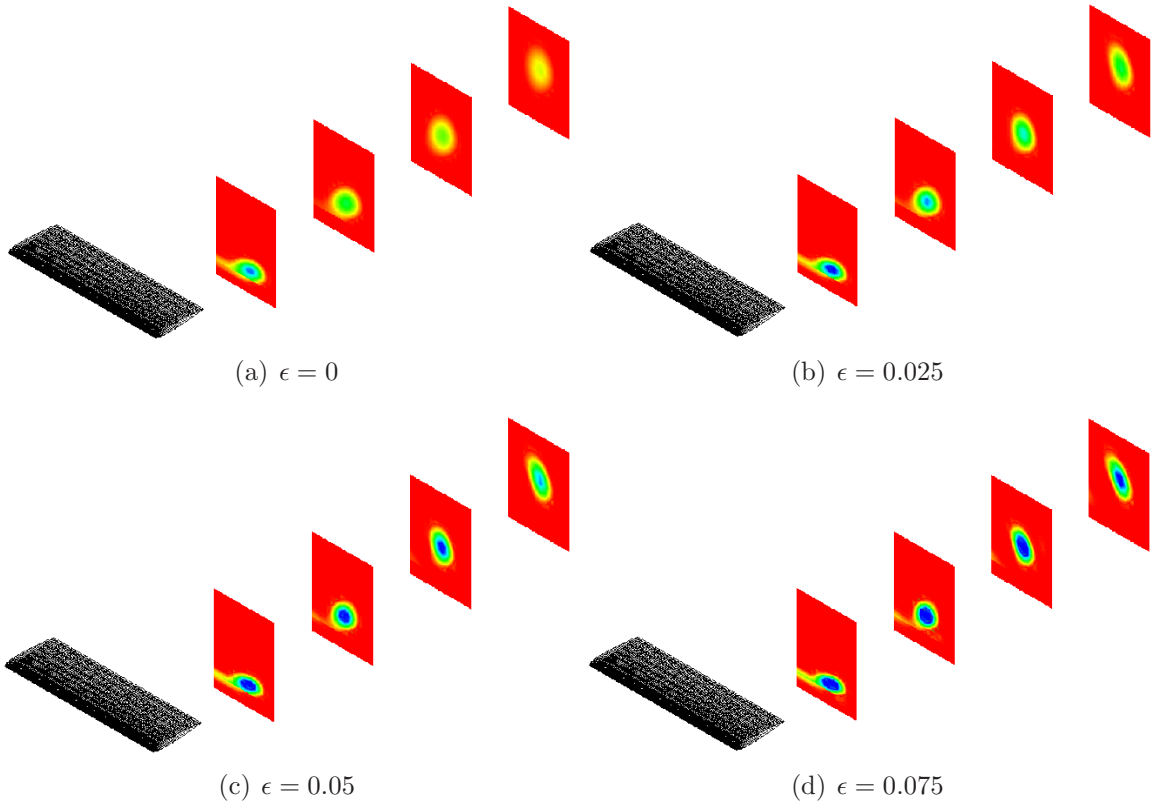

(a) $\epsilon = 0$ (b) $\epsilon = 0.025$

(c) $\epsilon = 0.05$ (d) $\epsilon = 0.075$

Figure 6.1: Vorticity magnitude on an NACA 0012 wing with four values of ϵ: $M_\infty = 0.8$, $\alpha = 5°$, aspect ratio = 3.

Figure 6.3 shows the distribution of the coefficient of pressure on the wing at three different span stations. The effect of adding the confinement term is negligible and the distribution of the coefficient of pressure for each value of ϵ collapses into one line. The coefficients of lift and drag at three different span stations are listed in

	$z = 0.891$		$z = 1.828$		$z = 2.766$	
ϵ	c_l	c_d	c_l	c_d	c_l	c_d
0	0.7098	0.0792	0.6123	0.0651	0.3869	0.0394
0.025	0.7091	0.0791	0.6114	0.0650	0.3851	0.0393
0.050	0.7083	0.0790	0.6103	0.0649	0.3833	0.0391
0.075	0.7074	0.0788	0.6093	0.0647	0.3817	0.0389

Table 6.1: Coefficients of lift and drag from Euler calculations of NACA 0012 wing with four values of ϵ at three span stations: $M_\infty = 0.8$, $\alpha = 5°$, aspect ratio = 3.

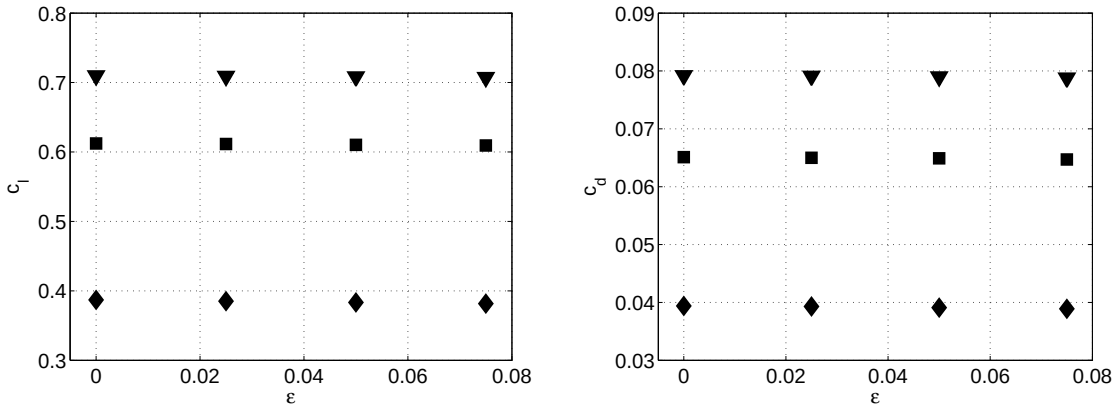

(a) Section C_L (b) Section C_D

Figure 6.2: Coefficients of lift and drag at three span stations from Euler calculation of an NACA 0012 wing for four values of ϵ: ▼ the span station $z = 0.891$, ■ the span station $z = 1.828$, ♦ the span station $z = 2.766$, $M_\infty = 0.8$, $\alpha = 5°$, aspect ratio = 3.

table 6.1, and are plotted separately in figure 6.2. The coefficients of lift and drag decreases by approximately 0.3% and 0.5% respectively as the confinement parameter ϵ increased from zero to 0.075 at $z = 0.891$, and up to 1.3% for both coefficients at $z = 2.766$. The location $z = 2.766$ was very close to the tip of the wing ($z_{\text{tip}} = 3$), and this was where the tip vortex was generated. Therefore the difference in both c_l and c_d for different values of the confinement parameter is expected to be largest at this location. The results from this test case indicate that the new formulation works well for transonic flow calculations and that the inclusion of the confinement term does not diminish the ability of the flow solver to capture discontinuities.

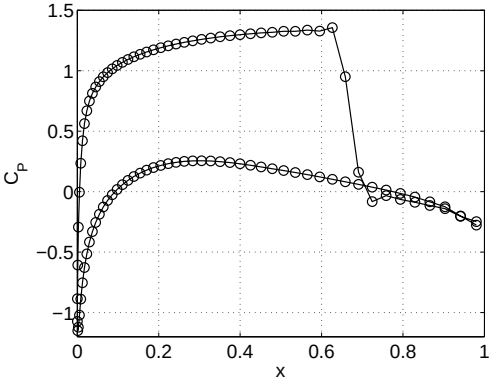

(a) Span station $z = 0.891$

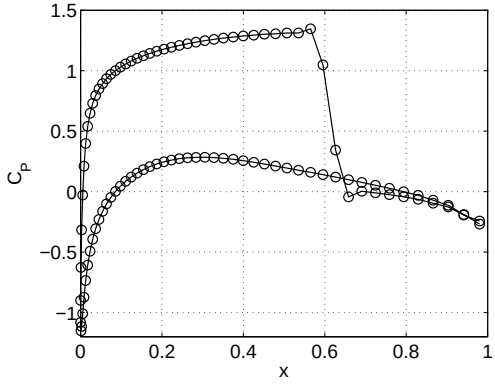

(b) Span station $z = 1.828$

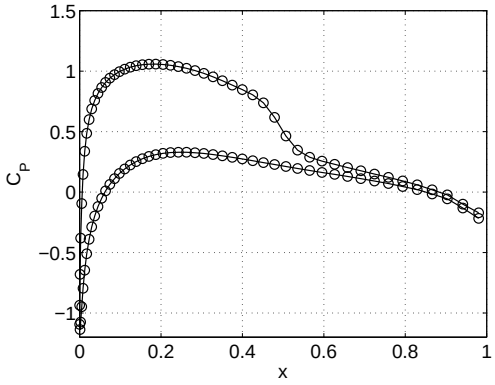

(c) Span station $z = 2.766$

Figure 6.3: Coefficient of pressure distribution at four span stations on NACA 0012 wing for four values of ϵ: — ∘ — denotes $\epsilon = 0$, $\cdots$ denotes $\epsilon = 0.025$, – · – denotes $\epsilon = 0.05$, – – denotes $\epsilon = 0.075$, $M_\infty = 0.8$, $\alpha = 5$, aspect ratio = 3.

6.6 Vorticity Confinement in Rotorcraft Flow

This section discusses the application of Vorticity Confinement to rotorcraft simulation. A comparison is made with the data for a lifting rotor in forward flight supplied by Professor Allen. The geometry for this case is from Caradonna & Tung (1981) with a collective pitch of 8 degrees. The tip Mach number is 0.7 and the advance ratio is $\mu = 0.2857$. The computation used 12 time instances for Euler calculation with $160 \times 48 \times 48$ mesh cells. The formulation of Vorticity Confinement is from (6.17). Figure 6.4 shows a significant improvement over the results previously shown in figure

5.12. The over-prediction of the lift coefficient has decreased markedly, especially on the advancing side. As ϵ increases, one can easily observe the effects of the blade–vortex interaction at the beginning of the advancing side. Recall that the results from the JST scheme hardly exhibit the dip in the coefficient of lift, even at the largest mesh size of $192 \times 64 \times 48$. The results shown here used fewer mesh cells but the effect of the blade–vortex interaction can be seen clearly when the confinement parameter ϵ is sufficiently large.

The required value of the confinement parameter for this case is one order of magnitude larger than the fixed-wing case. This is because the skewed geometry of the helicopter mesh. Additionally, because the mesh cells are extremely small near the hub, confinement is only added in the outer half of the blade. The smallest mesh size for this case is of the order $\mathcal{O}(10^{-8})$ while the largest mesh cell is of the order of $\mathcal{O}(10^{-1})$.

Figure 6.5 shows the vorticity magnitude at the first time instance where $\psi = 90°$ at 2 cut-planes normal to the x direction where $x = 2$ and $x = 5$. The leading edge and the trailing edge are located at $x = 0$ and $x = 1$ respectively. It can be observed from the plots that the vortical structure could be maintained better with Vorticity Confinement compared to the result from the original calculation. However, the vortex structure still diffuses much faster compared to the results of the fixed-wing because the mesh distribution in the vortical regions is more sparse than the traditional C-mesh distribution. It is safe to assume that changing the current O–H mesh topology to an H–H mesh, or an unstructured mesh distribution should improve this matter significantly. The severity of the mesh stretching can be seen from figure 6.6.

6.7 Discussion and Analysis

The idea of Vorticity Confinement was first conceived by Steinhoff (1994); Steinhoff & Underhill (1994) to counteract numerical dissipation that is almost always employed in numerical schemes. In its simplest form, the confinement term $\mathbf{s}$ can be expressed

as

$$\mathbf{s} = \frac{\nabla |\boldsymbol{\omega}|}{|\nabla |\boldsymbol{\omega}||} \times \boldsymbol{\omega}.$$

Upon taking the curl of the confinement term in conjunction with the following mathematical identity

$$\vec{\nabla} \times (\mathbf{A} \times \mathbf{B}) = \mathbf{A} (\nabla \cdot \mathbf{B}) + (\mathbf{B} \cdot \nabla) \mathbf{A} - \mathbf{B} (\nabla \cdot \mathbf{A}) - (\mathbf{A} \cdot \nabla) \mathbf{B}$$

with

$$\mathbf{A} = \frac{\nabla |\boldsymbol{\omega}|}{|\nabla |\boldsymbol{\omega}||} \qquad \text{and} \qquad \mathbf{B} = \boldsymbol{\omega},$$

one obtains

$$\vec{\nabla} \times \mathbf{s} = \frac{\nabla |\boldsymbol{\omega}|}{|\nabla |\boldsymbol{\omega}||} (\nabla \cdot \boldsymbol{\omega}) + (\boldsymbol{\omega} \cdot \nabla) \frac{\nabla |\boldsymbol{\omega}|}{|\nabla |\boldsymbol{\omega}||} - \boldsymbol{\omega} \left(\nabla \cdot \frac{\nabla |\boldsymbol{\omega}|}{|\nabla |\boldsymbol{\omega}||} \right) - \left(\frac{\nabla |\boldsymbol{\omega}|}{|\nabla |\boldsymbol{\omega}||} \cdot \nabla \right) \boldsymbol{\omega}. \quad (6.18)$$

As before, let

$$\hat{\mathbf{n}} = \frac{\nabla |\boldsymbol{\omega}|}{|\nabla |\boldsymbol{\omega}||},$$

and recognizing that $\hat{\mathbf{n}}$ is a normal unit vector pointing in the direction of the gradient of vorticity magnitude, one can infer that this is the directional term. Equation (6.18) can now be rewritten as

$$\vec{\nabla} \times \mathbf{s} = \hat{\mathbf{n}} (\nabla \cdot \boldsymbol{\omega}) + (\boldsymbol{\omega} \cdot \nabla) \hat{\mathbf{n}} - \boldsymbol{\omega} (\nabla \cdot \hat{\mathbf{n}}) - (\hat{\mathbf{n}} \cdot \nabla) \boldsymbol{\omega}. \quad (6.19)$$

These are the terms that are subtracted from the vorticity transport equation in order to counteract the diffusion of vorticity. The terms on the right hand side can

be expanded as follows

$$(\hat{n}_1\mathbf{i} + \hat{n}_2\mathbf{j} + \hat{n}_3\mathbf{k})\left(\frac{\partial\omega_x}{\partial x} + \frac{\partial\omega_y}{\partial y} + \frac{\partial\omega_z}{\partial z}\right) \tag{6.20}$$

$$\left(\omega_x\frac{\partial}{\partial x} + \omega_y\frac{\partial}{\partial y} + \omega_z\frac{\partial}{\partial z}\right)(\hat{n}_1\mathbf{i} + \hat{n}_2\mathbf{j} + \hat{n}_3\mathbf{k}) \tag{6.21}$$

$$(\omega_x\mathbf{i} + \omega_y\mathbf{j} + \omega_z\mathbf{k})\left(\frac{\partial\hat{n}_1}{\partial x} + \frac{\partial\hat{n}_2}{\partial y} + \frac{\partial\hat{n}_3}{\partial z}\right) \tag{6.22}$$

$$\left(\hat{n}_1\frac{\partial}{\partial x} + \hat{n}_2\frac{\partial}{\partial y} + \hat{n}_3\frac{\partial}{\partial z}\right)(\omega_x\mathbf{i} + \omega_y\mathbf{j} + \omega_z\mathbf{k}) \tag{6.23}$$

The effects of adding and subtracting these terms from the vorticity transport equation are not clear with these mathematical expressions. This can be more easily understood when examining the momentum equations (6.2).

In two dimensions, the first two terms on the right hand side become zero. The last two terms can then be simplified to

$$\omega_z\mathbf{k}\left(\frac{\partial\hat{n}_1}{\partial x} + \frac{\partial\hat{n}_2}{\partial y}\right) \qquad \text{and} \qquad \left(\hat{n}_1\frac{\partial\omega_z}{\partial x} + \hat{n}_2\frac{\partial\omega_z}{\partial y}\right)\mathbf{k}.$$

The signs in front of these two terms are negative, which means that these two quantities are added to the vorticity transport equation to counteract the numerical dissipation.

6.7.1 Lamb–Oseen Vortex Model Problem

To visualize the effect of adding the curl of the confinement term to the vorticity transport equation, a model problem is examined. The model problem consists of the Lamb–Oseen vortex. The velocity in the θ direction is given by

$$v_\theta = \frac{\Gamma}{2\pi}\frac{1 - \exp\left(r/r_c\right)^2}{r}$$

where r is the radius, r_c is the core radius and Γ is circulation contained in the vortex. Figure 6.7 shows the initial vorticity of the model problem, and the initial vorticity along the radial direction is shown in figure 6.8. Calculation was performed on a square domain with 15×15 uniformly distributed grid points.

Upon numerically calculating the curl of the confinement term, the result is presented in figure 6.9. These are the values added to the vorticity transport equation and one can observe that the values are positive and concentrated near the center of the vortex. This shows that the confinement term does prevent the vorticity from diffusion. Similarly, outside a certain cut-off point along the radius, the values become negative. This mechanism, again, prevents the vortical structure from diffusing away as it has opposite signs to the diffusion terms. Note that the value at the origin is not plotted here because the gradient of the vorticity magnitude at this point is identically zero for this model problem. Hence $\hat{\mathbf{n}}$ is undefined at this location, and its value is omitted from this plot.

6.7.2 Numerical Diffusion vs. Vorticity Confinement

One issue that arises from the inception of Vorticity Confinement is that the confinement term is independent of the numerical schemes used in calculations. This leaves for inconsistencies when different numerical schemes are used, and is one of the major problems in correctly identifying the confinement parameter ϵ. Naturally, when one uses a high order scheme (higher than second order), numerical diffusion is considerably less in comparison to first or second order accurate schemes. As a result, there is a need to systematically formulate the confinement term based on numerical diffusion and discretization errors.

6.8 Closing Remarks on Vorticity Confinement

It has been shown that the method of Vorticity Confinement can be utilized to confine the trailing vortices, both for steady fixed-wing calculations and for unsteady periodic rotary-wing cases. However, there is still a lot of work that needs to be addressed

in order to identify the best value of the confinement parameter ϵ for a given case. Discretization errors, numerical diffusion, numerical schemes and geometries all have to be taken into account. The values used in this chapter for both fixed-wing and rotary-wing calculations have come from trial and error.

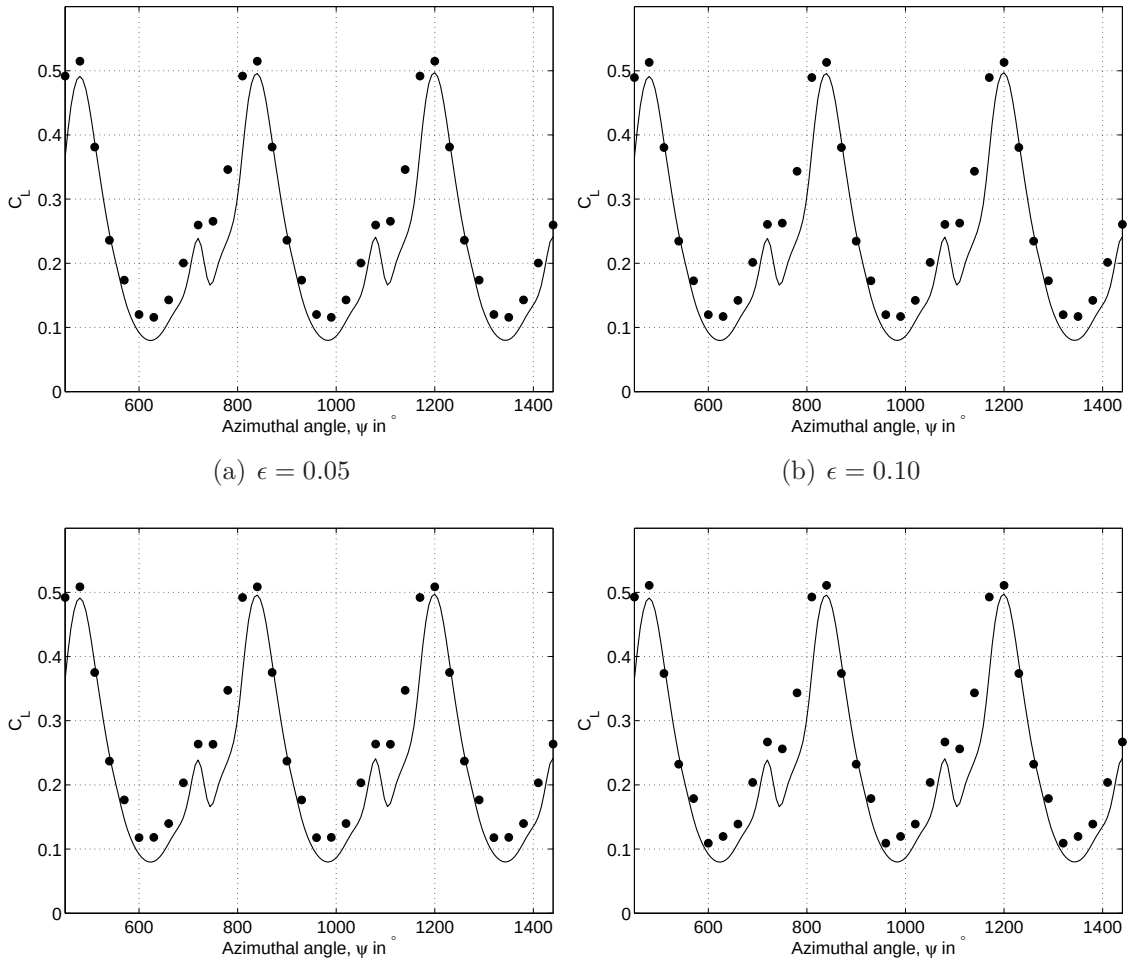

(a) $\epsilon = 0.05$ (b) $\epsilon = 0.10$

(c) $\epsilon = 0.15$ (d) $\epsilon = 0.20$

Figure 6.4: Coefficient of lift per blade vs. the azimuth of a lifting rotor in forward flight using Euler calculation with the JST dissipation scheme combined with Vorticity Confinement: $M_t = 0.7$, $\mu = 0.2857$, $\theta_c = 8°$, $N = 12$, • computed result from the current work using the JST dissipation scheme with Vorticity Confinement, — simulation result provided Allen.

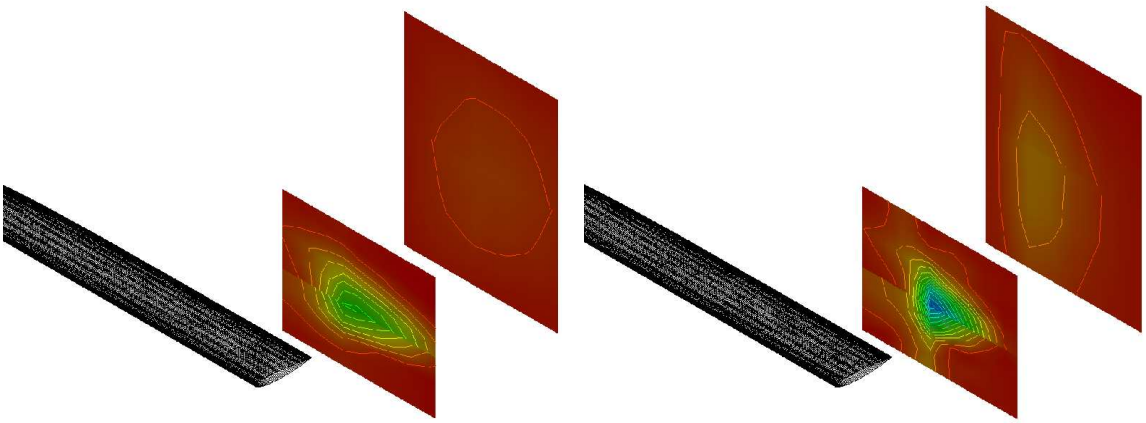

(a) $\epsilon = 0$ (b) $\epsilon = 0.2$

Figure 6.5: Vorticity magnitude of a lifting rotor in forward flight at the cut-planes $x = 2$ and $x = 5$ with $160 \times 48 \times 48$ mesh cells: $M_t = 0.7$, $\mu = 0.2857$, $\theta_c = 8°$, $N = 12$, $\psi = 90°$.

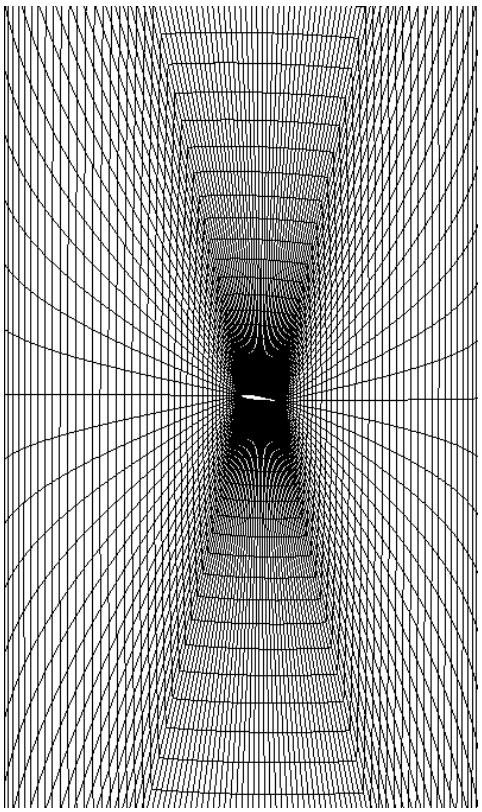

Figure 6.6: Mesh cross section at the tip of of the blade

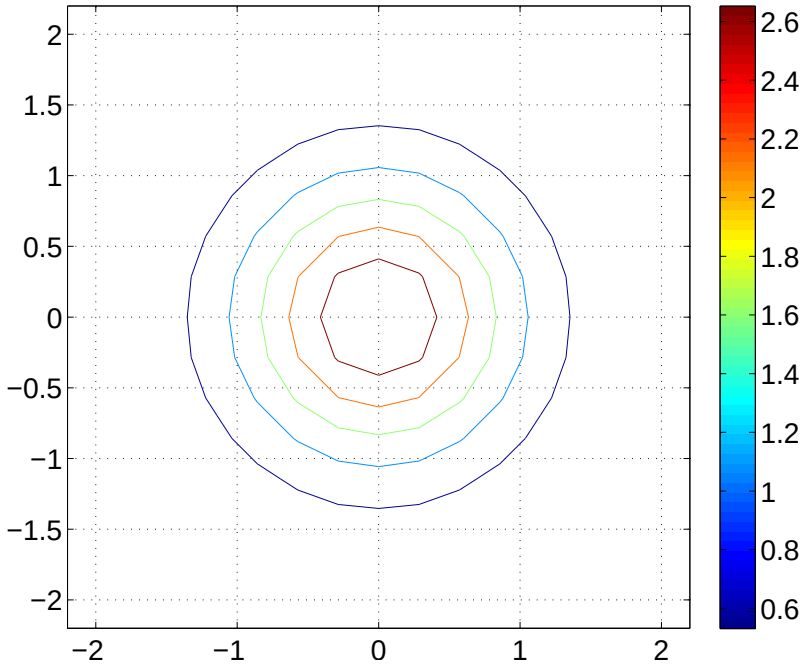

Figure 6.7: Initial vorticity profile of a model problem with the Lamb–Oseen vortex: $r_c = 1$ and $\Gamma = 10$.

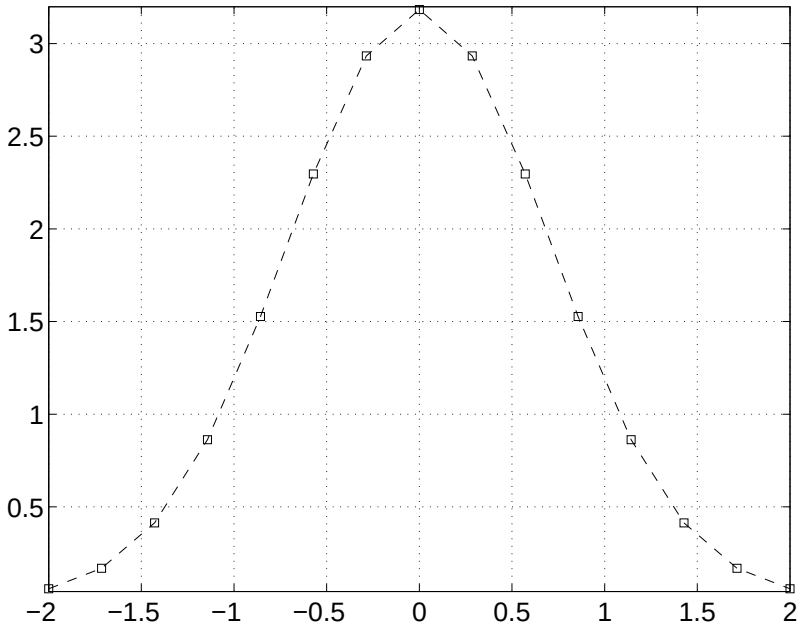

Figure 6.8: Vorticity distribution in the radial direction of a model problem with the Lamb–Oseen vortex: $r_c = 1$ and $\Gamma = 10$.

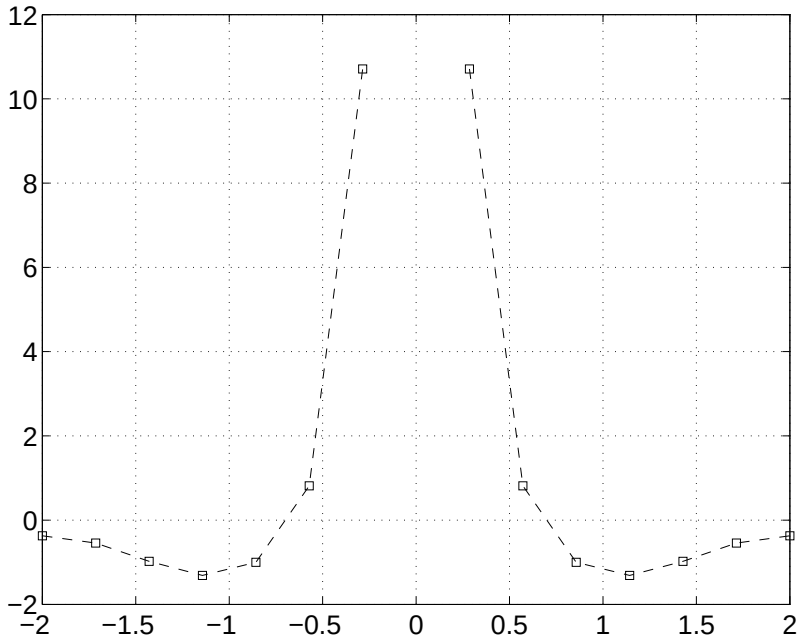

Figure 6.9: Values of the curl of the confinement term, $\vec{\nabla} \times \mathbf{s}$, for the Lamb–Oseen vortex model problem.

Chapter 7

Conclusion and Future Work

The work in this thesis has shown that the Time Spectral method can significantly reduce computational time in rotorcraft simulation by as much as 10 times in comparison to traditional BDF time stepping schemes. Additionally, the method is easier to adapt to existing flow solvers compared to other nonlinear frequency domain type methods. The applicability of the method depends on the nature of problems. If a problem requires many modes to resolve the smallest frequency within a period, this method will become expensive very quickly because the Fourier collocation matrix multiplication process. For this class of problems, a traditional BDF time stepping would be more suitable.

A new Vorticity Confinement formulation has been developed. The new formulation works well for fixed-wing aircraft calculations. When applied to rotorcraft calculation, the increase in confinement can be observed. However, when the confinement parameter increases past a certain threshold, the aerodynamic prediction becomes inaccurate and the stability of the code is questionable. At the present state, the method still lacks strong mathematical foundation underlying its basic concept. Additionally, there has been no attempt to calibrate the confinement parameter even for a simple case such as flow past a cylinder. The confinement value is usually obtained through the process of trial and error, and this strongly depends on the code and mesh topology, as well as the numerical schemes used in computation. As a result,

Vorticity Confinement is still a subject under investigation, and will require considerable effort in standardizing before it can become a reliable tool for computational fluid dynamicists.

7.1 Recommendations for Future Work

The main objective of the work in this thesis is to investigate the benefits of the Time Spectral method for rotorcraft simulation. Therefore there are areas in other aspects of rotorcraft simulation that have been omitted. The following subsections describe the aspects that should next be considered in order to drive the current work closer to a more realistic and accurate prediction.

7.1.1 Articulated Rotor

The blades studied in the current research are rigid, untwisted and untapered with constant collecting and cyclic pitches. Implementing simulations of tapered and/or linearly twisting blades is a straightforward process with the current code because the internal mesh generator has the capability to handle these features given the correct input geometric values. However, these geometric features have to be prescribed beforehand and the blades will retain the prescribed geometry variation throughout the entire simulation.

7.1.2 Aeroelasticity

A real helicopter blade is highly flexible and to obtain a more accurate result, aeroelasticity should be included since blade deformations are an integral part of the rotor movement. The flow solver can be coupled to a commercial finite element package such as NASTRAN, and the deformation can be calculation after a certain number of time steps for either weak or strong coupling.

7.1.3 Inclusion of Fuselage and Tail Rotor

Addition of the fuselage and tail rotor will have noticeable effects on the flow field generated by the main rotor. In order to implement this, major modifications have to be made to the current code since it must be able to handle real multi-block configurations (the current code is a pseudo multi-block code where a single block of mesh is generated and is subdivided into equal parts for each processor). An external mesh generator will also be required. In which case, using an unstructured steady state flow solver as a starting point may be more practical since the Time Spectral method can be easily added.

Appendix A

Numerical Method Background

Appendix A contains some background in numerical method for the calculations presented in this thesis. Section A.1 presents the way in which the governing equations are non-dimensionalized. Section A.2 presents theory of positivity and finally, section A.3 presents the theorem of local extremum diminishing (LED) schemes, which provides conditions for a scheme to be non-oscillatory.

A.1 Non-Dimentionalization

Consider the flow equations in integral form:

$$\int_{\Omega} \frac{\partial \mathbf{w}}{\partial t} \, \mathrm{d}\mathcal{V} + \oint_{\partial\Omega} \mathbf{f}_j \cdot \mathbf{n} \, \mathrm{d}\mathcal{S} = 0. \tag{A.1}$$

Non-dimensionalization of the governing equations can be achieved by dividing the dimensional quantities by the characteristic or reference properties, denotes by

the 0 subscript. The dimensionless quantities will be noted by the * superscript:

$$
\begin{aligned}
x_i^* &= \frac{x_i}{x_0} & t^* &= \sqrt{\frac{p_0}{\rho_0}}\left(\frac{t}{x_0}\right) \\
\rho^* &= \frac{\rho}{\rho_0} & u_i^* &= \sqrt{\frac{\rho_0}{p_0}}u_i \\
b_i^* &= \sqrt{\frac{\rho_0}{p_0}}b_i & E^* &= \frac{\rho_0 E}{p_0} \\
\mu^* &= \frac{\mu}{\mu_0}
\end{aligned}
$$

The volumetric and flux integrals of the conservation equations can be written in dimensionless form as:

$$
\int_\Omega \frac{\partial \mathbf{w}}{\partial t}\,\mathrm{d}\mathcal{V} = x_0^2 \begin{bmatrix} \sqrt{p_0\rho_0} \\ p_0 \\ p_0 \\ p_0 \\ \sqrt{\frac{p_0^3}{\rho_0}} \end{bmatrix} \int_\Omega \frac{\partial \mathbf{w}^*}{\partial t^*}\,\mathrm{d}\mathcal{V}^* \tag{A.2}
$$

$$
\oint_{\partial\Omega} \mathbf{f}_c \cdot \mathbf{n}\,\mathrm{d}\mathcal{S} = x_0^2 \begin{bmatrix} \sqrt{p_0\rho_0} \\ p_0 \\ p_0 \\ p_0 \\ \sqrt{\frac{p_0^3}{\rho_0}} \end{bmatrix} \oint_{\partial\Omega} \mathbf{f}_c^* \cdot \mathbf{n}^*\,\mathrm{d}\mathcal{S}^* \tag{A.3}
$$

$$
\oint_{\partial\Omega} \mathbf{f}_v \cdot \mathbf{n}\,\mathrm{d}\mathcal{S} = x_0^2 \begin{bmatrix} 0 \\ \frac{\mu_0}{x_0}\sqrt{\frac{p_0}{\rho_0}} \\ \frac{\mu_0}{x_0}\sqrt{\frac{p_0}{\rho_0}} \\ \frac{\mu_0}{x_0}\sqrt{\frac{p_0}{\rho_0}} \\ \frac{\mu_0}{x_0}\frac{p_0}{\rho_0} \end{bmatrix} \oint_{\partial\Omega} \mathbf{f}_v^* \cdot \mathbf{n}^*\,\mathrm{d}\mathcal{S}^* \tag{A.4}
$$

The non-dimensionalized equations become:

$$\int_\Omega \frac{\partial \mathbf{w}^*}{\partial t^*}\,\mathrm{d}\mathcal{V}^* + \oint_{\partial\Omega} \mathbf{f}_c^* \cdot \mathbf{n}^*\,\mathrm{d}\mathcal{S}^* + \frac{\mu_0}{x_0\sqrt{p_0\rho_0}} \oint_{\partial\Omega} \mathbf{f}_v^* \cdot \mathbf{n}^*\,\mathrm{d}\mathcal{S}^* = \int_\Omega \frac{\partial \mathbf{w}^*}{\partial t^*}\,\mathrm{d}\mathcal{V}^* + \oint_{\partial\Omega} \mathbf{f}_c^* \cdot \mathbf{n}^*\,\mathrm{d}\mathcal{S}^* + \sqrt{\gamma}\frac{\mathrm{M}_0}{\mathrm{Re}_0} \oint_{\partial\Omega} \mathbf{f}_v^* \cdot \mathbf{n}^*\,\mathrm{d}\mathcal{S}^* \quad \text{(A.5)}$$

The reference quantity M_0 and Re_0 almost always refer to the tip location of the helicopter blade in helicopter simulations.

A.2 Theory of Positivity

Consider a general explicit scheme in one dimension:

$$v_i^{n+1} = \sum_j a_{ij} v_i^n. \quad \text{(A.6)}$$

If this is consistent with a differential equation with no source such as

$$\frac{\partial u}{\partial t} + \frac{\partial}{\partial x} f(u) = 0 \qquad \text{or} \qquad \frac{\partial u}{\partial t} = \sigma \frac{\partial^2 u}{\partial x^2},$$

then

$$\sum_j a_{ij} = 1 \quad \text{(A.7)}$$

since

$$v(x,t) + \Delta t \frac{\partial v}{\partial t} + \frac{\Delta t^2}{2}\frac{\partial^2 v}{\partial t^2} + \ldots = \sum_j a_{ij} \left\{ v(x,t) + (j-i)\Delta x \frac{\partial v}{\partial x} + (j-i)^2 \frac{\Delta x^2}{2}\frac{\partial^2 v}{\partial x^2} + \ldots \right\}$$

Also

$$\begin{aligned}\left|v_i^{n+1}\right| &\leq \sum_j |a_{ij}| \left|v_j^n\right| \\ &\leq \left(\sum_j |a_{ij}|\right) \max_j \left|v_j^n\right| \\ &= \sum_j |a_{ij}| \, |v^n|_\infty .\end{aligned}$$

Hence $|v^{n+1}|_\infty \leq |v^n|_\infty$ if

$$\sum_j |a_{ij}| \leq 1. \tag{A.8}$$

However, if $v_j = \pm 1$ according to signs of a_{ij}, then

$$\left|v_i^{n+1}\right| = \sum_j |a_{ij}| .$$

In order to satisfy (A.7) and (A.8), note that if a_{ij} do not all have the same sign,

$$\sum_j |a_{ij}| > \sum_j a_{ij} > 1.$$

Also for $\sum_j a_{ij} = 1$, all a_{ij} must then be ≥ 0. Therefore the condition for stability is that all the coefficients a_{ij} must be non-negative, i.e.

$$a_{ij} \geq 0. \tag{A.9}$$

A.3 Local Extremum Diminishing (LED) Schemes

For any scheme that exhibits non-oscillatory behavior, the scheme should fall under the terms of the local extremum diminishing (LED) condition, which states that maxima should not increase and minima should not decrease, i.e. this is equivalent to stability in L_∞ norm, with the additional condition that local extrema cannot

increase. This principle can be used for multi-dimensional problems for both structured and unstructred meshes. The LED scheme is equivalent to the total variation diminishing (TVD) for one-dimensional problems.

Consider an equation of a time dependent conservation law in two dimensions:

$$\frac{\partial v}{\partial t} + \frac{\partial}{\partial x} f(v) + \frac{\partial}{\partial y} g(v) = 0, \tag{A.10}$$

where v is the scalar dependent variable on an arbitrary mesh. Let v_j be the value of v at mesh point j. In semi-discrete form, we can express the approximation of (A.10) as

$$\frac{\mathrm{d}v_j}{\mathrm{d}t} = \sum_k c_{jk} v_k.$$

Upon introducing Taylor series expansion for $v(x_k - x_j, y_k - y_j)$, it follows that in the absence of a source term

$$\sum_k c_{jk} = 0. \tag{A.11}$$

Without any loss of generality, one can rewrite equation (A.11) as

$$\frac{\mathrm{d}v_j}{\mathrm{d}t} = \sum_{k \neq j} c_{jk} \left(v_k - v_j \right).$$

If the coefficients c_{jk} are positive;

$$c_{jk} \geq 0, \qquad k \neq j.$$

The above condition ensures that the scheme is stable in L_∞ norm. For a compact scheme where $c_{jk} = 0$ if j and k are not the nearest neighbors, then v_j is a local maximum, i.e. $v_k - v_j \leq 0$. The consequence of this implies that

$$\frac{\mathrm{d}v_j}{\mathrm{d}t} \leq 0.$$

Hence the local maximum cannot increase and a local minimum cannot decrease. Such a scheme is termed local extremum diminishing (LED).

Appendix B

Matrix Operator for Numerical Differentiation

B.1 Fourier Collocation Matrix

This section discusses details of compact representation of the spectral Fourier derivative operator in the physical space, instead of the wave space. The derivation is based on lecture notes of Moin (2003).

Assume that f is a function with a period of 2π defined on the grid

$$x_j = \frac{2\pi j}{N} \qquad \text{where} \qquad j = 0, 1, 2, \ldots, N-1.$$

Forward and backward discrete Fourier transform of u is given by

$$\hat{f}_k = \frac{1}{N} \sum_{j=0}^{N-1} f(x_j) \mathrm{e}^{-\mathrm{i}kx_j} \tag{B.1}$$

and

$$f(x_j) = \sum_{k=-\frac{N}{2}}^{\frac{N}{2}-1} \hat{f}_k \, \mathrm{e}^{\mathrm{i}kx_j}. \tag{B.2}$$

The Fourier transform of the derivative approximations is computed by multiplying

the Fourier transform of f by ik. Therefore

$$\widehat{Df}_k = \mathrm{i}k\hat{f}_k. \tag{B.3}$$

In practice, the Fourier coefficient corresponding to the *oddball* wave number is set to zero to ensure that the derivative remains real in the physical space (if N is even), i.e.

$$\widehat{Df}_{-\frac{N}{2}} = 0.$$

For the inverse transform, the derivative at point j is then

$$\left.\frac{\partial f}{\partial x}\right|_j = \sum_{k=-\frac{N}{2}+1}^{\frac{N}{2}-1} \widehat{Df}_k \, \mathrm{e}^{\mathrm{i}kx_j}. \tag{B.4}$$

Using (B.3) and (B.4), (B.2) can be written as

$$(Df)_j = \sum_{k=-\frac{N}{2}+1}^{\frac{N}{2}-1} \mathrm{i}k\hat{f}_k \, \mathrm{e}^{\mathrm{i}kx_j}. \tag{B.5}$$

By substituting (B.1) into (B.5), we obtain

$$\begin{aligned}(Df)_l &= \frac{1}{N} \sum_{k=-\frac{N}{2}+1}^{\frac{N}{2}-1} \sum_{j=0}^{N-1} \mathrm{i}kf(x_j) \, \mathrm{e}^{-\mathrm{i}kx_j} \mathrm{e}^{\mathrm{i}kx_l} \\ &= \frac{1}{N} \sum_k \sum_j \mathrm{i}kf(x_j) \, \mathrm{e}^{\frac{\mathrm{i}2\pi k}{N}(l-j)}.\end{aligned}$$

Let

$$d_{lj} = \frac{1}{N} \sum_{k=-\frac{N}{2}+1}^{\frac{N}{2}-1} \mathrm{i}k \, \mathrm{e}^{\mathrm{i}\frac{2\pi k}{N}(l-j)}, \tag{B.6}$$

then the derivative of each grid point is given by

$$(Df)_l = \sum_{j=0}^{N-1} d_{lj} f(x_j). \tag{B.7}$$

One can see that the term d_{lj} in the right hand side of (B.7) is the multiplication with the matrix D, and the vector $\vec{f}$ with elements f_l. In order to simplify the expression for d_{lj}, first consider the geometric series

$$S = \sum_{k=-\frac{N}{2}+1}^{\frac{N}{2}-1} \mathrm{e}^{\mathrm{i}kx} = \frac{\sin\left(\frac{N-1}{2}x\right)}{\sin\frac{x}{2}}.$$

Differentiating the above series yields

$$\frac{\mathrm{d}S}{\mathrm{d}x} = \sum_{k=-\frac{N}{2}+1}^{\frac{N}{2}-1} \mathrm{i}k\,\mathrm{e}^{\mathrm{i}kx} = \frac{\left[\frac{N-1}{2}\right]\cos\left(\frac{N-1}{2}x\right)\sin\frac{x}{2} - \frac{1}{2}\cos\frac{x}{2}\sin\left(\frac{N-1}{2}x\right)}{\left(\sin\frac{x}{2}\right)^2}. \tag{B.8}$$

Using the following trigonometric identities:

$$\begin{aligned}
\sin\left(\frac{Nx}{2} - \frac{x}{2}\right) &= \sin\frac{Nx}{2}\cos\frac{x}{2} - \cos\frac{Nx}{2}\sin\frac{x}{2} \\
\cos\left(\frac{Nx}{2} - \frac{x}{2}\right) &= \cos\frac{Nx}{2}\cos\frac{x}{2} - \sin\frac{Nx}{2}\sin\frac{x}{2}.
\end{aligned}$$

From our initial assumption, note that in (B.6)

$$x = \frac{2\pi}{N}(l-j). \tag{B.9}$$

Using the trigonometric identities and substitute (B.9) into (B.8), we obtain

$$\frac{\mathrm{d}S}{\mathrm{d}x} = \frac{N}{2}(-1)^{l-j}\cot\left\{\frac{\pi(l-j)}{N}\right\}.$$

Finally, one can simplify (B.6) as

$$d_{lj} = \begin{cases} \frac{1}{2}(-1)^{l-j} \cot\left\{\frac{\pi(l-j)}{N}\right\} & : \quad l \neq j \\ 0 & : \quad l = j \end{cases} .$$

The operation count for the multiplication of a matrix and a vector is $\mathcal{O}(N^2)$ operations. Although this is more expensive than the fast Fourier transform method, which requires $\mathcal{O}(N \log_2 N)$, using the Fourier collocation matrix greatly simplifies the problem. In practice, the total operation counts using the Fourier collocation matrix could be lower than FFT for small N because the Time Spectral method avoids the multiple Fourier transforms and inverse Fourier transforms that one would have to perform during each time step. Additionally, N is generally small, e.g. $4 \leq N \leq 12$.

Appendix C

Lifting Rotor in Forward Flight Plots

This chapter lists complete C_p plots at the span station $z = 0.9$ for cases 1–3 of table 5.2 from chapter 5. The results shown in this Appendix are for three different mesh sizes using either the JST and CUSP artificial dissipation schemes. The results are compared against the simulation results provided by Professor Chris Allen of the University of Bristol, United Kingdom.

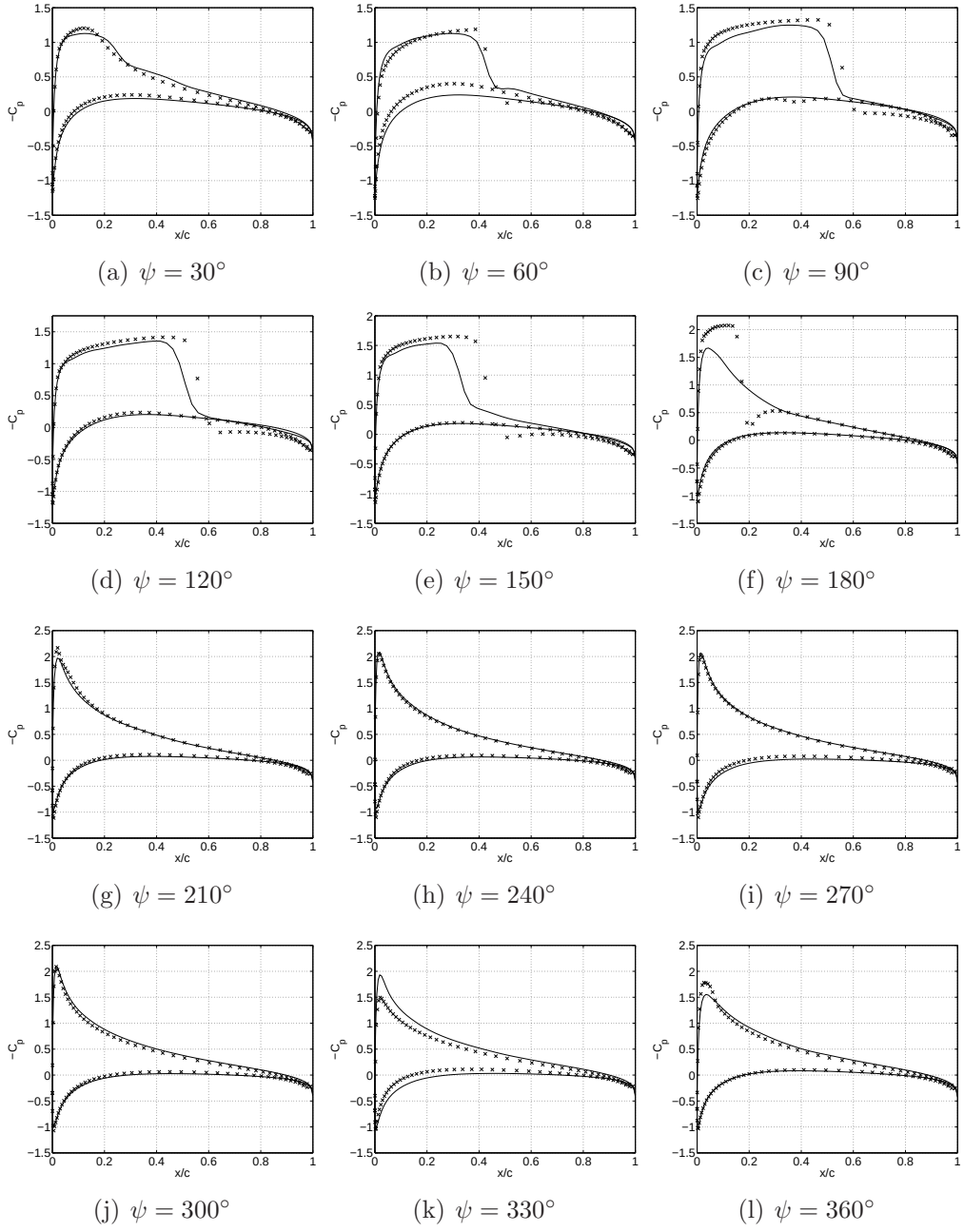

(a) $\psi = 30°$ (b) $\psi = 60°$ (c) $\psi = 90°$

(d) $\psi = 120°$ (e) $\psi = 150°$ (f) $\psi = 180°$

(g) $\psi = 210°$ (h) $\psi = 240°$ (i) $\psi = 270°$

(j) $\psi = 300°$ (k) $\psi = 330°$ (l) $\psi = 360°$

Figure C.1: Coefficient of pressure at $r/R = 0.90$ using the JST dissipation scheme with $128 \times 48 \times 32$ mesh cells, $M_t = 0.7$, $\mu = 0.2857$, $\theta_c = 8°$, $N = 12$: — computed result, $\times$ result provided by Allen.

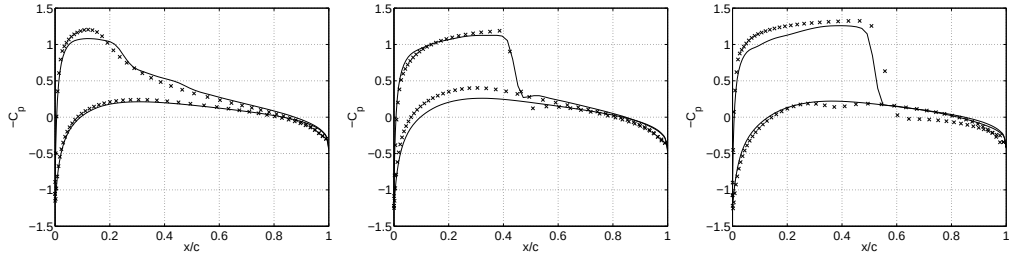

(a) $\psi = 30°$ (b) $\psi = 60°$ (c) $\psi = 90°$

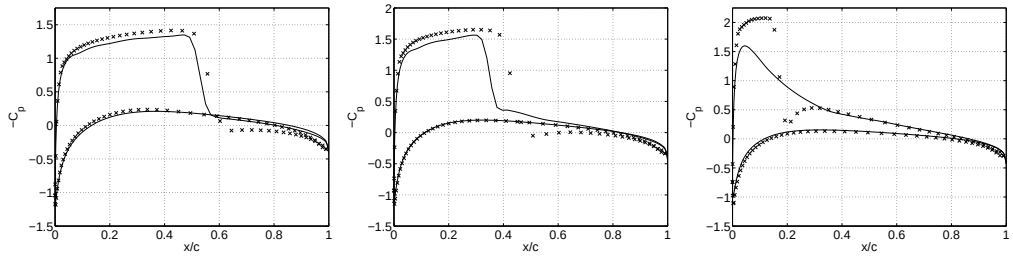

(d) $\psi = 120°$ (e) $\psi = 150°$ (f) $\psi = 180°$

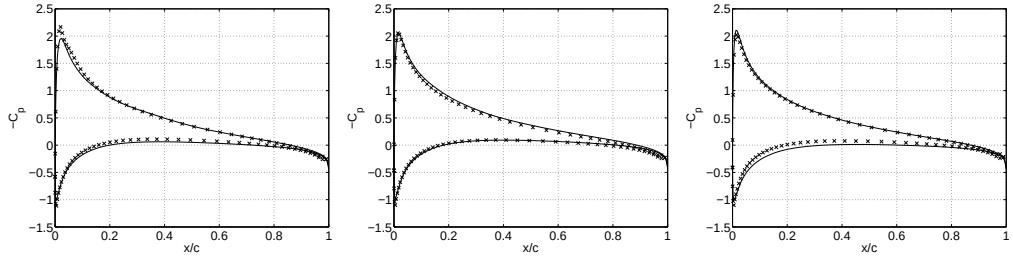

(g) $\psi = 210°$ (h) $\psi = 240°$ (i) $\psi = 270°$

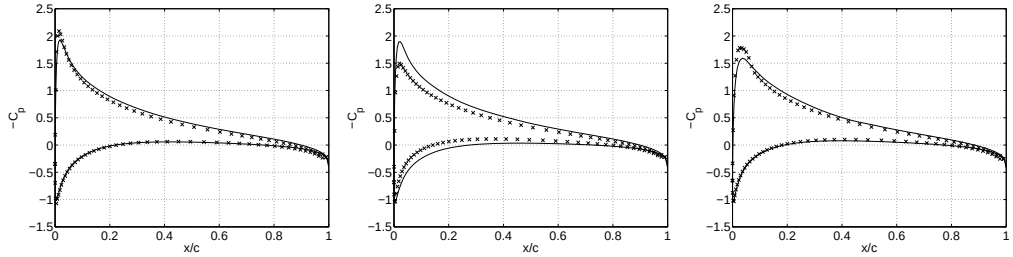

(j) $\psi = 300°$ (k) $\psi = 330°$ (l) $\psi = 360°$

Figure C.2: Coefficient of pressure at $r/R = 0.90$ using the JST dissipation scheme with $160 \times 48 \times 48$ mesh cells, $\mathrm{M}_t = 0.7$, $\mu = 0.2857$, $\theta_c = 8°$, $N = 12$: — computed result, $\times$ result provided by Allen.

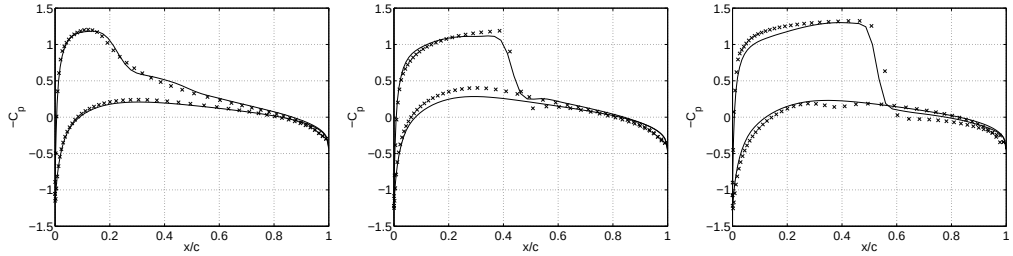

(a) $\psi = 30°$ (b) $\psi = 60°$ (c) $\psi = 90°$

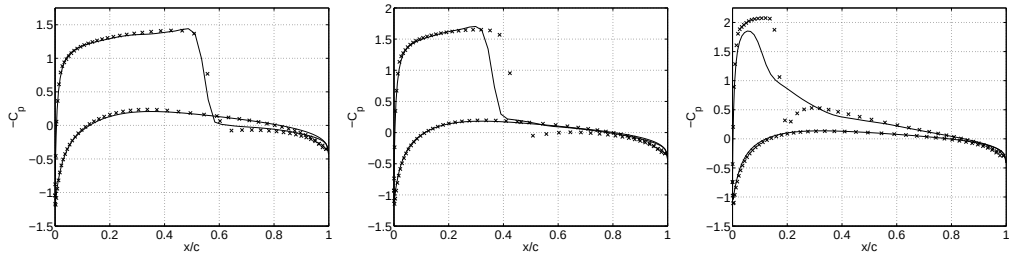

(d) $\psi = 120°$ (e) $\psi = 150°$ (f) $\psi = 180°$

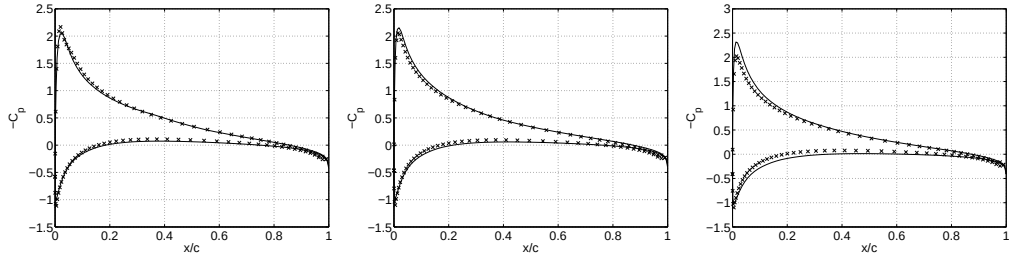

(g) $\psi = 210°$ (h) $\psi = 240°$ (i) $\psi = 270°$

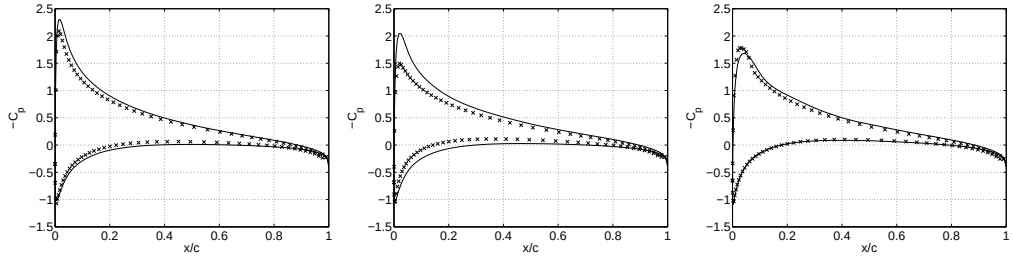

(j) $\psi = 300°$ (k) $\psi = 330°$ (l) $\psi = 360°$

Figure C.3: Coefficient of pressure at $r/R = 0.90$ using the CUSP dissipation scheme with $128 \times 48 \times 32$ mesh cells, $\mathrm{M}_t = 0.7$, $\mu = 0.2857$, $\theta_c = 8°$, $N = 12$: — computed result, $\times$ result provided by Allen.

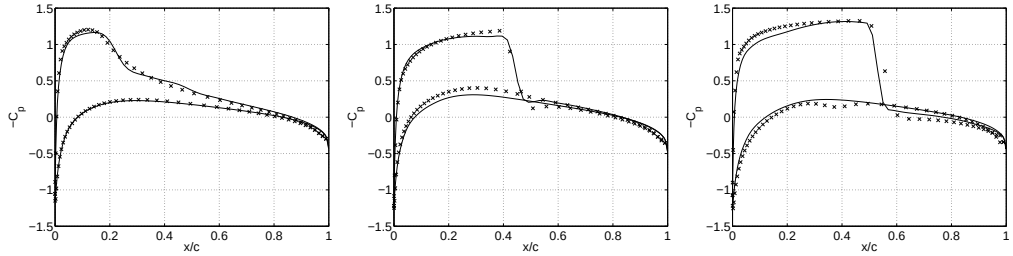

(a) $\psi = 30°$ (b) $\psi = 60°$ (c) $\psi = 90°$

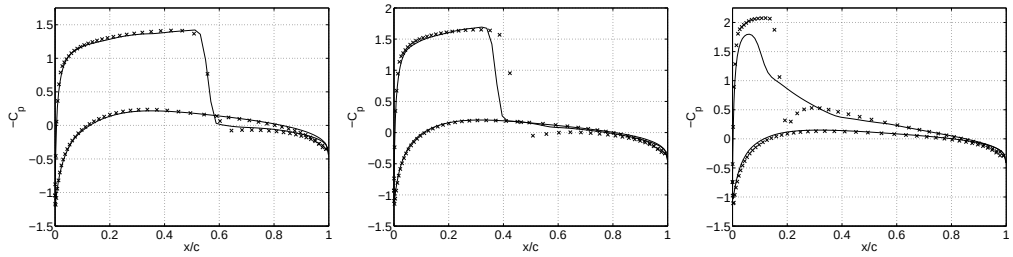

(d) $\psi = 120°$ (e) $\psi = 150°$ (f) $\psi = 180°$

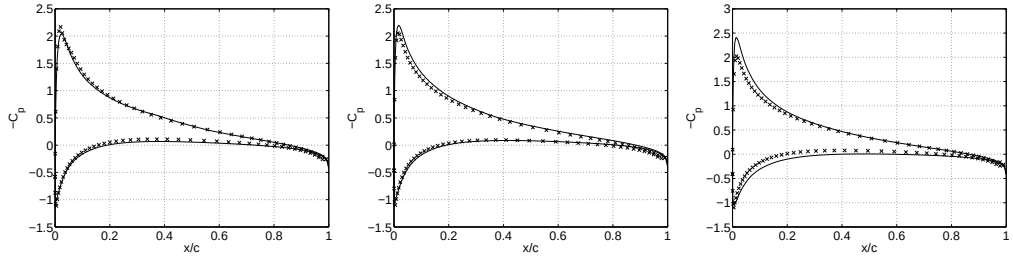

(g) $\psi = 210°$ (h) $\psi = 240°$ (i) $\psi = 270°$

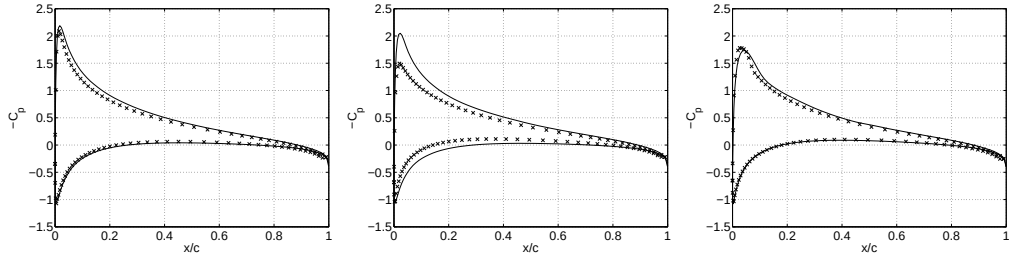

(j) $\psi = 300°$ (k) $\psi = 330°$ (l) $\psi = 360°$

Figure C.4: Coefficient of pressure at $r/R = 0.90$ using the CUSP dissipation scheme with $160 \times 48 \times 48$ mesh cells, $\mathrm{M}_t = 0.7$, $\mu = 0.2857$, $\theta_c = 8°$, $N = 12$: — computed result, $\times$ result provided by Allen.

Bibliography

Agarwal, R. K. & Deese, J. E. 1987 Euler Calculations for Flowfield of a Helicopter Rotor in Hover. *Journal of Aircraft* **24** (4), 231–238.

Agarwal, R. K. & Deese, J. E. 1988 Navier–Stokes Calculations of the Flowfield of a Helicopter Rotor in Hover. In *AIAA 26th Aerospace Sciences Meeting & Exhibit*. Reno, NV, AIAA Paper 1988–0106.

Allen, C. B. 2003*a* Convergence of Steady and Unsteady Formulations for Inviscid Hovering Rotor Solutions. *International Journal of Numerical Analysis and Modeling* **41** (9), 931–949.

Allen, C. B. 2003*b* Numerical Simulation of Multi-Bladed Rotors in Lifting Forward Flight. In *AIAA 21st Applied Aerodynamics Conference*. Orlando, FL, AIAA Paper 2003–4080.

Allen, C. B. 2004*a* Multi-Bladed lifting Rotor Simulation in Hover, Forward Flight, and Ground Effect. In *AIAA 22nd Applied Aerodynamics Conference*. Providence, RI, AIAA Paper 2004–5288.

Allen, C. B. 2004*b* An unsteady multiblock multigrid scheme for lifting forward flight rotor simulation. *International Journal for Numerical Methods in Fluids* **45** (9), 973–984.

Allen, C. B. 2006 Parallel Flow-Solver and Mesh Motion Scheme for Forward Flight Rotor Simulation. In *AIAA 24th Applied Aerodynamics Conference*. San Francisco, CA, AIAA Paper 2006–3476.

Allen, C. B. 2007 Parallel Simulation of Lifting Rotor Wakes in Forward Flight. *International Journal of Numerical Analysis and Modeling* **4** (1), 1–15.

Anderson, W. K., Thomas, J. L. & van Leer, B. 1984 A Comparison of Finite Volume Flux Vector Splittings for the Euler Equations. In *AIAA 23rd Aerospace Sciences Meeting & Exhibit*. Reno, NV, AIAA Paper 1985–0122.

Arieli, R., Taubert, M. E. & Caughey, D. A. 1985 Computation of Transonic Flow About Helicopter Rotor Blades. *AIAA Journal* **24** (5), 722–727.

Baldwin, B. & Lomax, H. 1978 Thin-Layer Approximation and Algebraic Model for Separated Turbulent Flows. In *AIAA 16th Aerospace Sciences Meeting*. Huntsville, AL, AIAA Paper 1978–0257.

Bhagwat, M., Moulton, M. A. & Caradonna, F. X. 2005 Development of a New Potential Flow Based Model for Hover Performance Prediction. In *AIAA 43rd Aerospace Sciences Meeting & Exhibit*. Reno, NV, AIAA Paper 2005–1367.

Bhagwat, M., Moulton, M. A. & Caradonna, F. X. 2006 Hybrid CFD for Rotor Hover Performance Prediction. In *AIAA 24rd Applied Aerodynamics Conference*. San Francisco, CA, AIAA Paper 2006–3474.

Biava, M. & Vigevano, L. 2002 The Effect of Far-Field Boundary Condition on Tip Vortex Path Predictions in Hovering. In *CEAS Aerospace Aerodynamics Research Conference*. Cambridge.

Boelens, O. J., van der Ven, H., Oskam, B. & Hassan, A. A. 2000 Accurate and Efficient Vortex-Capturing for a Helicopter Rotor in Hover. *Tech. Rep.* NLR–TP–2000–420. Nationaal Lucht- en Ruimtevaartlaboratorium.

Boniface, J. C. and Sidès, J. 1993 Numerical Simulation of Steady and Unsteady Euler Flows Around Multibladed Helicopter Rotors. *Tech. Rep.* ONERA TP 1991–177. Office National d'Études et de Recherches Aérospatiale, Presented at the 17th European Rotorcraft Forum, Berlin, Federal Republic of Germany, September 1991.

Brandt, A. 1977 Multi-Level Adaptive Solutions to Boundary-Value Problems. *Mathematics of Computation* **31**, 333–390.

Canuto, C., Hussaini, M. Y., Quarteroni, A. & Zang, T. A. 2007 *Spectral Methods: Evolution to Complex Geometries and Applications to Fluid Dynamics*, 1st edn. Springer–Verlag New York, LLC.

Caradonna, F. X. 2000 Developments and Challenges in Rotorcraft Aerodynamics. In *AIAA 38th Aerospace Sciences Meeting & Exhibit*. Reno, NV, AIAA Paper 2000–0109.

Caradonna, F. X. & Isom, M. P. 1972 Subsonic and Transonic Potential Flow over Helicopter Rotor Blades. *AIAA Journal* **10** (12), 1606–1612.

Caradonna, F. X. & Isom, M. P. 1976 Numerical Calculation of Unsteady Transonic Potential Flow over Helicopter Rotor Blades. *AIAA Journal* **14** (4), 482–488.

Caradonna, F. X., Laub, G. H. & Tung, C. 1984 An Experimental Investigation of the Parallel Blade–Vortex Interaction. *Tech. Rep.* NASA Technical Memorandum 86005. National Aeronautics and Space Administration.

Caradonna, F. X., Lautenschlager, J. L. & Silva, M. J. 1988 An Experimental Study of Rotor–Vortex Interactions. In *AIAA 26th Aerospace Sciences Meeting & Exhibit*. Reno, NV, AIAA Paper 1988–0045.

Caradonna, F. X. & Philippe, J. J. 1978 The Flow Over a Helicopter Blade Tip in the Transonic Regime. *Vertica* **2**, 43–60.

Caradonna, F. X. & Tung, C. 1981 Experimental and Analytical Studies of a Model Helicopter Rotor in Hover. *Tech. Rep.* NASA Technical Memorandum 81232. National Aeronautics and Space Administration.

Chattot, J.-J. & Phillipe, J.-J. 1980 Pressure Distribution Computation on a Non-Lifting Symmetrical Helicopter Blade in Forward Flight. *La Recherche Aérospatiale* (1980–5), 19–33.

Chen, C. L., McCroskey, W. J. & Obayashi, S. 1990 Numerical Simulations of Forward-Flight Rotor Flow Using an Upwind Method. *Journal of Aircraft* **28** (6), 374–380, Presented as Paper 1989–1846 at the AIAA 20th Fluid Dynamics, Plasmadynamics and Lasers Conference, Buffalo, NY, June 1989.

Conlisk, A. T. 1997 Modern Helicopter Aerodynamics. *Annual Review of Fluid Mechanics* **29**, 515–567.

Crank, J. & Nicolson, P. 1947 A Practical Method for Numerical Evaluation of Solutions of Partial Differential Equations of the Heat-Conduction Type. In *Proceedings of the Cambridge Philosophical Society*, , vol. 43, pp. 50–67.

Dadone A., Hu, G. & Grossman, B. 2001 Towards a Better Understanding of Vorticity Confinement Methods in Compressible Flow. In *AIAA 15th Computational Fluid Dynamics Conference*. Anaheim, CA, AIAA Paper 2001–2639.

Dahlquist, G. 1956 Convergence and Stability in the Numerical Integration of Ordinary Differential Equations. *Mathematica Scandinavica* **4**, 33–53.

Dahlquist, G. 1959 Stability and Error Bounds in the Numerical Integration of Ordinary Differential Equations. *Transactions of the Royal Institute of Technology, Stockholm* (130), 87.

Dietz, W. 2004 Application of Vorticity Confinement to Compressible Flow. In *AIAA 42th Aerospace Sciences Meeting & Exhibit*. Reno, NV, AIAA Paper 2004–0718.

Dietz, W., Fan, M., Steinhoff, J. & Wenren, Y. 2001 Application of Vorticity Confinement to the Prediction of Flows Over Complex Bodies. In *AIAA 15th Computational Fluid Dynamics Conference*. Anaheim, CA, AIAA Paper 2001–2642.

Ekici, K., Hall, K. C. & Dowell, E. H. 2008 Computationally Fast Harmonic Balance Methods for Unsteady Aerodynamic Predictions of Helicopter Rotors. In *AIAA 46th Aerospace Sciences Meeting & Exhibit*. Reno, NV, AIAA Paper 2008–1439.

Fan, M. & Steinhoff, J. 2004 Computation of Blunt Body Wake Flow by Vorticity Confinement. In *AIAA 42th Aerospace Sciences Meeting & Exhibit*. Reno, NV, AIAA Paper 2004–0592.

Federenko, R. P. 1964 The Speed of Convergence of One Iterative Process. *U.S.S.R. Computational Mathematics and Mathematical Physics* **4** (3), 227–235.

Fedkiw, R., Stam, J. & Jensen, H. W. 2001 Visual Simulation of Smoke. In *International Conference on Computer Graphics and Interactive Techniques, Proceedings of the 28th Annual Conference on Computer Graphics and Interactive Techniques*, pp. 15–22.

Friedmann, P. P. 2004 Rotary-Wing Aeroelasticity: Current Status and Future Trends. *AIAA Journal* **42** (10), 1953–1972.

Gopinath, A. K. 2007 Efficient Fourier-Based Algorithms for Time-Periodic Unsteady Problems. PhD thesis, Stanford University.

Gopinath, A. K. & Jameson, A. 2005 Time Spectral Method for Periodic Unsteady Computations over Two- and Three-Dimensional Bodies. In *AIAA 43th Aerospace Sciences Meeting & Exhibit*. Reno, NV, AIAA Paper 2005–1220.

Gopinath, A. K., van der Weide, E., Alonso, J. J., Jameson, A., Ekici, K. & Hall, K. 2007 Three-Dimensional Unsteady Multi-stage Turbomachinery Simulations Using the Harmonic Balance Technique. In *AIAA 45th Aerospace Sciences Meeting & Exhibit*. Reno, NV, AIAA Paper 2007–0892.

Hall, K. C., Thomas, J. P. & Clark, W. S. 2002 Computation of Unsteady Nonlinear Flows in Cascades Using a Harmonic Balance Technique. *AIAA Journal* **40** (5).

Harten, A 1978 The Artificial Compression Method for Computation of Shocks and Contact Discontinuities: III. Self-Adjusting Hybrid Schemes. *Mathematics of Computation* **32** (10), 363–389.

Hassan, A. A., Tung, C. & Sankar, L. N. 1992 Euler Solutions for Self-Generated Rotor Blade–Vortex Interactions. *International Journal for Numerical Methods in Fluids* **15**, 427–451, Presented as AIAA paper 1990–1588 at the AIAA 20th Fluids, Plasma Dynamics Conference, Buffalo, New York, June 1990.

Holmes, D. G. & Tong, S. S. 1984 A Three-Dimensional Euler Solver for Turbomachinery Blade Rows. In *American Society of Mechanical Engineers, International Gas Turbine Conference and Exhibit*. Amsterdam, The Netherlands.

Hsu, J. & Jameson, A. 2002 An Implicit–Explicit Hybrid Scheme for Calculating Complex Unsteady Flows. In *AIAA 40th Aerospace Sciences Meeting & Exhibit*. Reno, NV, AIAA Paper 2002–0152.

Hu, G. & Grossman, B. 2002 The Computational of Massively Separated Flows Using Compressible Vorticity Confinement Methods. In *AIAA 40th Aerospace Sciences Meeting & Exhibit*. Reno, NV, AIAA Paper 2002–0714.

Hu, G., Grossman, B. & J., Steinhoff 2002 Numerical Method for Vorticity Confinement in Compressible Flow. *AIAA Journal* **40** (10), 1945–1953.

Jameson, A. 1974 Iterative Solution of Transonic Flows Over Airfoils and Wings, Including Flows at Mach 1. *Communications on Pure and Applied Mathematics* **27**, 283–309.

Jameson, A. 1979 Acceleration of Transonic Potential Flow Calculations on Arbitrary Meshes by the Multiple Grid Method. In *AIAA 4th Computational Fluid Dynamics Conference*. Williamsburg, VA, AIAA Paper 1979–1458.

Jameson, A. 1982 Steady State Solution of the Euler Equations for Transonic Flow. In *Proceedings of Symposium on Transonic, Shock and Multidimensional Flows* (ed. R. Meyer), pp. 37–70. Madison, WI: Academic Press.

Jameson, A. 1983 Solution of the Euler Equations For Two Dimensional Transonic by a Multigrid Method. *Applied Mathematics and Computation* **13**, 327–356.

Jameson, A. 1985*a* A Nonoscillatory Shock Capturing Scheme using Flux Limited Dissipation. In *Large-scale Computations in Fluid Mechanics; Proceedings of the 15th Summer Seminar on Applied Mathematics*, pp. 345–370.

Jameson, A. 1985*b* *Numerical Methods in Fluid Dynamics*, *Lecture Notes in Mathematics*, vol. 1127/1985, chap. Transonic Flow Calculations, pp. 156–242. Springer Berlin/Heidelberg, Princeton University MAE Report 1651, March 1984.

Jameson, A. 1986 *Multigrid Methods II*, *Lecture Notes in Mathematics*, vol. 1228, chap. Multigrid Algorithms for Compressible Flow Calculations, pp. 166–201. Springer Berlin/Heidelberg, Proceedings of the 2nd European Conference on Multigrid Methods, Cologne, October 1985.

Jameson, A. 1991 Time Dependent Calculations Using Multigrid, with Applications to Unsteady Flows Past Airfoils and Wings. In *AIAA 10th Computational Fluid Dynamics Conference*. Honolulu, HI, AIAA Paper 1991–1596.

Jameson, A. 1995*a* Analysis and Design of Numerical Schemes for Gas Dynamics 1: Artificial Diffusion, Upwind Biasing, Limiters and Their Effect on Accuracy and Multigrid Convergence. *International Journal of Computational Fluid Dynamics* **4**, 171–218.

Jameson, A. 1995*b* Analysis and Design of Numerical Schemes for Gas Dynamics 2: Artificial Diffusion and Discrete Shock Structure. *International Journal of Computational Fluid Dynamics* **5**, 1–38.

Jameson, A. 2003 *Class Notes*. Stanford University, Stanford, CA, AA 215B: Advanced Computational Fluid Dynamics.

Jameson, A. & Baker, T. J. 1983 Solution of the Euler Equations for Complex Configurations. In *AIAA 6th Computational Fluid Dynamics Conference*. Danvers, MA, AIAA Paper 1983–1929.

Jameson, A., Schmidt, W. & Turkel, E. 1981 Numerical Solutions of the Euler Equations by Finite Volume Methods Using Runge–Kutta Time-Stepping Schemes.

In *AIAA 14th Fluid and Plasma Conference*. Palo Alto, CA, AIAA Paper 1981–1259.

Jameson, A. & Yoon, S. 1987 Lower–Upper Implicit Schemes with Multiple Grids for the Euler Equations. *AIAA Journal* **25** (10).

Ji, M. 2006 Second Moment Closure Modeling for Rotating Stably Stratified Turbulent Shear Flow. PhD thesis, Stanford University.

Johnson, W. 1994 *Helicopter Theory*, unabridged revised edn. Dover Publications.

Kumar, M. & Murthy, V. R. 2007 Analysis of Flow around Multibladed Rotor Using CFD in the Frequency Domain. In *AIAA 25th Applied Aerodynamics Conference*. Miami, FL, AIAA Paper 2008–3806.

Kumar, M. & Murthy, V. R. 2008 Efficient Rotor Flow Calculation Using Multiblade Coordinate Transformed CFD Frequency Domain. In *AIAA 46th Aerospace Sciences Meeting & Exhibit*. Reno, NV, AIAA Paper 2008–0408.

van Leer, B. 1979 Towards the Ultimate Conservative Difference Scheme. V. A. Second-Order Sequel to Godunov's Method. *Journal of Computational Physics* **32**, 101–136.

Leishman, J. G. 2006 *Principles of Helicopter Aerodynamics*, 2nd edn. Cambridge University Press.

Löhner, R. & Yang, C. 2002 Vorticity Confinement on Unstructured Grids. In *AIAA 40th Aerospace Sciences Meeting & Exhibit*. Reno, NV, AIAA Paper 2002–0137.

Löhner, R., Yang, C. & Roger, R. 2002 Tracking Vortices over Large Distances Using Vorticity Confinement. In *24th Symposium on Naval Aerodynamics*. Fukuoka, Japan.

Mavriplis, D. J. 1999 Large-Scale Parallel Viscous Flow Computations Using an Unstructured Multigrid Algorithm. *Tech. Rep.* NASA Contractor Report 1999–209724. National Aeronautics and Space Administration, ICASE Report 99–44.

McMullen, M. S. 2003 The Application of Non-Linear Frequency Domain Methods to the Euler and Navier–Stokes Equations. PhD thesis, Stanford University.

McMullen, M. S., Jameson, A. & Alonso, J. J. 2001 Acceleration of Convergence to a Periodic Steady State in Turbomachinery Flows. In *AIAA 39th Aerospace Sciences Meeting & Exhibit*. Reno, NV, AIAA Paper 2001–0152.

McMullen, M. S., Jameson, A. & Alonso, J. J. 2002 Application of a Non-Linear Frequency Domain Solver to the Euler and Navier–Stokes Equations. In *AIAA 40th Aerospace Sciences Meeting & Exhibit*. Reno, NV, AIAA Paper 2002–0120.

McMullen, M. S., Jameson, A. & Alonso, J. J. 2006 Demonstration of Non-linear Frequency Domain Methods. *AIAA Journal* **44** (7).

Moin, P. 2001 *Fundamentals of Engineering Numerical Analysis*. Cambridge University Press.

Moin, P. 2003 *Supplementary Notes*. Stanford University, Stanford, CA, ME 408: Spectral Methods in Computational Physics.

Morvant, R., Badcock, K. J., Barakos, G. N. & Richards, B. E. 2005 Airfoil–Vortex Interaction Using the Compressible Vorticity Confinement Method. *AIAA Journal* **43** (1), 63–75.

Murayama, M., Nakahashi, K. & Obayashi, S. 2001 Numerical Simulation of Vortical Flows Using Vorticity Confinement Coupled with Unstructured Grid. In *AIAA 39th Aerospace Sciences Meeting & Exhibit*. Reno, NV, AIAA Paper 2001–0606.

Murman, E. M. & Cole, J. D. 1970 Calculation of Plane Steady Transonic Flows. In *AIAA 8th Aerospace Sciences Meeting*. New York, NY, AIAA Paper 1970–188.

Nicolaides, R. A. 1978 On the Observed Rate of Convergence of an iterative Method Applied to a Model Elliptic Difference Equation. *Mathematics of Computational* **32** (141), 127–133.

Owen, F. K. & Tauber, M. E. 1986 Measurement and Prediction of Model-Rotor Flowfields. *Journal of Aircraft* **23** (11), Presented as Paper 1985–1558 at the AIAA 18th Fluid Dynamics, Plasmadynamics and Lasers Conference, Cincinnati, OH, July 1985.

Pomin, H. & Wagner, S. 2001 Navier–Stokes Analysis of Helicopter Rotor Aerodynamics in Hover and Forward Flight. In *AIAA 39th Aerospace Sciences Meeting & Exhibit*. Reno, NV, AIAA Paper 2001–0998.

Pomin, H. & Wagner, S. 2002*a* Aeroelastic Analysis of Helicopter Rotor Blades on Deformable Chimera Grids. In *AIAA 40th Aerospace Sciences Meeting & Exhibit*. Reno, NV, AIAA Paper 2002–0951.

Pomin, H. & Wagner, S. 2002*b* Navier–Stokes Analysis of Helicopter Rotor Aerodynamics in Hover and Forward Flight. *Journal of Aircraft* **39** (5), 813–821, Presented as Paper 2001–0998 at the AIAA 39th Aerospace Sciences Meeting & Exhibit, Reno, NV, January 2001.

Pomin, H. & Wagner, S. 2004 Aeroelastic Analysis of Helicopter Rotor Blades on Deformable Chimera Grids. *Journal of Aircraft* **41** (3), 577–584.

Ramachandran, K., Owen, S. J., Caradonna, F. X. & Moffitt, R. C. 1994 Hover Performance Prediction Using CFD. In *The American Helicopter Society, 50th Annual Forum*, pp. 1259–1273.

Robinson, M. 2004 Application of Vorticity Confinement to Inviscid Missile Force and Moment Prediction. In *AIAA 42nd Aerospace Sciences Meeting & Exhibit*. Reno, NV, AIAA Paper 2004–0717.

Roe, P. L. 2001 Vorticity Capturing. In *AIAA 15th Computational Fluid Dynamics Conference*. Anaheim, CA, AIAA Paper 2001–2523.

Sheffer, S. G., Alonso, J. J., Martinelli, L. & Jameson, A. 1997 Time-Accurate Simulation of Helicopter Rotor Flows Including Aeroelastic Effects. In

AIAA 35th Aerospace Sciences Meeting & Exhibit. Reno, NV, AIAA Paper 1997–0399.

Srinivasan, G. R. & Baeder, J. D. 1992 TURNS: A Free-Wake Euler/Navier–Stokes Numerical Method for Helicopter Rotors. *AIAA Journal* **31** (5), 959–962, Technical Notes.

Srinivasan, G. R., Baeder, J. D., Obayashi, S. & McCroskey, W. J. 1990 Flowfield of a Lifting Rotor in Hover: A Navier–Stokes Simulation. *Tech. Rep.* NASA Technical Memorandum 102862. National Aeronautics and Space Administration.

Srinivasan, G. R. & McCroskey, W. J. 1993 Euler Calculations of Unsteady Interaction of Advancing Rotor with a Line Vortex. *AIAA Journal* **31** (9).

Srinivasan, G. R., Raghavan, V. & Duque, E. P. N. 1991 Flowfield Analysis of Modern Helicopter Rotors in Hover by Navier–Stokes Method. In *AHS and Royal Aeronautical Society, Technical Specialists' Meeting on Rotorcraft Acoustics/Fluid Dynamics Proceedings*. Philadelphia, PA.

Steijl, R., Barakos, G. N. & Badcock, K. J. 2005 A CFD Framework for Analysis of Helicopter Rotors. In *AIAA 17th Computational Fluid Dynamics Conference*. Toronto, Canada, AIAA Paper 2005–5124.

Steijl, R., Barakos, G. N. & Badcock, K. J. 2006 A Framework for CFD Analysis of Helicopter Rotors in Hover and Forward Flight. *International Journal for Numerical Methods in Fluids* **51** (8), 819–847.

Steinhoff, J. 1994 *Frontiers of Computational Fluid Dynamics*, chap. 14 Vorticity Confinement: A New Technique for Computing Vortex Dominated Flows, pp. 235–263. John Wiley & Sons, eds. Caughey, D. A. & Hafez, M. M.

Steinhoff, J. & Underhill, D. 1994 Modification of Euler Equations for "Vorticity Confinement" – Application to the Computation of Interacting Vortex Rings. *Physics of Fluids* **6** (8), 2738–2744.

Stepniewski, W. Z. & Keys, C. N. 1984 *Rotary-Wing Aerodynamics*, new edn. Dover Publications.

Strawn, R. & Ahmad, J. 2000 Computational Modeling of Hovering Rotors and Wakes. In *AIAA 38th Aerospace Sciences Meeting & Exhibit*. Reno, NV, AIAA Paper 2000–0110.

Vassberg, J., Gopinath, A. K. & Jameson, A. 2005 Revisiting the Vertical-Axis Wind-Turbine Design Using Advanced Computational Fluid Dynamics. In *AIAA 43th Aerospace Sciences Meeting & Exhibit*. Reno, NV, AIAA Paper 2005–0047.

van der Ven, H., Boelens, O. J. & Oskam, B. 2001 Multitime Multigrid Convergence Acceleration for Periodic Problems with Future Applications to Rotor Simulations. *Tech. Rep.* NLR–TP–2001–363. Nationaal Lucht- en Ruimtevaartlaboratorium.

Wang, C., J., Steinhoff & Wenren, Y. 1995 Numerical Vorticity Confinement for Vortex–Solid Body Interaction Problems. *AIAA Journal* **33** (8), 1447–1453.

Wenren, Y., Fan, M., Dietz, W., Hu, G., Braun, C., Steinhoff, J. & Grossman, B. 2001 Efficient Eulerian Computation of Realistic Rotorcraft Flows Using Vorticity Confinement. In *AIAA 39th Aerospace Sciences Meeting & Exhibit*. Reno, NV, AIAA Paper 2001–0996.

Wenren, Y., Walter, J., Fan, M. & Steinhoff, J. 2006 Vorticity Confinement and Advanced Rendering to Compute and Visualize Complex Flows. In *AIAA 44th Aerospace Sciences Meeting & Exhibit*. Reno, NV, AIAA Paper 2006–0945.

Xu, H., Zhang, S. & Khalid, M. 2005 Numerical Simulations of Unsteady Flows Past a Four-Bladed Rotor in Forward-Flight. In *AIAA 17th Computational Fluid Dynamics Conference*. Toronto, Canada, AIAA Paper 2005–5125.

Yang, Z., Sankar, L. N., Smith, M. & Bauchau, O. 2002 Recent Improvements to a Hybrid Method for Rotors in Forward Flight. *Journal of Aircraft* **39** (5), 804–812, Presented as Paper 2000–0260 at the AIAA 38th Aerospace Sciences Meeting & Exhibit, Reno, NV, January 2000.

Ying, S. X., Steger, J. L., Schiff, L. B. & Baganoff, D. 1986 Numerical Simulation of Unsteady, Viscous, High-Angle-of-Attack Flows Using a Partially Flux-Split Algorithm. In *Atmospheric Flight Mechanics Conference*. Williamsburg, VA, AIAA Paper 1986–2179.

Zhao, Q. J., Xu, G. H. & G., Zhao J. 2006 New Hybrid Method for Predicting the Flowfields of Helicopter Rotors. *Journal of Aircraft* **43** (2), 372–380.

Zierep, J. 1966 Theorie der Schallnahen und der Hyperschallströmungen. *Karlsruhe: G. Braun* .